ABSTRACT

Title of Thesis: ELECTROMAGNETIC CHARACTERIZATION OF MISALIGNED SERPENTINE WAVEGUIDE STRUCTURES IN TRAVELING-WAVE TUBES AT MICROWAVE FREQUENCIES

Kyle Francis Kuhn
Master of Science, 2022

Thesis Directed by: Professor Thomas M. Antonsen, Jr.
Institute for Research in Electronics and Applied Physics
Department of Electrical and Computer Engineering

Modern-day millimeter and microwave source technology has advanced considerably over the past century, but to meet the defense industry's demand for high power and large bandwidth, vacuum electronic devices (VEDs) are still the ideal candidate to fulfill such requirements as opposed to their solid-state semiconductor counterparts. Of the numerous VEDs available, the traveling-wave tube (TWT) amplifier provides novel solutions in areas where size, weight, and power (SWaP), and bandwidth are of great importance such as on satellites and in electronic warfare applications.

The advancement in computer-aided design (CAD) and simulation has allowed for increasingly complicated device configurations to be designed with ease. Instead, challenges arise in fabrication as extremely tight manufacturing tolerances on the order of micron to sub-micron levels are necessary due to the very short wavelengths in the mm-wave and sub-mm-wave

regimes. Without this level of manufacturing precision, VEDs will not operate at optimal levels in power, bandwidth, and efficiency.

We present a serpentine waveguide (SWG) design to be used as the slow-wave structure (SWS) in a TWT amplifier. Manufacturing techniques for the design are discussed, and a detailed study into how one-dimensional and two-dimensional misalignments in the circuit's half-plane affect the radio frequency (RF) signal that propagates through the device. Figures of merit include the device's reflected power, or S_{11}, the transmitted power through the SWG, or S_{21}, the device's cutoff frequency, and the SWG's dispersion curves.

Computer simulations using Ansys's High Frequency Structure Simulator, or HFSS, and cold test laboratory measurements for aligned and misaligned Ka-band (26.5 GHz – 40 GHz) SWG circuits are presented. Upon completing a thorough RF characterization of the Ka-band device, efforts will shift focus to designing a SWG circuit for a W-band (75 GHz – 110 GHz) TWT amplifier prototype.

Electromagnetic Characterization of Misaligned Serpentine Waveguide Structures in Traveling-Wave Tubes at Microwave Frequencies

by

Kyle Francis Kuhn

Thesis submitted to the Faculty of the Graduate School of the
University of Maryland, College Park in partial fulfillment
of the requirements for the degree of
Master of Science
2022

Advisory Committee:
Professor Thomas M. Antonsen, Jr., Chair
Professor Brian L. Beaudoin, Co-Chair
Professor Yanne K. Chembo
Professor Patrick G. O'Shea
Dr. Zachary Drikas, U.S. Navy
Dr. Bisrat Addissie, U.S. Navy

Preface

The United States Navy (USN) and the United States (U.S.) Department of Defense (DoD) often seek external assistance in developing technology directly related to their core mission objectives. There are many methods by which this goal can be accomplished. The more conventional and well-known manner includes the United States Government contracting large, private companies such as Lockheed Martin, Norhrop Grumman, Raytheon, Leidos, etc., to complete more demanding tasks such as building the next-generation fighter jet. Another lesser-known method, born out of the Small Business Innovation Development Act of 1982 and the Small Business Technology Transfer Act of 1992, both passed by Congress, stimulates technological innovation to meet the government's needs while promoting small business growth by contracting domestically-based, for-profit companies with no more than 500 employees and affiliates [1].

The work described herein is directly supported by the Small Business Innovation Research (SBIR) and Small Business Technology Transfer (STTR) programs, the latter of which partners a small business meeting the aforementioned requirements with a university, a federally funded research and development center, or a qualified non-profit research institution [2].

Dedication

To my incredible family and friends. Your unconditional love and support gave me strength throughout this difficult journey. This would not have been possible without you.

Acknowledgments

I owe my most sincere gratitude to the many people who made my graduate education in electrical engineering achievable.

First and foremost I would like to thank my advisor, Professor Thomas Antonsen, Jr., for allowing me to study under his direction. His world-leading knowledge of vacuum electronics, plasma physics, and many other disciplines within electrical engineering truly cultivated a learning environment second to none. He also provided me with the opportunity to travel to two international conferences allowing me to gain incredible insights into these fields as well as being able to network with other field-leading engineers and physicists. Professor Antonsen always made himself available, regardless of the current circumstances, and never relinquished his patience for my seemingly endless questions. I further thank him for understanding the incredibly tight timeline under which I was restricted to complete my Master's Degree and for his support throughout this process. I consider myself extremely lucky to be one of his students.

I would also like to thank my co-advisor, Professor Brian Beaudoin, for his additional support. He was generous enough to grant me space in his laboratory to carry out measurements as well as providing me with personal equipment to facilitate measurements and simulations.

It is also imperative to recognize NAVSEA and the Navy for funding the research described in this thesis through the contract N68335-20-C0815 and the amazing research group with whom I was so fortunate to work. Professor Antonsen, Professor Beaudoin, Dr. John Petillo, Philipp

Borchard, Aaron Jensen, and Heather Shannon were all invaluable in supporting this research. Not only are they all especially knowledgeable and talented, it was truly a joy working with them. I am hopeful additional opportunities for collaboration will arise in the future.

The members serving on my defense committee are owed my gratitude, as well. Professor Yanne Chembo has been instrumental in my collegiate education ever since I took his introduction to static electromagnetics course for undergraduates at the University of Maryland, which was the first class he taught upon arriving at the institution as an Associate Professor in 2019. I have since taken many more courses within the electrophysics discipline taught by him, but it is he who pushed me to pursue a graduate education and has unconditionally supported me throughout my journey. It is with great pleasure I have witnessed him rise through the ranks within the ECE Department and IREAP as it is so well-deserved. Additionally serving on the committee is Professor Patrick O'Shea whose graduate charged particle beam course solidified my understanding of the work presented in this thesis. Professor O'Shea teaches with great passion and the material he covered served as the final puzzle piece to this work.

Last, but certainly not least, Dr. Zachary Drikas and Dr. Bisrat Addissie have agreed to serve as special committee members. Dr. Drikas and Dr. Addissie were kind enough to grant me an interview for a summer internship at the Naval Research Laboratory in Washington, D.C. before I even finished my first semester as an undergraduate electrical engineering student. Not only did they make the time to consider an interview, they saw potential in me and awarded me the position. I am eternally grateful for their consideration because not only was my first "real" job a dream position at a DoD laboratory working on electronic warfare systems, but it is where I was first exposed to RF engineering. Let's just say I was sold on specializing in electrophysics from the moment I came into work on my very first day and never looked back...

Additional thanks go out to Dr. Valery Dolgashev of the SLAC National Laboratory for his availability and willingness to help me with the incredibly complex software, HFSS; Emily Irwin of the Electrical and Computer Engineering Department at the University of Maryland for always being patient with me, my never-ending questions, and my tight degree timeline; the Science, Mathematics, and Research for Transformation (or "SMART") Program for funding my education; John Soos and Gina Guiducci of C5ISR at Aberdeen Proving Ground, Maryland, for sponsoring me through the SMART Program and providing me with a full-time position post-graduation; all my former colleagues in NRL Code 5745 including Daniel Webb, Victor Mendez, and others; Dr. Nathaniel Ferlic, a recently graduated Ph. D. student from the UMD ECE program, who provided me with invaluable guidance from a former student's perspective; Dr. Alan Cook, Dr. Igor Chernyavskiy, Dr. Simon Cooke, Dr. Colin Joye, Dr. Khanh Nguyen, and many others who laid the groundwork for much of the folded/serpentine waveguide research discussed in this thesis; and Dottie Brosius of IREAP for creating the unbelievable LaTeX template used to compose this thesis and for her help with my many elusive LaTeX troubles.

Finally, I would be remiss without expressing my eternal gratitude for the unwavering love and support of my parents, Chris and Sharon, my sister, Julia (and of course, our spoiled German Shepard, Rhody), as well as my entire extended family and friends including A. Alem, R.J. Banks, P.J. Eichensehr, M.A. Eisenberg, N.L. Griisser, K.R. Harry, L.C. Joseph, Z.T. Kessler, B.H. Knorr, V. Lehmann, C.M. Morgan, A.M. Piepol, K.A. Smith, J. Tano, L.G. Tondin, and many others whose names I cannot include here as the list would be too long. I am forever indebted to you all for your love. Thank you from the bottom of my heart.

— K.F. Kuhn

Table of Contents

List of Tables

List of Figures

List of Publications

1. **K.F. Kuhn**, T.M. Antonsen, Jr., B. Beaudoin, P. Borchard, J. Hoh, J. Petillo, and A. Jensen, "Characterization of the effects of misalignments in a Ka-band serpentine waveguide structure," in *International Conference on Plasma Sciences (ICOPS), Seattle, WA, USA, May 22–26, 2022*.

2. J. Petillo, S. Ovtchinnikov, A. Jensen, P. Borchard, **K. Kuhn**, B. Beaudoin, and T.M. Antonsen, Jr., "The determination of beam transport manufacturing parameter sensitivities using adjoint methods in the presence of static fields with MICHELLE," in *International Conference on Plasma Sciences (ICOPS), Seattle, WA, USA, May 22–26, 2022*.

3. **K.F. Kuhn**, T.M. Antonsen, Jr., B. Beaudoin, P. Borchard, J. Hoh, J. Petillo, and A. Jensen, "Characterization of refelected RF power in a misaligned Ka-band serpentine waveguide TWT," in *International Vacuum Electronics Conference (IVEC), Monterey, CA, USA, April 25–28, 2022*, pp. 71–72.

4. P. Borchard, J. Hoh, **K. Kuhn**, B. Beaudoin, T.M. Antonsen, Jr., J. Petillo, and A. Jensen, "Fabrication of traveling wave tube amplifier circuit using elastic averaging precision alignment technique," in *International Vacuum Electronics Conference (IVEC), Monetery, CA, USA, April 25–28, 2022*, pp. 166–167.

5. J. Petillo, S. Ovtchinnikov, A. Jensen, P. Borchard, **K. Kuhn**, B. Beaudoin, and T.M. Antonsen, Jr., "Development and application of adjoint methods in the presence of static electric and magnetic fields in the MICHELLE beam optics code," in *International Vacuum Electronics Conference (IVEC), Monetery, CA, USA, April 25–28, 2022*.

List of Abbreviations

1D	One-Dimensional
2D	Two-Dimensional
BWO	Backward-Wave Oscillator
CAD	Computer-Aided Design
CC	Coupled-Cavity
CEM	Computational Electromagnetic
CNC	Computer Numerical Control
CST	Computer Simulation Technology
dB	Decibels
DoD	Department of Defense
EA	Elastic Averaging
ECE	Electrical and Computer Engineering
EM	Electromagnetic
EW	Electronic Warfare
FEM	Finite-Element Method
FoM	Figure of Merit
FW	Folded Waveguide
FWHM	Full-Width Half Maximum
HFSS	High-Frequency Structure Simulator
HPM	High-Power Microwave
HV	High Voltage
IOSTT	Input/Output Step-Out to Taper
IOTL	Input/Output Taper Length
IREAP	Institute for Research in Electronics and Applied Physics
ISW	Input Step Width

KC	Kinematic Coupling
KCL	Kirchhoff's Current Law
mm-Wave	Millimeter-Wave
NAVSEA	Naval Sea Systems Command
NRL	Naval Research Laboratory
PiC	Particle-in-Cell
PNA	Performance Network Analyzer
QKC	Quasi-Kinematic Coupling
RADAR	Radio Detection and Ranging
RF	Radio Frequency
RMS	Root-Mean-Square
SBIR	Small Business Innovation Research
SLAC	Stanford Linear Accelerator Center
SOLT	Short, Open, Load, and Thru
STTR	Small Business Technology Transfer
SWaP	Size, Weight, and Power
SWG	Serpentine Waveguide
SWS	Slow-Wave Structure
TRL	Thru, Reflect, and Line
TWT	Traveling-Wave Tube
UMD	University of Maryland
U.S.	United States
USN	United States Navy
VED	Vacuum Electronic Device
VNA	Vector Network Analyzer
WR	Rectangular Waveguide

Chapter 1: Introduction

1.1 Motivation

The continuously-evolving societal dependence on wireless electronic devices has caused such devices to permeate almost every facet of day-to-day life. The defense industry is also not immune to the increased reliance on this equipment; in fact, it is often at the forefront of groundbreaking developments in such electronics. For this reason, wireless electronic device development, maintenance, and security have become de facto core values for the United States Department of Defense (DoD).

Inherent in these core values lie the importance of advancing and maintaining reliable communications and society-advancing research, both of which demand increasingly high powers and large bandwidths. Also demanding the same requirements are electronic warfare (EW) systems for use in defending the United States' and its allies' ability to successfully operate secure communications systems and continue to carry out essential defense capabilities in the event of an adversarial attack. As bandwidth requirements continue to increase, higher frequencies in the millimeter-wave (mm-wave) regime (30 GHz – 300 GHz) and the sub-mm-wave regime (300 GHz – $\approx$3 THz) are needed. The increase in power in conjunction with higher frequencies gives rise to significant challenges for devices to meet these standards.

Modern-day technology has advanced considerably over the past century, but to meet the needs for high power and large bandwidth, vacuum electronic devices (VEDs) are still the ideal candidate to fulfill said requirements (solid-state semiconductor devices are not yet capable of achieving these capabilities). They also provide novel solutions in areas where size, weight, and power (SWaP) are of equal importance (such as on satellites) [3].

The advancement in computer-aided design (CAD) and simulation has allowed for increasingly complicated device configurations to be designed with ease. Instead, challenges arise in fabrication because extremely tight manufacturing tolerances on the order of micron (μm) to sub-micron (sub-μm) levels are necessary due to the very short wavelengths in the mm-wave and sub-mm-wave regimes. Without this level of manufacturing precision, VEDs will not operate at optimal levels in power, bandwidth, and efficiency.[1]

Difficulties in producing high-frequency, high-power, and large bandwidth VEDs does not end with tight manufacturing specifications. Tolerances on the order of a few microns to sub-micron levels are additionally very expensive. This is due to many factors, but there are two that are most restrictive. The first issue is there are few machines capable of achieving such levels of accuracy [3]. Secondly, VEDs are typically composed of many smaller components, each of which must also be fabricated precisely. When these smaller components are assembled to compose the final device, each component's error will negatively contribute to the full assembly's performance quality. For this reason, tight tolerance devices generally have a low yield thereby making them significantly more expensive. Low yields manifest on the consumer side (in this

[1] "Optimal levels" in the EW context also constitute unparalleled device operation (and little to no degradation in performance) even in the most harsh electronic and environmental conditions.

context, the U.S. Navy) as higher costs for the product or conceding to using a device with sub-par performance in one or more of its design facets, which is not optimal [3].

The STTR supporting the work described herein states that our group must develop technologies capable of "...high precision assembly of the extremely high tolerance, large aspect ratio components required by modern mm-wave vacuum electronics ..." [3, 4]. In other words, we must develop solutions to the problems discussed in the introductory paragraphs.

The precision alignment of the device's components is essential to accomplish this program's goals. For this reason, additional program requirements articulate our solution must also make use of at least one of the of following methods (but are not limited to those stated) to fasten assembly pieces together:

- **Elastic Averaging (EA):** Mitigates structural misalignments by averaging out errors through "controlled compliance between precision surfaces" (see Figs. 1.1 and 1.2b). EA has a precision accurate to 1 μm (for more details on the elastic averaging technique, see [5]) [4, 6].

- **Kinematic Coupling (KC):** A type of deterministic coupling (i.e., the same initial conditions will always result in the same final system state) where the number of constraining or contact points on the fastener equals the degrees of freedom to be constrained (see Fig. 1.1 and 1.2c). KC has a precision that can be accurate to less than 0.1 μm [4, 6].

- **Quasi-Kinematic Coupling (QKC):** A variation of KC, QKC relies on an arc-shaped contact (as opposed to point contacts in KC) that allows for lower contact stresses due to the larger contact area. QKC has a precision accurate to sub-μm levels (< 0.1 μm) (see Fig. 1.1 and 1.2d) [4, 6].

It is important to take into account when designing VEDs that KC does not have the ability to maintain a vacuum seal whereas EA and QKC do have this capability.

Though the main goal of this STTR is focused on mechanical precision alignment techniques, because these techniques are being employed in VEDs, there are consequences on the radio frequency (RF) and electron gun components that need to be studied. This thesis will focus mainly on the research into characterizing the effects misalignments have on the RF components of the VED. This and other research contributions will be briefly outlined in Sec. 1.2.

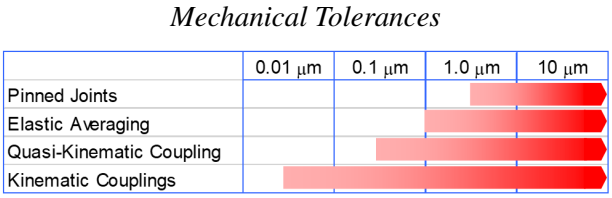

Figure 1.1: Mechanical tolerances for various coupling techniques. Adapted from [7].

1.2 Research Contributions

The awarded STTR is a three-year contract under which Dymenso, LLC; the University of Maryland (UMD), College Park; and Leidos, Inc. are partnered to deliver a functional W-band (75 GHz – 110 GHz) traveling-wave tube (TWT) amplifier prototype using a serpentine waveguide (SWG) as its slow-wave structure (SWS) to the United States Naval Research Laboratory (NRL) (see Ch. 2 for more details on traveling-wave tubes, serpentine waveguides,

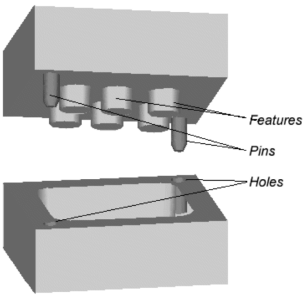

(a) Conventional pinned joint alignment method.

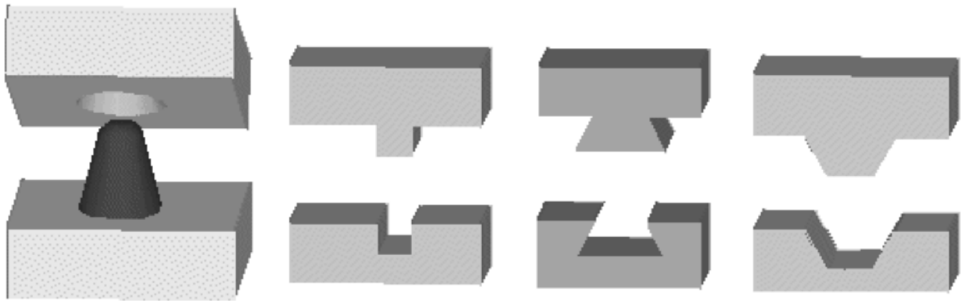

(b) Examples of the elastic averaging method. From left to right: collet, rail/slot, dovetail, and V/groove.

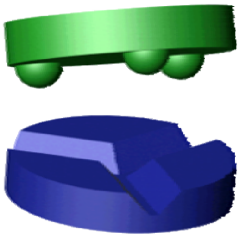

(c) Kinematic coupling method.

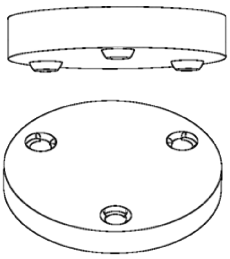

(d) Quasi-kinematic coupling method.

Figure 1.2: Various mechanical alignment and coupling methods. Methods (b), (c), and (d) are often used for precision alignment techniques. Adapted from [6, 7].

and slow-wave structures). This thesis comes at the end of the contract's first year and each group's responsibilities to this point are described below.

Dymenso will create the Ka-band circuit's mechanical design by optimizing the EA alignment technique and simulating the device at high temperatures (up to 1000°C) to ensure mechanical robustness and repeatability in bakeout and operational environments; fabricate the Ka-band design; perform quality control measurements on the fabricated Ka-band circuit; and begin to create the W-band circuit's mechanical design [4].

UMD will provide the electrical design for the Ka-band SWG circuit, cold test the circuit in the laboratory once fabricated by Dymenso, design the W-band circuit for the TWT prototype, perform any laboratory tests for the W-band TWT, and conduct analytical research in developing and applying the adjoint method to beam optics sensitivities [4].

Leidos will assist UMD in realization of the adjoint method by implementing it in the beam optics and collector design particle-in-cell (PiC) code, MICHELLE, managed by NRL and Leidos [4].

1.3 Thesis Outline

This thesis is organized in the following manner: Ch. 2 provides a comprehensive background of TWTs, coupled-cavities (CCs), folded waveguides (FWs), serpentine waveguides, and the chosen fabrication method for the SWG in this study. In Ch. 3, a review of SWG circuit theory is presented. Following the theory, a Ka-band SWG circuit design is discussed. Ch. 4 describes the methods used to improve matching between the SWG and the tapers to

a standard waveguide size, Ch. 5 presents detailed simulations of how one-dimensional and two-dimensional misalignments in the device affect the microwave signal, and Ch. 6 includes laboratory cold test measurements for fabricated Ka-band circuits. Finally, an analytical optimization model is presented in Ch. 7 to avoid exciting backward waves in a SWG circuit that will be used in the W-band SWG TWT prototype to be delivered to the Navy. Conclusions are made in Ch. 8 where future work is also stated.

Chapter 2: Background

2.1 Overview

It is crucial to first understand at a high level the application of the SWG before it is presented in detail. Though the SWG is widely studied by academia and in vacuum electronics research, its primary application is to serve as a slow-wave structure in TWT amplifiers. A brief discussion of TWT amplifiers' principle operation is presented in this chapter as well as the reasons for which the SWG is beneficial for its design in certain applications.

2.2 Traveling-Wave Tubes

2.2.1 Introduction

The traveling-wave tube has been the design of choice for microwave frequency signal amplification for over 50 years. They can be seen in a wide variety of applications ranging from radio detection and ranging (RADAR) to electronic warfare (EW), from satellites to other communications methods, and even in research. Their widespread use results in their domination of the microwave vacuum tube market by accounting for over 50% of all sales [8].

In this section, a brief history of the traveling-wave tube will be discussed followed by an analysis of helix TWTs (the first TWT to be developed). Once the fundamental groundwork has

been laid, a discussion on other cavities and slow-wave structures will be presented, followed by the motivation for selecting the SWG as the circuit to be studied. The adjoint method, which is a mathematical method recently applied to TWTs to optimize various performance characteristics such as electron gun design and circuit alignment, is presented in Appendix A.

2.2.2 A Brief History of the Traveling-Wave Tube

The first notion of controlling an electron beam using high frequency electromagnetic (EM) waves was introduced in a patent by the Russian electrical engineer Andrew V. Haeff in 1936 [8]. Haeff was working on an oscillograph, or an early version of the oscilloscope, at the California Institute of Technology when he was successfully able deflect a hollow electron beam using a radio frequency signal running through a helix. During his research, he also observed amplification in the RF signal; however, he did not describe the reason for this phenomenon [8, 9, 10].

Shortly before Haeff's patent was submitted, Dutch engineer Klaas Posthumus, working at the Philips National Laboratory in Eindhoven, Netherlands, described the interaction between an EM wave and an electron in 1935 [8, 11]. His analysis stated that when the tangential component of velocity of an RF signal propagating through a helix is the same (or very close to) the average velocity of an electron traveling in the direction of the helix's axis, the EM wave and the electron will have a strong interaction causing the electron to transfer energy to the RF signal [8]. Such a development laid the foundation for more rigorous research into traveling-wave tube technology. It wasn't until June 1946, however, that TWTs were first announced to the public at the Fourth

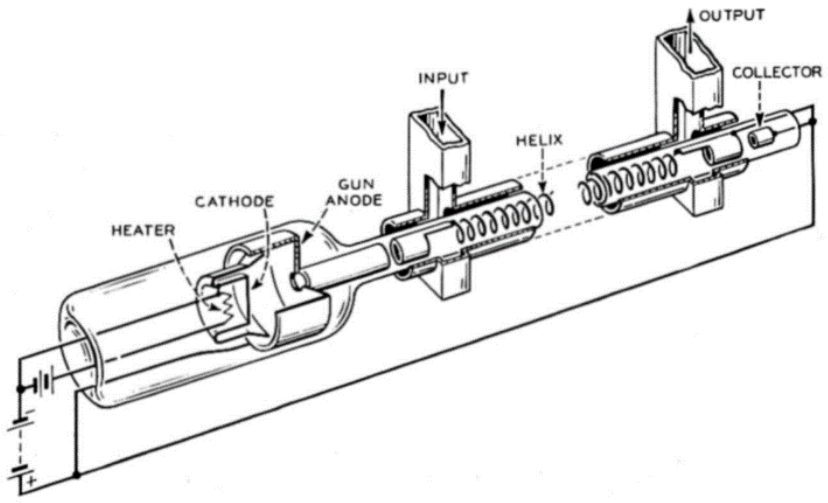

Figure 2.1: J.R. Pierce's traveling-wave tube design. Adapted from [12].

Institute of Radio Engineer's Electron Tube Conference at Yale University [8]. In the same year, Andre Blanc-Pierre and Pierre Lapostolle described the first elementary coupled-cavity TWT [8].

Though the technology and some basic theory for traveling-wave tubes had been around for approximately 10 years at the point of the Radio Engineer's Electron Tube Conference in 1946, the most rigorous and fundamental theory for the devices was not introduced until January 1950, when American engineer John R. Pierce published his paper, "Traveling-Wave Tubes," in the Bell System Technical Journal [12]. Fig. 2.1 depicts his design of the traveling-wave tube. It was from this paper that TWT technology expanded rapidly and began to permeate into several applications, some of which were described in the introduction to this paper, in which they still exist in modern technology. Even today, Pierce's paper is widely considered the foundational theory behind TWTs.

2.2.3 TWTs – A Common Choice

A logical and very important question arises at this point: why are traveling-wave tubes so widely used as microwave amplifiers as opposed to other devices? The answer to this question is discussed in more detail below, but the explanation largely lies in the TWT's large bandwidth and high gain.

In order to further motivate the benefits of TWTs, introducing the klystron is necessary. A klystron is another type of microwave tube that was developed largely in parallel to TWTs. Detailed analysis of the klystron's principle operation is beyond the scope of this text, but to briefly summarize the device, it is similar to the TWT in the sense that an electron beam propagates through a vacuum tube that is connected to (generally) two cavities. One cavity has RF injected into it (by means of coupling, which is usually inductive) from an external source and a the second cavity is where the amplified RF signal is extracted (also by inductive or capacitive coupling). Like the TWT helix, the cavities in a klystron serve as areas where beam-wave interaction occurs.

In any respect, helix TWTs have a much larger bandwidth than klystrons [13]. In fact, the bandwidth of a helix TWT can exceed two octaves whereas klystrons can only operate within about 10% – 15% of its cavity's resonant frequency [8]. The fact that klystrons are limited to their cavity's resonant frequency also brings to light the problem of operating frequencies and size. To design a resonant cavity for less than 1 GHz, its size would be quite large (due to the fact cavity size is inversely proportional frequency) and in many cases, impractical. In helix TWTs, however, there are no such size restrictions because the RF signal propagates on a conducting

helix rather than resonating in a cavity; for this reason, TWTs have been designed to operate at frequencies ranging from hundreds megahertz to over 300 GHz (in coupled-cavity TWTs) [8].

The amplifier's gain is also an important figure of merit in their design. Two-cavity klystrons typically have a maximum gain of about 20 dB and can operate with peak powers on the order of megawatts. Klystron gain can be increased to ≈80 dB with the addition of two cavities (for a device with four cavities in total), but due to the increase in size with additional cavities, klystrons typically do not incorporate more than four cavities [14]. TWTs, on the other hand, can reach a small signal gain of about 20 dB – 50 dB and can operate with an average power on the order of kilowatts [14]. Though the maximum gain is usually less than a four-cavity klystron, the size of the TWT with 50 dB gain is much smaller than that of a klystron with the same gain.

The one area where a klystron outperforms a TWT is in efficiency. TWTs have efficiencies that typically range from 10% to 40%, however, older TWTs operate with 10% – 20% efficiency [14]. TWT efficiency can be increased by introducing a variable pitched helix as described in [15] or by the addition of a depressed collector located at the end of the device. The collector recovers some of the beam's electrons and recycles them within the circuit. Klystrons, on the other hand, routinely operate with efficiencies greater than 40% and have a maximum theoretical efficiency of 58%.

A very practical example of a case in which a TWT would be highly advantageous to choose over klystron (or any other vacuum tube amplifier, for that matter) is in an electronic warfare application. EW systems typically strive for very high gain over very large bandwidths to cause interference and disrupt communications. This must usually be done in a reasonably sized package, as well, further solidifying the choice of a TWT amplifier. Their compact design

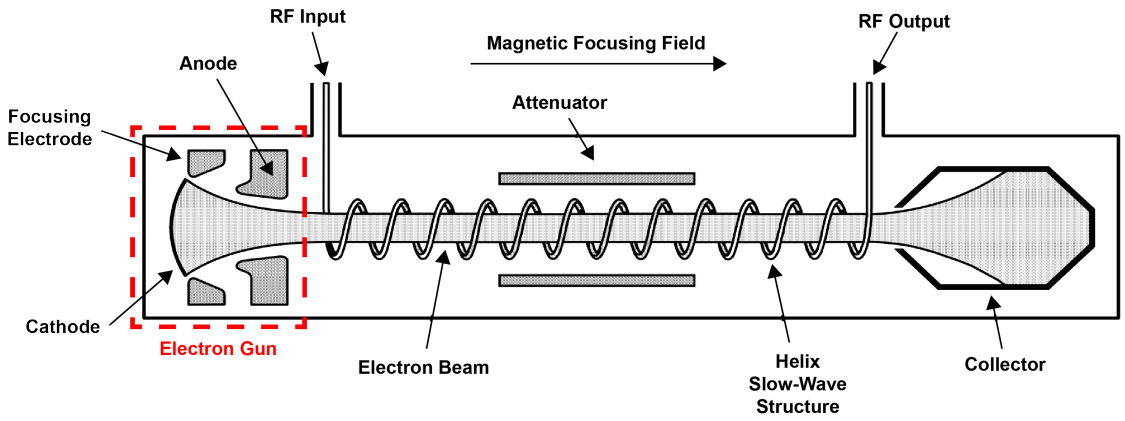

Figure 2.2: Basic schematic depiction of a helix TWT amplifier. Adapted from [8].

also makes them ideal for deployment on satellites where device footprint size and weight are of the utmost importance.

2.2.4 Helix TWTs

Carrying out the analysis of traveling-wave tubes to understand their principle operation is most logically done by separating its components into two parts: the RF circuit and the beam. Before it is possible to delve into the analysis of the SWG TWT, which is the focus of this thesis, it is essential to understand the most fundamental TWT, or the helix TWT. To do this, first consider the basic schematic representation of a TWT illustrated in Fig. 2.2.

The small signal analysis of the TWT in Fig. 2.2 begins by applying Posthumus' and Pierce's observations of beam-wave interactions. They concluded that for RF signal amplification to occur, the $\hat{z}$-component (or axial component) of the velocity of the RF wave in the helix must be equal, or very close, to the average velocity of the electrons in the beam propagating along the helix's axis (the reader will have to take this fact on merit in order to further develop the theory behind the beam-wave interactions; the explanation of these findings will arise naturally as the

subsequent analysis continues) [8, 12]. There is a glaring issue with this observation, however. The RF signal propagates through the helix at the speed of light and the electrons in the beam cannot travel at such a speed. Thus, a method to slow the RF propagation must be conceived.

To slow the EM wave's propagation velocity in the helix, consider the RF signal propagating along the conducting helix from left to right in Fig. 2.2. The axial component of the wave's velocity along the helix is given by

$$v_{ph} = c \sin \psi = \frac{cp}{\sqrt{p^2 + (2\pi a)^2}} < c \tag{2.1}$$

where c is the speed of light, ψ is the helix's pitch angle with respect to the vertical axis, a is the helix radius, and p is the length of a single helix period along $\hat{z}$ (see Fig. 2.3). This axial component of velocity will be defined as the phase velocity, v_{ph}, herein. Note that v_{ph} is the RF wave's velocity along the helix's path reduced by the helix's pitch. Thus, v_{ph} is less than the speed of light. For this reason, the helix is referred to as a "slow-wave structure" (or SWS). In order to match the RF phase velocity to the average speed of the electrons in the beam, the helix's pitch, ψ, must be designed such that $v_{ph} = csin\,(\psi) = \langle v_e \rangle$ where the angle brackets denote the average of the argument and v_e is the electron's velocity in the beam in the $+\hat{z}$-direction.

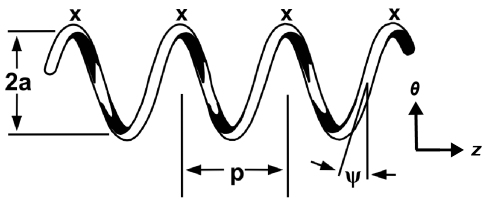

(a) 3D helix geometry.

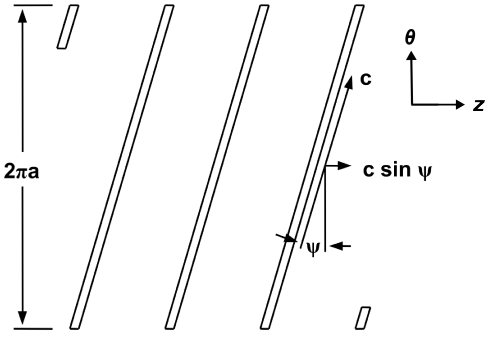

(b) 2D projection of 3D helix geometry.

Figure 2.3: Helix geometries. Adapted from [8].

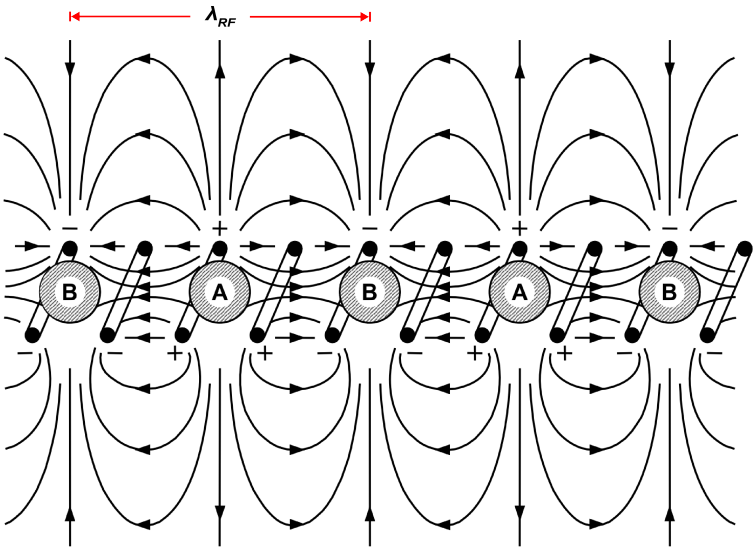

Figure 2.4: Electric field in a conducting helix where one half-wavelength of the RF signal spans two full helix turns. Adapted from [8].

Now that $v_{ph} = \langle v_e \rangle$, the physics behind the beam-wave interaction can be discussed. In Fig. 2.4, the electric field lines are drawn for a helix in which a half-wavelength of the RF field spans two complete helix turns. In other words, a single period of the RF signal spans four helix turns. The reasons behind choosing four helix turns per RF period are discussed in more detail in [12]. It is these fields that are the mechanism carrying out the beam-wave interaction. When actually designing a TWT, the helix pitch, the number of turns, and its length must be carefully chosen based on the TWT's desired bandwidth and the beam energy. For the preliminary analysis of the beam-wave interactions, it is assumed the helix is in a magnetic field-free region, i.e., $\boldsymbol{B} = 0$ everywhere.

From Fig. 2.4, it is clear electrons in the beam entering the helix are located in Region B where they experience an axial force in the $+\hat{z}$-direction due to the EM fields (this force is more commonly known as the Lorentz force). The Lorentz force is given by $\boldsymbol{F} = q\left(\boldsymbol{E} + \boldsymbol{v} \times \boldsymbol{B}\right)$ where $\boldsymbol{F}$ is the force vector, $q = -e$ is the charge, e is the fundamental charge, $\boldsymbol{E}$ is the electric

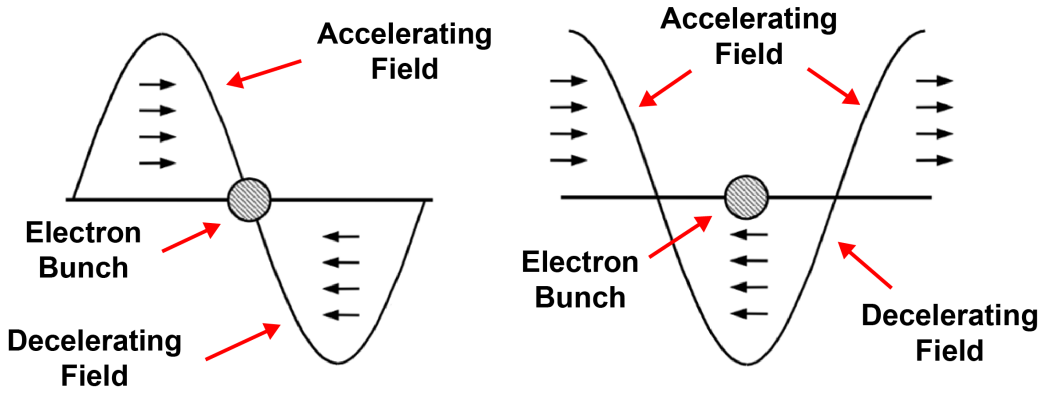

(a) Beam entering helix.

(b) Electron bunch in the field from (a) after experiencing a $-\pi/2$ phase shift.

Figure 2.5: Illustration of the interaction between the helix's electric field and the electron beam (a) when the beam first enters the helix and (b) when the electron bunch in the beam falls into decelerating field after the electric field undergoes a $-\pi/2$ phase shift. The sinusoidal traces depict the force $F = qE = -eE$. Adapted from [8].

field vector, and $\boldsymbol{B}$ is the magnetic flux field vector. The charge will be accelerated in the $+\hat{z}$-direction upon seeing this force in Region B.

The accelerated charges moving in the $+\hat{z}$-direction will then enter Region A where the electric field's direction reverses from pointing in the $-\hat{z}$-direction to pointing in the $+\hat{z}$-direction. The change in the electric field's sign is due to the helix's changing polarity corresponding to a half-wavelength of the RF signal per two complete helix turns. The electrons in Region A will thus experience a force in the $-\hat{z}$-direction and will be decelerated. Electrons are still being accelerated in Region B, however, so they will begin to catch up to those being decelerated in Region A. This causes electron "bunches" to begin to form. The bunches in the early stages of the helix are far from discrete; in other words, the bunch edges are not yet well-defined.

The space charge forces begin to increase in the volume the bunches occupy and said forces start to have an effect on the EM wave traveling through the helix. Electrons on the helix located

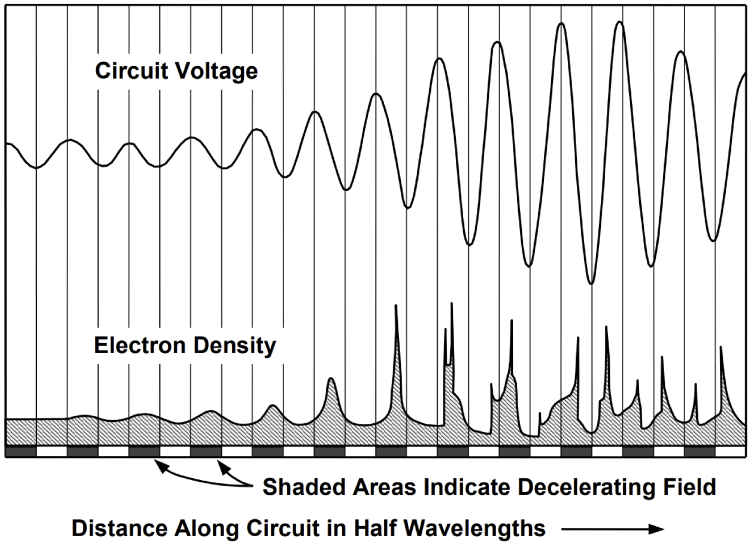

Figure 2.6: Correlation between the amplified RF signal and the accumulation of electron density in the bunches in a TWT amplifier. Adapted from [8].

behind the forming bunches travel with $v'_{ph} = -2v_{ph}$ relative to the beam and the electrons on the helix in front of the bunch travel at $v'_{ph} = v_{ph}$ relative to the beam (i.e., they appear stationary with respect to the beam) [8]. Thus, the charge density behind the bunch decreases (decreasing the space charge force behind the bunch) and the charge density in front of the beam increases (increasing the space charge force in front of the beam). The electron's change in phase velocity on the helix also causes the RF signal to undergo a $-\pi/2$ ($-90°$) phase shift, thereby shifting the electric field by $-\pi/2$ as well (shown in the transition from Fig. 2.5a to Fig. 2.5b). Now that the beam is out of phase with the electric field, the electron bunches shift into a region where $\boldsymbol{E}$ points in the $+\hat{z}$-direction, which is a decelerating field as depicted in Fig. 2.5b. The energy the electrons lose from being decelerated by this electric field is transferred to the wave in the helix resulting in the desired amplification of the RF signal [8].

Like any real system, the RF amplification is not infinite. As the bunches continue to decelerate, they become more discrete and more charge accumulates in them resulting in a large

increase of space charge forces within the bunches. Increasing space charge forces cause a phase lag in the RF signal and its phase shifts by an additional $-\pi/2$ [8]. The electron bunches are now in phase with an accelerating electric field and they extract energy from the RF signal on the helix thereby reducing the amplification. The point at which this occurs is called the TWT saturation point, i.e., when the RF signal's energy is equal to the beam's energy and the maximum amplification has been achieved [8]. This phenomenon is depicted in Fig. 2.6.

The helix's wire size also contributes to the beam-wave interaction that amplifies the RF signal. For this reason, the wire's geometry must be carefully selected. If the wire's cross-section is very small, the EM fields will not radiate very far from the wire's edge and there will be little beam-wave interaction. If the wire's cross-section is too large (i.e., if the mean helix radius is less than the wire's internal diameter), however, there will be little space for the electron beam to propagate along the helix's axis. This would result in excess collisions between the beam and the wire likely damaging the helix and degrading TWT performance [12]. The solution to this is to create a helix constructed from a conducting metal sheet (also called a "tape helix") that can be located close to the beam so as to increase the beam-wave interaction and also allow the beam to propagate through the device with few collisions [12].

The preceding, mostly qualitative, analysis has described the basic functionality of a helix traveling-wave tube and illustrated the phase velocity of the EM wave on the helix must match the average velocity of the electrons in the beam in order to facilitate interaction between the electrons present in the beam and the microwave signal.

2.3 Coupled-Cavities, Folded Waveguides, and Serpentine Waveguides

2.3.1 An Alternative to the Helix

A conducting tape helix is not the only method to implement a SWS in a TWT. Other common slow-wave structures used in TWTs, particularly at frequencies at and above Ka-band (26.5 GHz – 40 GHz), are the folded waveguide (FW) depicted in the Fig. 2.7a and the serpentine waveguide depicted in Fig. 2.7b.

In the FW/SWG SWS, the RF signal propagates through the meandering waveguide and the electron beam passes through the beam tunnel that bisects the waveguide. There is a gap in the region where the beam tunnel intersects the waveguide so that the EM wave can interact with the beam. This region is referred to as the "gap" and there are two gaps in a single period of the FW/SWG. For this reason, the FW/SWG structure is actually a special case of a coupled-cavity circuit; each portion of the meandering waveguide separated by the beam tunnel is its own cavity capacitively coupled to the next section. The meandering waveguide's principle is identical to that of the helix: to slow the RF's (axial) phase velocity such that it is approximately equal to the electron's velocity in the beam.

Folded waveguides and serpentine waveguides are usually the choice design when working with mm-wave frequencies and above. This is mainly due to fabrication processes and power handling capabilities. As mentioned in Ch. 1, size scales inversely to frequency; thus, for frequencies around 30 GHz and above, a tape helix would be very small, extremely fragile, difficult to produce, and have low power-handling capabilities. The FW/SWG geometry does not suffer from fragility, however, because the structure is often milled from a solid copper

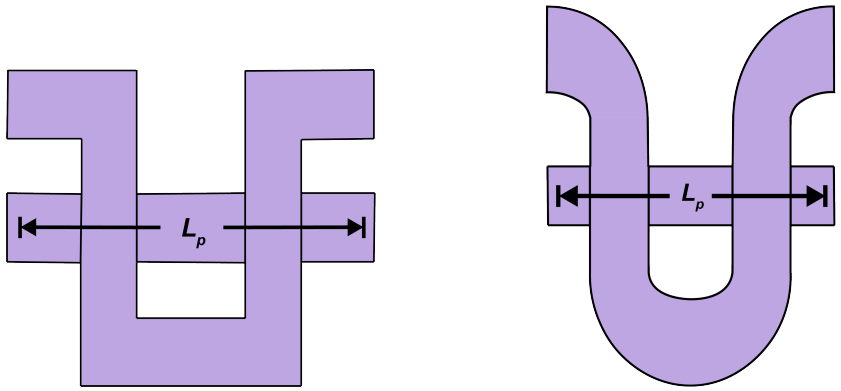

(a) Folded waveguide single period.

(b) Serpentine waveguide single period, which is a special case of the FW.

Figure 2.7: 2D projection of typical folded waveguide and serpentine waveguide structures. FW/SWG TWTs are fabricated by linking numerous periods of length L_p in series.

block or even 3D printed (see [16] for more details about a 3D printed W-band SWG). Further discussion follows regarding CC's and FW/SWG's ability to handle higher power, but at a reduced bandwidth.

2.3.2 Coupled-Cavity Power Handling and the Energy Quality Factor

The ability for a TWT to handle high power levels is extremely important, especially in the scope of this research project. General CC TWTs provide this ability due to their high quality factor, Q. To find Q, we start from electromagnetic energy conservation and Poynting's theorem,

$$\frac{\partial}{\partial t}\underbrace{\int d^3x\,\frac{1}{4}\left(\epsilon|\hat{\boldsymbol{E}}|^2+\mu|\hat{\boldsymbol{H}}|^2\right)}_{U}+\underbrace{\int_S dA\,\hat{n}\cdot\frac{1}{2}\mathbb{R}\{\hat{\boldsymbol{E}}\times\hat{\boldsymbol{H}}\}}_{P_{walls}}=0 \tag{2.2}$$

where $\hat{\boldsymbol{E}}$ is the complex electric field vector, $\hat{\boldsymbol{H}}$ is the complex magnetic field vector, $\epsilon=\epsilon_r\epsilon_0$ is the material permittivity, ϵ_r is the material's relative permittivity, ϵ_0 is the permittivity of free space (vacuum), $\mu=\mu_r\mu_0$ is the material permeability, μ_r is the material's relative permeability, μ_0 is the permeability of free space, and $\hat{n}$ is the surface normal unit vector.

For cavity modes, the average energy stored in $\hat{\boldsymbol{E}}$ and $\hat{\boldsymbol{H}}$ is the same, i.e.,

$$\int_V d^3x \, \frac{\epsilon}{4}|\hat{\boldsymbol{E}}|^2 = \int_V d^3x \, \frac{\mu}{4}|\hat{\boldsymbol{H}}|^2 \, . \tag{2.3}$$

The loaded quality factor's definition in terms of of energy is given by:

$$Q_e = \frac{\omega U}{P_d} \, . \tag{2.4}$$

Substituting in for the stored energy and dissipated power, we get

$$Q_e = \frac{\omega}{c}\frac{1}{R_s}\sqrt{\frac{\mu}{\epsilon}}\frac{\int d^3x \, |\hat{\boldsymbol{H}}|^2}{\int dA \, |\hat{\boldsymbol{H}}_{\boldsymbol{z}}|^2} \tag{2.5}$$

where ω is the angular frequency, U is the stored energy in the resonant cavity, and $P_d = \frac{1}{2}\int dA \, R_s|\hat{\boldsymbol{H}}_{\boldsymbol{z}}|^2$ is the power dissipated in the cavity walls due to an imperfect conductor, $\hat{\boldsymbol{H}}_{\boldsymbol{z}}$ is the magnetic field's tangential component, $R_s(\sigma) = \sqrt{\frac{\omega\mu}{2\sigma}}$ is the surface resistance, and σ is the material's conductivity. The use of c in (2.5) assumes the CC is under vacuum.

In other words, the quality factor is proportional to the energy stored in the cavity divided by the energy dissipated in RF one cycle. Coupled-cavity TWTs are also capable of handling higher power because they are often made from solid copper or copper alloys. Such material has high conductivity, σ, resulting in less power being dissipated in the walls. This results in higher Q_e as well as higher output power.

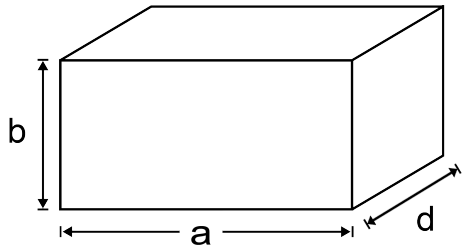

Figure 2.8: Rectangular resonant cavity.

2.3.3 Coupled-Cavity Cutoff Frequency and Bandwidth Quality Factor

Though CC and CC-like (i.e., FW/SWG) circuits have the ability to handle greater power levels, their bandwidth is much less than that of a tape helix. In fact, tape helices are extremely wide band because they do not have a lower cutoff frequency like a coupled-cavity or a waveguide. Rectangular coupled-cavities are simply a series connection of rectangular resonant cavities, each with a cutoff frequency given by

$$\omega_c = \frac{1}{\sqrt{\mu\epsilon}}\sqrt{\left(\frac{m\pi}{a}\right)^2 + \left(\frac{n\pi}{b}\right)^2 + \left(\frac{p\pi}{d}\right)^2} \tag{2.6}$$

where $m \in \mathbb{N}$, $n \in \mathbb{N}$, and $p \in \mathbb{N}$ (i.e., m, n, and p are positive integers) denote the TE_{mnp} mode, $\frac{1}{\sqrt{\mu\epsilon}} = c$ in vacuum, a is the cavity's broadwall dimension, b is the cavity's narrow wall dimension, and d is the cavity's length (see Fig. 2.8). A rectangular waveguide is a special case of rectangular resonant cavity where $d \gg p\pi$, so $\frac{p\pi}{d} \to 0$. Using this limit in(2.6), we arrive at the cutoff frequency for a rectangular waveguide:

$$\omega_c = \frac{1}{\sqrt{\mu\epsilon}}\sqrt{\left(\frac{m\pi}{a}\right)^2 + \left(\frac{n\pi}{b}\right)^2} \tag{2.7}$$

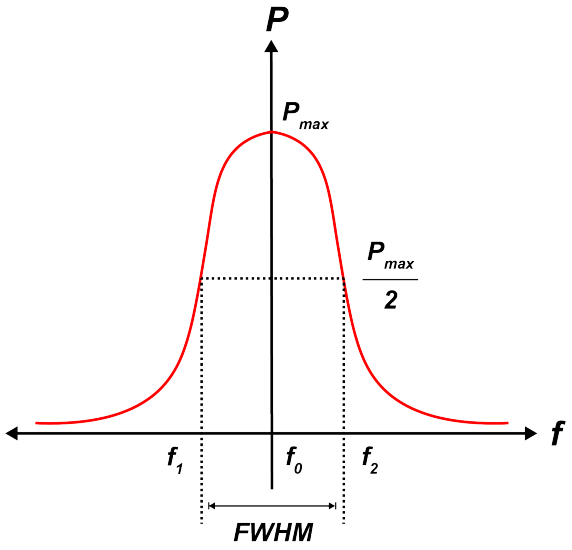

Figure 2.9: Definition of the FWHM in terms of frequency and power. The resonant frequency is f_0.

Equation (2.7) can be used to calculate the cutoff frequency for FWs and SWGs because their cross-sections are rectangular.

We now introduce the bandwidth quality factor, Q_f, which is defined as

$$Q_f = \frac{f_0}{\Delta f} \tag{2.8}$$

where f_0 is the resonant frequency and $\Delta f = f_2 - f_1$ is the bandwidth at the full-width half maximum (FWHM) (see Fig. 2.9). In terms of frequency and power, the FWHM is defined as the bandwidth over which the cavity's resonating power is greater than half (i.e., 3 dB below) the resonant frequency's power, P_{max}.

Q_e and Q_f are not identical, but when Q is large, $Q_e \approx Q_f$. This is the case for rectangular resonant cavities resulting in low bandwidth because $Q_f \propto \frac{1}{\Delta f}$.

2.4 Device Selection for Misalignment Studies

2.4.1 Circuit Geometry

Careful consideration must be made when choosing a device to fulfill the the requirements set forth in Ch. 1. TWTs with a helical SWS offer extreme wide band capabilities, but in the mm-wave regime, however, the helix would have to be very small. This significantly limits its ability to handle high power. In fact, in Ka-band, a helix TWT would be limited to only about 500 W or less (at frequencies above Ka-band, this power level only decreases). As mentioned previously, a helix of small size is very delicate, as well. Coupled-cavity TWTs, on the other hand, are capable of handling high power levels, but at significantly lower bandwidths as discussed in Sec. 2.3.2 and Sec. 2.3.3. It is apparent a device is needed that serves as a compromise between the helix TWT and CC TWT. Let us further investigate the FW/SWG geometry.

Unlike true CC TWTs where individual resonant cavities are coupled through small apertures, or "irises," the FW/SWG geometry is a continuous waveguide that is bent in between the interaction regions, or gaps. In fact, the bending waveguide nature behaves as a serial network of coupled cavities, each of which are fairly low-Q. Recall from (2.8) that the SWG's lower quality factor results in a larger available bandwidth than a CC TWT.

SWG structures are also much more robust than a helix because they are often milled from solid copper (or copper alloy) blocks or 3D printed rather than making use of a fragile helix. Power levels in these solid structures can increase by one or more orders of magnitude compared to those a helix is capable of obtaining.

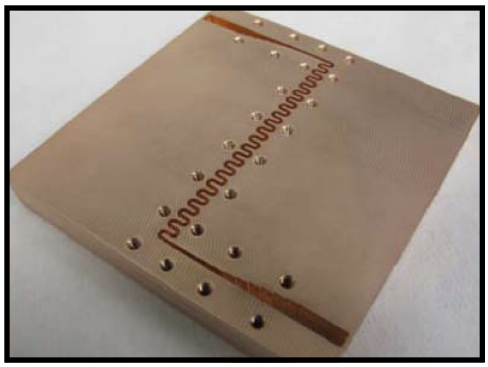

Figure 2.10: SWG circuit (without a beam tunnel) milled from a copper block in the half-plane. The full structure consists of two of these half-planes vertically positioned and brazed together to form a single, closed device. Adapted from [17].

2.4.2 Circuit Fabrication Techniques

It has become evident the FW/SWG geometry is a desirable geometry for this project due to its characteristics akin to helix TWTs and CC TWTs. The device's fabrication method must now be decided, which must be in accordance with precision alignment. One method in which this is possible is to use the computer numerical control (CNC) milling technique to remove material from a solid copper block as mentioned previously. This can be done by milling the FW/SWG circuit out of a single block, or, milling the circuit out of two blocks split in the half-plane as shown in Fig. 2.10. When fabricating the circuit in the half-plane, the final device is composed of joining the circuit's lower half to its upper half using precision alignment techniques. Holes for the pinned joint alignment technique are visible in Fig. 2.10.

The fabrication aspect ratio, defined as the depth the end mill cuts into the block divided by the end mill's diameter, is of great importance when machining such devices. Milling the FW/SWG circuit out of a single block is not desirable due to the high aspect ratio; a larger aspect ratio often results in manufacturing imperfections thus degrading the RF signal. Milling

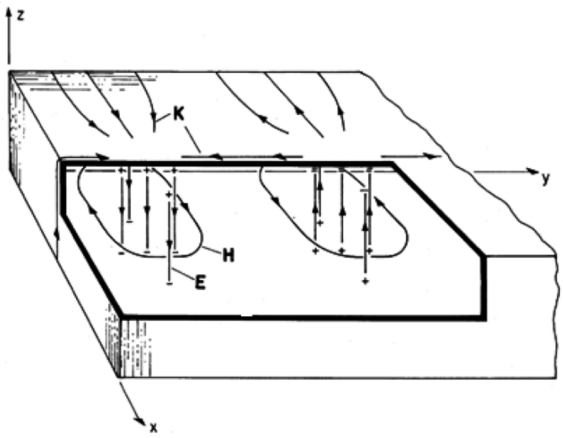

Figure 2.11: The electric field, $\boldsymbol{E}$, magnetic field, $\boldsymbol{H}$, and surface currents, $\boldsymbol{K}$, in a rectangular waveguide. Adapted from [18].

the circuit in its half-plane reduces the aspect ratio, and therefore, the number of imperfections, leading to a more precisely fabricated structure.

The beam tunnel also benefits from the half-plane fabrication technique. In the half-plane, the end mill must only cut a short distance into the block whereas if the FW/SWG is milled from a single block, the end mill must cut a hole through the block that is the length of the entire circuit (this is known as a "hole-pop"). Any minute misalignments of the block to the mill when the mill begins cutting will be exacerbated further down the circuit. The end mill is more susceptible to bending away from a straight path further into the circuit, as well, if the hole-pop method is used.

A SWG circuit for a W-band TWT was fabricated using the methods described above in [19] and [20] revealing further anecdotal evidence half-plane fabrication is superior to a single block fabrication. When milled from a single block, the FW/SWG structure still requires a top plate that acts as the waveguide's second narrow wall in order to complete the waveguide's circuit. Other studies performed by the group in [19] and [20] examined this single-block fabrication with a cover and numerous cold tests revealed higher RF reflection and consequently, lower RF

transmission in the single-block design. Such behavior can be explained by examining the surface currents in a rectangular waveguide which are given by the relation:

$$\boldsymbol{K} = \hat{n} \times \boldsymbol{H} \tag{2.9}$$

where $\boldsymbol{K}$ is the surface current in A/m, $\hat{n}$ is the surface normal unit vector, and $\boldsymbol{H}$ is the magnetic field vector. Using Fig. 2.11 and the right hand rule, it becomes clear the surface currents in the half-plane are null whereas the surface currents in the top plane are nonzero [18, 21].

2.4.3 Final Circuit Selection

The details in the discussion presented in Sec. 2.4.1 and Sec. 2.4.2 must be considered carefully when choosing a circuit geometry. For our research, we selected to use a half-plane split block SWG as it offers a unique compromise in both power and bandwidth as well as the opportunity to quantify the consequences misalignments in precision manufactured devices may have on the RF signal.

Chapter 3: Serpentine Waveguide Circuit Theory

3.1 Overview

Now that the SWG SWS has been chosen, it is beneficial to introduce a brief review of FW/SWG circuit theory. In this chapter, an overview of the general dispersion relation is presented and the analytical transmission line model for the FW/SWG is then introduced followed by the application of this model to a circuit misaligned in the half-plane. An accurate model for the FW/SWG allows us to create a well-defined dispersion relation for the device which can then be later supplied to large-signal interaction codes such as CHRISTINE or TESLA in which gain calculations are performed (see [22], [23], and [24] for more details). The chapter concludes with a discussion of the Pierce impedance, which is commonly used to quantify the beam-wave interaction strength in VEDs.

3.2 Dispersion Relation

3.2.1 Background

A discussion is warranted regarding dispersion relationships before the transmission line model for FW/SWGs is derived. Such relations permeate the microwave, electron device, and plasma physics industries. Though dispersion, or a type of signal distortion, exhibits unique

characteristics in different systems, understanding its behavior is imperative to understanding the overall device behavior.[2] In TWTs, it is particularly important because the intersection of the dispersion curve with the beam line is the frequency at which the strongest beam-wave interaction occurs in the amplifier.

The power of the relationship between ω and k becomes more evident when it is plotted on a 2D coordinate axis. Take the dispersion relation for the lowest mode in a straight, rectangular waveguide, the TE_{10} mode, for example:

$$\omega^2(k) = \omega_{c,10}^2 + k^2c^2 \tag{3.1}$$

where $\omega_{c,10} = \frac{\pi c}{a}$ is the rectangular waveguide's cutoff frequency for the TE_{10} mode [17]. The plot corresponding to (3.1) is shown in Fig. 3.1. This plot makes it easy visualize and possible to extract both the phase velocity,

$$v_{ph} \equiv \frac{\omega}{k} \, , \tag{3.2}$$

and the group velocity,

$$v_g \equiv \frac{\partial \omega}{\partial k} \, , \tag{3.3}$$

of the microwave signal in the in the waveguide. Plotting $\omega(k)$ also allows for the inclusion of the light line (the dotted trace in Fig. 3.1), which gets its name from the fact its slope is equivalent to the speed of light, c. In later sections, a beam line will also be added to the SWG dispersion curve plots to demonstrate the beam-wave interaction between the microwave signal and the electron beam propagating through a SWG's beam tunnel.

[2] In general, the dispersion relation relates the frequency, ω, to the wavenumber, k. In other words, it is expressed as $\omega(k)$ or $k(\omega)$.

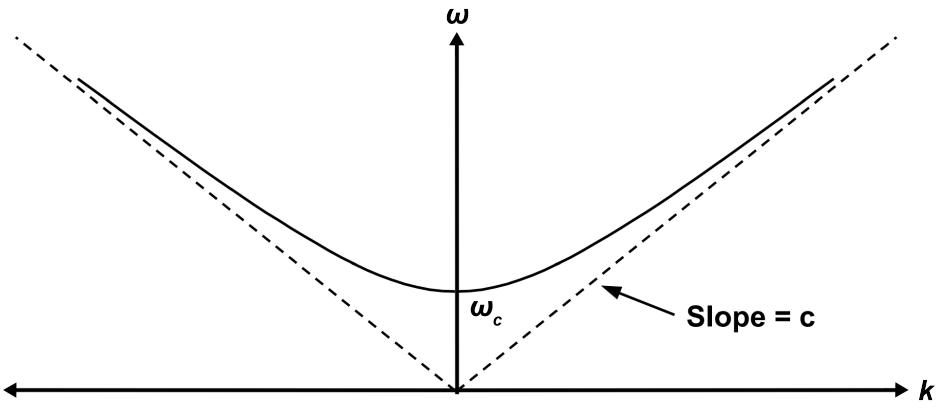

Figure 3.1: Dispersion curve for a rectangular waveguide with cutoff frequency ω_c. Adapted from [8].

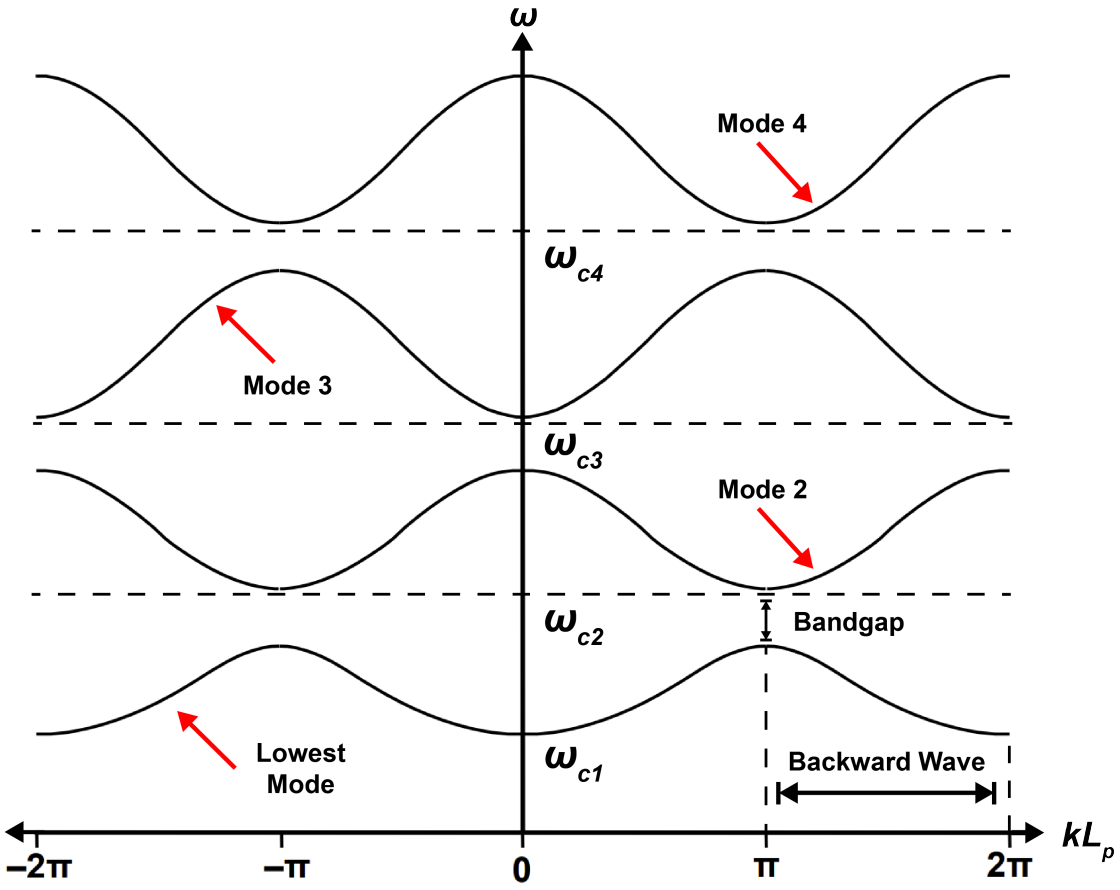

Figure 3.2: Dispersion curves for a periodic vane-loaded waveguide with period L_p. Adapted from [8].

As the wavenumber, k, approaches zero, it is evident from (3.1) that $\omega \to \omega_{c,10}$ and $v_g \to 0$. It thus becomes clear why this is called "cutoff;" the signal's group velocity is null and therefore, no wave is propagating. As k increases, however, $v_g \to c$. When $k > 0$, $v_g > 0$ and the wave propagates in the forward ($+\hat{z}$) direction. When $k < 0$, however, $v_g < 0$ and the wave propagates in the backwards ($-\hat{z}$) direction (this phenomenon is known as a "backward wave").

3.2.2 Periodic Structures and the SWG

Plotting dispersion curves for periodic structures is particularly beneficial as even more device properties can be inferred from the $\omega(k)$ diagram. Take the case of a periodically vane-loaded waveguide with period length L_p, whose dispersion curves are depicted in Fig. 3.2, for example.

It is evident from Fig. 3.2 that for periodic structures, the dispersion relation also becomes periodic; this gives light to interesting structural properties. The dispersion curves' periodicity arises from spatial harmonics present in the device. One of the first observations to note in the curves is the existence of upper *and* lower cutoff frequencies for each mode (recall cutoff occurs when $v_g = {}^{\partial\omega}/_{\partial k} = 0$). When the term "cutoff" is used, however, it is generally assumed to still be referring to the mode's lower cutoff frequency unless otherwise stated. In Fig. 3.2, each mode's lower cutoff frequency is labeled as ω_{c1}, ω_{c2}, ω_{c3}, etc. in order of increasing mode cutoff. For rectangular waveguides, the lowest mode is always the TE_{10} mode. The higher mode numbers and cutoff frequencies are dependent on the waveguide geometry, of course.

Introduction of upper and lower cutoff frequencies in periodic structures also leads to bandgaps (also commonly known as "stop bands"). Bandgaps are defined as regions of frequency

where signals with a purely real wavenumber do not propagate through the device. In other words, there are certain frequency ranges in the periodic structure for which waves are evanescent. This occurs between a lower mode's upper cutoff frequency and a higher mode's lower cutoff frequency. See Fig. 3.2 for an illustration of a bandgap in a periodic structure.

The SWG's dispersion relation can be derived by considering the dispersion relation for the TE_{10} mode in a straight waveguide expressed in (3.1) and the electric field's phase in the SWG given by

$$\phi_z = kL_s + \pi\left(2n+1\right) \tag{3.4}$$

where L_s is the RF signal path length from one gap to the second gap through the serpentine bend and $n \in \mathbb{Z}$ (i.e., n is in the set of all positive and negative integers) denoting the spatial harmonics in the periodic SWG [17]. Combining (3.1) and (3.4) yields a normalized dispersion relationship for the SWG for the TE_{10} mode:

$$\left(\frac{f}{f_c}\right)^2 = 1 + \frac{a^2}{L_s^2}\left[\frac{\phi_z}{\pi} - (2n+1)\right]^2 \tag{3.5}$$

where f is the operating frequency [17].

3.3 SWG Transmission Line Model

An alternate expression for the SWG's dispersion relation can be derived by considering the structure's transmission line model. First, we examine a FW with its beam tunnel and waveguide bends modeled using shunt admittances, Y_s, as depicted in Fig. 3.3 and its unfolded transmission line equivalent depicted in Fig. 3.4. From Fig. 3.4, it is possible to write the equations for the

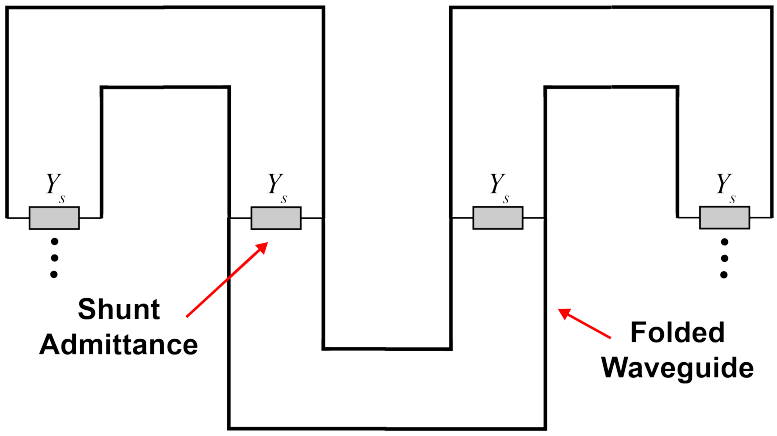

Figure 3.3: FW geometry with shunt admittances used to model the beam tunnel and SWG bends. Adapted from [24].

voltage and current waves propagating through the structure as

$$\begin{cases} V(z) = V_+ e^{ikz} + V_- e^{-ikz} & (3.6) \\ I(z) = \dfrac{1}{Z_0}\left(V_+ e^{ikz} - V_- e^{-ikz}\right) & (3.7) \end{cases}$$

where V_+ and V_- are the forward and backward wave amplitudes, respectively, z is the spatial coordinate, $Z_0(\omega) = \frac{Z_{00}}{\sqrt{1-\omega_c^2/\omega^2}}$ is the frequency-dependent line characteristic impedance, Z_{00} is a constant determined by impedance matching, ω_c is the cutoff frequency, ω is the operating frequency, and the wavenumber, k, is given by [24]:

$$k = \frac{1}{c}\sqrt{\omega^2 - \omega_c^2}\,. \tag{3.8}$$

Next, we demand $V(-L) = -V_{n-1}$, $V(0) = V_n$, and $V(L) = -V_{n+1}$ at the boundaries and plug these relations into (3.6) and (3.7). The FW/SWG is a periodic structure, so we look for solutions of the form $V_{n\pm1} = V_n e^{\pm i\theta}$ where θ is the phase [24]. Replacing the complex exponentials using Euler's formula and substituting $\alpha = kL$ as the phase advance across

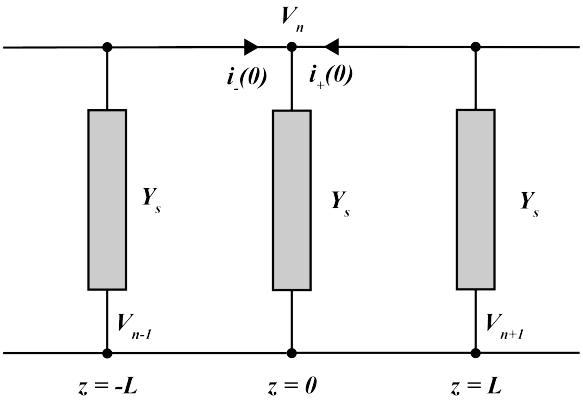

Figure 3.4: Unfolded transmission line model for the FW/SWG. The voltage across the admittances alternates polarity at each distance L along $\hat{z}$ due to the π phase shift in the electric field across a single period of the FW/SWG. Adapted from [24].

structure, we arrive at the transmission line model dispersion relation for the FW/SWG,

$$\Delta \sin \alpha + \cos \alpha = -\cos \theta \tag{3.9}$$

where $\Delta = \frac{Z_0 Y_s}{i2}$ [24]. Rewriting Δ in terms of known quantities yields

$$\Delta(\omega) = \frac{\Delta_{00}}{\sqrt{1 - (\omega_c/\omega)^2}} \left(\frac{\omega_0}{\omega} - \frac{\omega}{\omega_0} \right) \tag{3.10}$$

where $\Delta_{00} = \frac{Z_{00}}{2} \sqrt{\frac{C_{sh}}{L_{sh}}}$ is the normalized impedance, $\omega_0 = \frac{1}{\sqrt{L_{sh} C_{sh}}}$ is the resonant frequency, C_{sh} is the capacitance, and L_{sh} is the inductance [24].

3.4 Transmission Line Model for a Misaligned Structure

The analysis presented in Sec. 3.3 above can also be extended to analytically model structural misalignments, which are of particular interest to our group. More specifically, we are interested in misalignments in the electric field's plane (i.e., the half-plane depicted in Fig. 2.10)

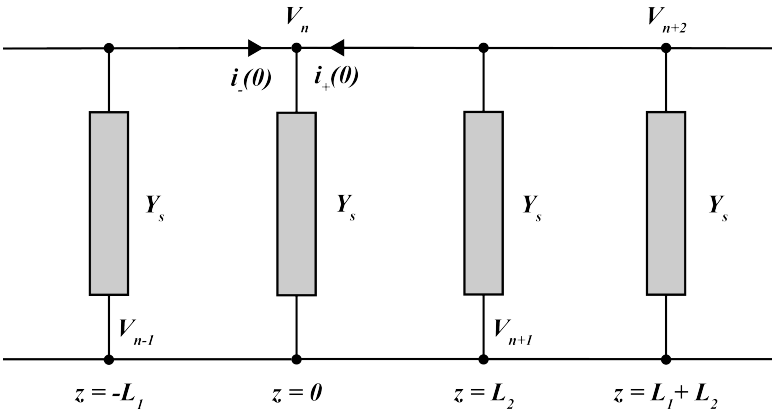

Figure 3.5: Unfolded transmission line model for the FW/SWG misaligned in the half-plane. Note that $L_1 \neq L_2$.

due to our choice fabrication method. Misalignments in the electric field's plane can begin to be modeled from modifying Fig. 3.4 by introducing periods, or cells, of different lengths $L_1 \neq L_2$.

Once again starting from (3.6) and (3.7) and performing an analogous analysis as for the aligned structure in Sec. 3.3, we arrive at the boundary conditions

$$\begin{cases} i_- (0) = I (0) = -\dfrac{i}{Z_0 \sin \alpha_1} \left(V_n \cos \alpha_1 + V_{n-1} \right) & (3.11) \\ i_+ (0) = I (0) = -\dfrac{i}{Z_0 \sin \alpha_2} \left(V_n \cos \alpha_2 + V_{n+1} \right) & (3.12) \end{cases}$$

where $\alpha_1 = kL_1$ and $\alpha_2 = kL_2$ are the phase advances across the differenet periods, each of which with unequal period lengths [24]. Constructing two Kirchhoff current law (KCL) equations and carrying out the subsequent algebra leads to the transmission line model dispersion relation for the misaligned FW/SWG:

$$2 \cos \beta = \sin \alpha_1 \sin \alpha_2 \left(2\Delta + \frac{\cos \alpha_1}{\sin \alpha_1} + \frac{\cos \alpha_2}{\sin \alpha_2} \right)^2 - \left(\frac{\sin \alpha_1}{\sin \alpha_2} + \frac{\sin \alpha_2}{\sin \alpha_1} \right) \tag{3.13}$$

where β is the phase advance across two periods [24].

3.5 Beam-Wave Interaction and the Pierce Impedance

The beam-wave interaction is the primary energy transfer method in many VEDs, including a SWG TWT. A common way to quantify this energy transfer is by calculating the interaction impedance, otherwise known as the Pierce impedance. In general, the Pierce impedance is given by:

$$Z_P(k_n) = \frac{|\hat{E}_{z,n}(k_0)|^2}{2\,(k_n)^2\,P(k_0)} \tag{3.14}$$

where $|\hat{E}_{z,n}|$ is the magnitude of the complex electric field along the beam tunnel axis, $k_n = k_0 + \frac{2\pi n}{L_p}$ is the wavenumber for the n^{th} Floquet spatial harmonic ($n \in \mathbb{Z}$), k_0 is the fundamental Brillouin zone's (i.e., $n = 0$) wavenumber, L_p is the SWG period length (that includes two beam tunnel gaps), and $P(k_0)$ is the time-averaged power flux through the SWG at a given phase [25]. The Brillouin zone is another method for describing the circuit's periodicity and for the SWG, the Brillouin zone is periodic in 2π. Most SWG structures have beam-wave interactions that occur in the first ($n = 1$) or second ($n = 2$) Brillouin zone [25].

To calculate the complex electric field's magnitude along the beam tunnel, it is necessary to make use of Floquet's theorem and space harmonics. Floquet's theorem states [26]:

> *For a given mode of propagation at a given steady-state frequency, the fields at one cross-section differ from those one period away only by a complex constant.*

If we express the complex electric field, $\hat{E}$ in terms of its magnitude, E, and phase as

$$\hat{E} = E(x, y, z)\, e^{-k_0 z} e^{-i\omega t} \tag{3.15}$$

and apply Floquet's statement, we can write the electric field as a Fourier series [26]:

$$E(x,y,z)\,e^{-k_0 z} = \sum_n \hat{E}_n e^{i(2\pi n/L_p)z} e^{-k_0 z} \tag{3.16}$$

where $\hat{E}_n$ is the electric field's n^{th} space harmonic. Rearranging and integrating (3.16) from 0 to L_p leads to an expression for $\hat{E}_n$ [26]:

$$\hat{E}_n = \frac{1}{L_p}\int_0^{L_p} dz\, E e^{-k_0 z} e^{[k_0 - i(2\pi n/L_p)]z} = \hat{E}_n\left(k_0\right)\ . \tag{3.17}$$

Notice how the first spatial phase in (3.17) is negative (known as a phase "delay") whereas the second spatial phase's real part is positive (known as a phase "advance"). Great care must be taken with these signs when using different EM simulation software. For example, when inputting a spatial phase into the computational electromagnetic (CEM) code Computer Simulation Technology (CST) Microwave Studio Suite (more commonly referred to as "CST Studio Suite," or, more simply, "CST") by Dassault Systèmes, a negative must be added if the calculation in (3.17) is to be done. In other words, CST Studio's eigenmode solver uses a phase advance [25]. The High Frequency Simulation Software (HFSS) finite-element method (FEM) CEM code from Ansys, however, uses a phase delay, so no additional negative sign is needed in front of the spatial phase in this software package.

Finally, the time-averaged power flux through the SWG, $P\left(k_0\right)$, can be calculated from the Poynting vector, i.e.,

$$P\left(k_0\right) = \frac{1}{2}\int_S \left(\hat{\boldsymbol{E}} \times \hat{\boldsymbol{H}}^*\right) \cdot d\boldsymbol{S}\ , \tag{3.18}$$

or equivalently,

$$P\left(k_0\right) = \frac{1}{2}\frac{1}{L_p}\frac{d\omega}{dk}\int_V \epsilon\hat{\boldsymbol{E}}\cdot\hat{\boldsymbol{E}}^*\,dV \tag{3.19}$$

where $\hat{\boldsymbol{H}}^*$ is the complex conjugate of the magnetic field, $\boldsymbol{S}$ is the surface normal through which the power flux is calculated, $\frac{d\omega}{dk} = v_g$ is the group velocity,

$$U_E \equiv \frac{1}{2}\int_V \epsilon\hat{\boldsymbol{E}}\cdot\hat{\boldsymbol{E}}^*\,dV \tag{3.20}$$

is the time-averaged electrical stored energy in a single SWG period,

$$U_B \equiv \frac{1}{2}\int_V \mu\hat{\boldsymbol{H}}\cdot\hat{\boldsymbol{H}}^*\,dV \tag{3.21}$$

is the time-averaged magnetic stored energy in a single SWG period, and

$$\int_V \epsilon\hat{\boldsymbol{E}}\cdot\hat{\boldsymbol{E}}^*\,dV = U_E + U_B = 2U_E = 2U_B\,. \tag{3.22}$$

In other words, the time-averaged electrical stored energy is equal to the time-averaged magnetic stored energy in one SWG period [26]. Equation (3.22) is just another way to express equation (2.3). A more detailed discussion regarding calculating the Pierce impedance in FW and SWG structures is discussed in [25], [27], and [28].

Chapter 4: Ka-Band Circuit Optimization

4.1 Overview

Before the W-band circuit design process begins, it was decided to first start by designing a SWG circuit at Ka-band. Ka-band is a lower frequency band than W-band. The lower frequencies, and consequently, longer wavelengths, require a SWG with larger dimensions that allows for more forgiving fabrication tolerances. Starting with these larger dimensions allows for a slightly larger error margin during the manufacturing process thus allowing us to gain insights into potential adjustments to make when working in W-band where the SWG circuit's tolerances are much smaller than at Ka-band.

This section begins with a concise review of scattering parameters (commonly referred to as "S-parameters") that will be the primary figure of merit in the circuit's design optimization. A brief description of the circuit's optimization process will then be presented. The design efforts focus on adding waveguide tapers to transition from the SWG size to the WR-28, or standard Ka-band rectangular waveguide size, as well as adding a step transition to improve matching between the SWG and the tapers. The HFSS FEM CEM code from Ansys is used to perform all simulations herein unless otherwise noted.

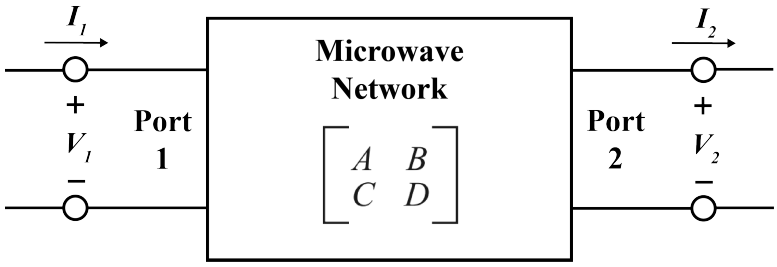

Figure 4.1: A general 2-port microwave network with an $ABCD$ transmission matrix. Adapted from [14].

4.2 Brief Review of Scattering Parameters

Scattering parameters are often used in microwave network analysis; they provide an intuitive approach to understanding transmitted waves through and reflected waves from devices. In real world applications, especially in high-power microwave (HPM) systems, this is extremely important. It is essential to minimize the device's reflection, or S_{11}, to avoid a large reflected signal in the interaction region. Such a reflection can induce self-oscillations when the gain of the forward going circuit wave in the presence of the electron beam is higher than the reflection coefficient. In this way the value of S_{11} determines the maximum stable gain the device can achieve.

To better understand S-parameters, consider the two-port microwave network depicted in Fig. 4.1. In this two-port network, there is a voltage V_1 across Port 1, a current I_1 flowing into Port 1, a voltage V_2 across Port 2, and a current I_2 flowing out of Port 2. The scattering matrix, $[\boldsymbol{S}]$, can be expressed in a matrix equation involving the incident and reflected microwave signals, or V^+ and V^-, respectively. For a two-port network fed by identical transmission lines or waveguides:

$$\begin{bmatrix} V_1^- \\ V_2^- \end{bmatrix} = \begin{bmatrix} S_{11} & S_{12} \\ S_{21} & S_{22} \end{bmatrix} \begin{bmatrix} V_1^+ \\ V_2^+ \end{bmatrix} \tag{4.1}$$

where each element of the matix, $[\boldsymbol{S}]$, is given by [14]:

$$S_{ij} = \left. \frac{V_i^-}{V_j^+} \right|_{V_k^+ = 0 \text{ for } k \neq j} . \tag{4.2}$$

Qualitatively, (4.2) states that when $i \neq j$, the j^{th} port is being driven with an incident wave and the reflected wave at the i^{th} port is being measured when all other incident waves, except for at the j^{th} port, are null. In other words, all other ports are terminated with matched loads to absorb all incident power and to avoid any reflected waves. When $i = j$, $S_{ij} = S_{ii}$ and (4.2) states a reflected wave is being observed at the i^{th} port when all other ports are terminated with matched loads [14]. This analysis can be extended to N-dimensions for a N-port microwave network by simply increasing the dimensions of $[\boldsymbol{S}]$ [14]:

$$\begin{bmatrix} V_1^- \\ V_2^- \\ \vdots \\ V_N^- \end{bmatrix} = \begin{bmatrix} S_{11} & S_{12} & \dots & S_{1N} \\ S_{21} & S_{22} & \dots & S_{2N} \\ \vdots & \vdots & \ddots & \vdots \\ S_{N1} & S_{N2} & \dots & S_{NN} \end{bmatrix} \begin{bmatrix} V_1^+ \\ V_2^+ \\ \vdots \\ V_N^+ \end{bmatrix} . \tag{4.3}$$

Often times microwave networks are cascaded to form larger networks, as in the case of a SWG periodic structure. Analysis of such networks is simplified by introducing the $ABCD$ transfer matrix, which is closely related to the $[\boldsymbol{S}]$ matrix. For the two-port network in Fig. 4.1, it is possible to construct the $ABCD$ transfer matrix by first writing the equations for the voltages

and currents at the ports:

$$\begin{cases} V_1 = AV_2 + BI_2 & (4.4) \\ I_1 = CV_2 + DI_2 & (4.5) \end{cases}$$

which can be expressed as the matrix equation

$$\begin{bmatrix} V_1 \\ I_1 \end{bmatrix} = \begin{bmatrix} A & B \\ C & D \end{bmatrix} \begin{bmatrix} V_2 \\ I_2 \end{bmatrix} \tag{4.6}$$

where the 2×2 matrix is the $ABCD$ transfer matrix [14]. The voltages and currents in cascaded devices like the SWG can easily be calculated by simply multiplying the $ABCD$ transfer matrices.

Further building on the SWG transmission line model discussed in Ch. 3, it is possible to rewrite (3.11) and (3.12) as an $ABCD$ transmission matrix for a single SWG half-period [24]. The matrix entries for the SWG half-period are as follows:

$$\begin{cases} A = -\cos\alpha + iZ_0Y_s\sin\alpha & (4.7) \\ B = iZ_0\sin\alpha & (4.8) \\ C = -2Y_s\cos\alpha + \dfrac{i}{Z_0\sin\alpha}\left(Z_0^2Y_s^2\sin^2\alpha - \cos^2\alpha + 1\right) & (4.9) \\ D = -\cos\alpha + iZ_0Y_s\sin\alpha & (4.10) \end{cases}$$

To find the transmission matrix for the full SWG period, simply multiply the half-period $ABCD$ matrix with itself.

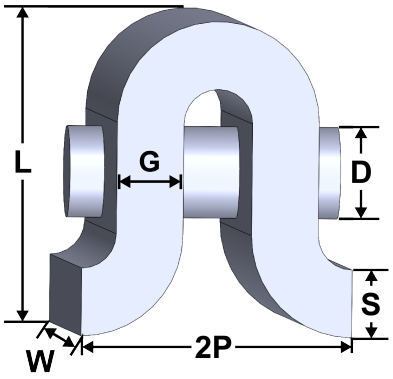

Figure 4.2: SWG parameter variable names and definitions. Note that $2P = L_p = 2L_g$.

4.3 Preliminary Structure

The preliminary circuit used to start the Ka-band design optimization efforts was based on designs presented in [17] and [29]. The SWG circuit dimension variable names are defined herein as shown in Fig. 4.2. The initial vacuum space circuit is depicted in Fig. 4.3 with select dimensions listed in Table 4.1.

With the SWG's vacuum space model created using CAD, it is now possible to simulate the circuit in Fig. 4.3 using HFSS to get an initial idea of its S-parameters. The circuit's reflection, or S_{11}, and transmission, or S_{21}, are plotted in Fig. 4.4. These early results are encouraging because it is clear that the reflection is at or below 20 dB down across most of the band (from about 30 GHz – 40 GHz).[3] The reflection only exceeds this level in the band's lower portion, i.e., from 26.5 GHz – ≈30 GHz).

The transmission, or S_{21}, exhibits great performance, as well. S_{21} is greater than -3 dB from about 27 GHz upward. In other words, more than half the signal is transmitted through the

[3]The -20 dB mark was chosen as the initial maximum threshold S_{11} should not exceed for the majority of the band due to results presented in [17] and [29] for a similar structure.

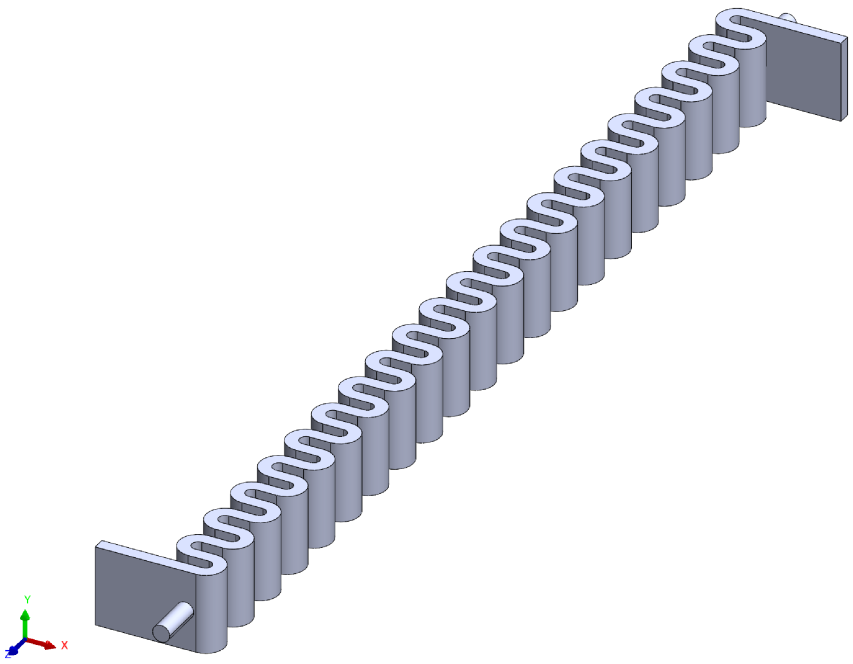

Figure 4.3: Preliminary Ka-band vacuum space SWG model based on designs presented in [17] and [29].

Preliminary Ka-Band SWG Circuit Dimensions

SWG Circuit Parameter	Value (Customary)	Value (Metric)
P	71.00 mil	1.8034 mm
D	48.00 mil	1.2192 mm

Table 4.1: Select dimensions for the preliminary Ka-band SWG vacuum space model. There are $N = 21.5$ periods in the model.

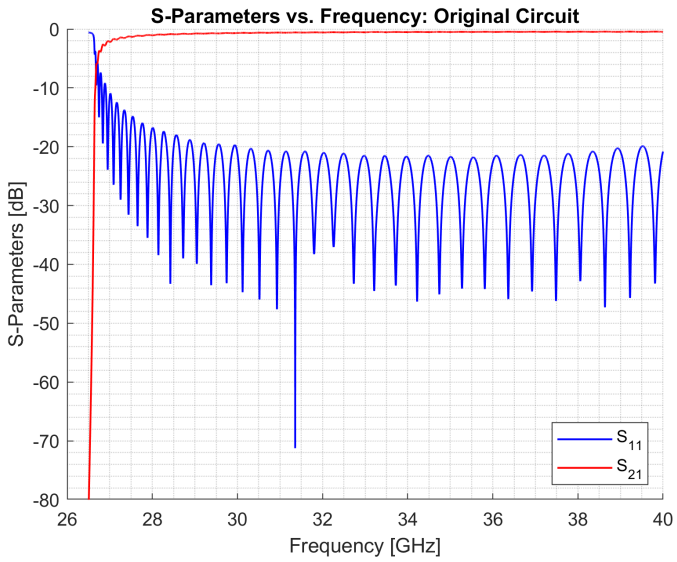

Figure 4.4: HFSS simulation results for the reflection and transmission S-parameters for the preliminary Ka-band vacuum space model.

device for frequencies above 27 GHz. It is also important to note the standing wave, exhibited by the periodic-like nature in S_{11}, is fairly uniform across the band; there are no abrupt disturbances visible thus indicating a well-behaved structure.

Many of the Ka-band dimensions and misalignments are expressed in the customary unit "mil," or one one-thousandth ($^1/_{1000}$) of an inch. The original Ka-band CAD model was created using customary units, hence these units carried over to later models. Table 4.2 serves as a reference chart reflecting common customary values used throughout this thesis and provides their metric equivalent.

4.4 Tapers with a Matching Section

The preliminary SWG vacuum space design presented in Sec. 4.3 shows promising results, but it is not yet suitable for fabrication; its broadwall, W, and its straight section narrow wall, G,

Quick Conversions

Value (Customary)	Value (Metric)
1 mil	0.0254 mm
2.2 mil	0.0559 mm
5 mil	0.1270 mm
7.5 mil	0.1905 mm
10 mil	0.2540 mm
15 mil	0.3810 mm
20 mil	0.5080 mm

Table 4.2: Reference chart for converting common values used in this thesis from their customary value to their metric equivalent. Recall 1 mil = 0.001 in.

do not adhere to the WR-28 standard rectangular waveguide size for Ka-band. The dimensions for the WR-28 are listed in Table 4.3. As is, the SWG would not be able to connect to other equipment due to its customized dimensions and for this reason, it is necessary to add transitions from the SWG size to the standard WR-28 size. These transition sections are referred to as "tapers" herein.

Adding tapers presents a new challenge in the circuit design; such an addition could introduce a mismatch between the SWG and the WR-28 causing additional, undesired reflections. A single-section impedance transformer in the form of a step transition (shown in Fig. 4.5) can be added at the SWG/taper boundary to minimize such reflections. The taper design also reduces unwanted reflections by taking an discrete number of matching sections and shortening their length to an infinitesimally small values, thus creating a continuous taper [14]. More information about single-section transformers, multi-section transformers, and tapered lines can be found in Chapter 5 of [14]. The complicated nature of these calculations makes this optimization effort ideal for CEM codes. In the case of this structure, the design was optimized in FEM code Analyst

WR-28 Dimensions

Operating Frequency	Broadwall, a (in. [mm])	Narrow Wall, b (in. [mm])
26.5 GHz – 40 GHz	0.28 [7.112]	0.14 [3.556]

Table 4.3: Dimensions for the WR-28, or the standard waveguide size for Ka-band. "WR" stands for "rectangular waveguide" and the number following it is the waveguide's broadwall dimension in mil, divided by 10 [30]. In this case, the broadwall dimension is 280 mil, hence the designation "WR-28." Most rectangular waveguides are designed such that $a \approx 2b$.

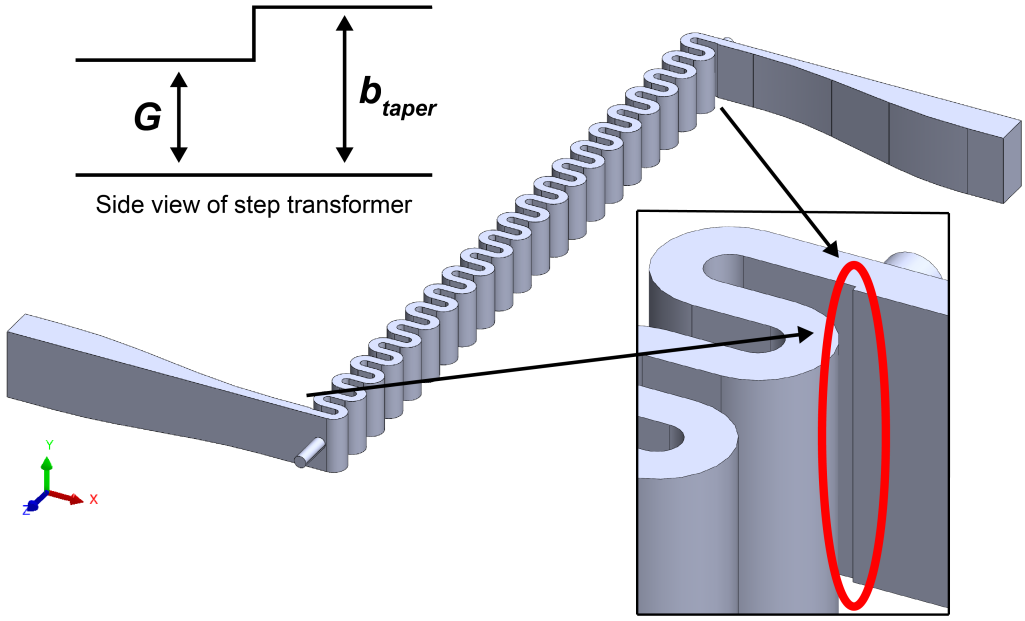

Figure 4.5: Ka-band vacuum space circuit with added right angle step impedance transformer and tapers to the WR-28 standard waveguide size.

Ka-Band SWG Step Transformer and Taper Dimensions

SWG Circuit Parameter	Value (Customary)	Value (Metric)
b_{taper}	39.50 mil	1.0033 mm
Transformer distance from beam tunnel ($\lvert dx \rvert$)	55.00 mil	1.3970 mm
Taper length	1.2205 in	31.00 mm

Table 4.4: Step transition and taper length dimensions for the Ka-band vacuum space model depicted in Fig. 4.5. The taper length is defined as the distance from the step transformer to the taper's end where its dimensions match those of a WR-28. The remaining circuit parameters are identical to those listed in Table 4.1.

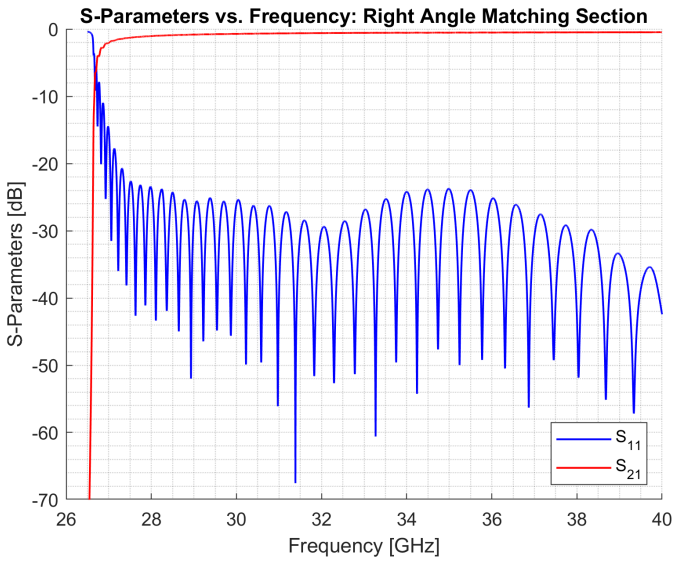

Figure 4.6: HFSS simulation results for the reflection and transmission S-parameters for the Ka-band vacuum space model with a right angle step transformer and tapers to the WR-28 standard waveguide size.

by Cādence. Other than the addition of the step transformer and the tapers, the SWG circuit dimensions remain unchanged from those listed in Table 4.1. The HFSS simulation results for the structure depicted in Fig. 4.5 are shown in Fig. 4.6.

Fig. 4.6 confirms adding the impedance transformer and the tapers to the WR-28 improved (i.e., reduced) the circuit reflection, or S_{11}. The frequency at which the reflected signal drops below -20 dB has shifted from about 30 GHz in the original structure to about 27 GHz in the structure with the step transformer. Above 27 GHz, the maximum reflection observed is about -24 dB and some standing wave peaks are seen to be as low as -35 dB. This is a significant improvement from the original Ka-band structure without the transformer or tapers where the minimum standing wave peak was observed to be approximately -21 dB.

The microwave signal transmission through the device with the step transformers and tapers is almost identical to the original structure's transmission also indicating a good match. No degradation in S_{21} was observed by adding the transformers or tapers.

4.5 Circuit Matching with a Fillet

4.5.1 Replacing the Right Angle Step Transformer

It has become evident introducing an impedance matching transformer along with optimized tapers improves the Ka-band circuit's S_{11} performance. Fabricating a right angle step transition at the Ka-band's small size is impractical, however; an end mill with an extremely small radius is required to make such a cut. This cut is not impossible, but the end mill's aspect ratio would be quite high and as discussed in Sec. 2.4.2, this is undesirable. The high aspect ratio could also result in extraneous fabrication imperfections, which should also be avoided because the RF signal in the mm-wave regime is sensitive to imperfections on the same order of magnitude as it's wavelength. Machining a more precise right angle would take significant amount of time and increase cost compared to an alternative geometry selection, as well.

One plausible method to avoid the problems discussed in the previous paragraph is to potentially replace the right angle step transition with a more smooth transition such as an arc segment from a circle with a larger radius (such a surface will be referred to as a "fillet"). This is depicted in Fig. 4.7. Introducing the fillet allows an end mill with a larger radius to be used thus ensuring more accurate and reliable fabrication. While the fillet may solve manufacturing woes, it is imperative to confirm its addition does not degrade the SWG's RF performance.

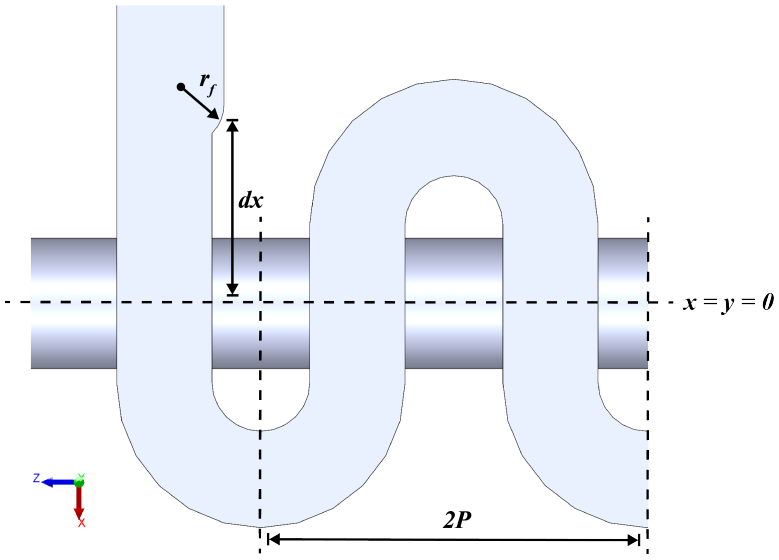

Figure 4.7: Side view of the SWG structure with a smooth fillet of radius r_f located a distance $|dx|$ away from the beam tunnel axis (z-axis) replacing the right angle step transition. Note that in this coordinate system, $dx < 0$.

Preventing an increase in S_{11} and a decrease in S_{21} while maintaining fabrication integrity is the primary goal of adding a fillet to the SWG circuit. Replacing the right angle step transformer with a fillet immediately gives rise to the question of the fillet's location. The fillet's curved surface has finite length in $\hat{x}$ unlike the step transformer. For this reason, we can hypothesize there are three fillet positions of interest. They are:

1. The **original** location of the right angle step transition, i.e., the fillet arc's midpoint is located in the same position as the original step. The absolute location is represented by the expression $x = dx$. This location will be referred to as the "original match location" herein.

2. **In front** of the original step transition's position by a distance of the fillet radius, $r_f = R$, divided by 2. In other words, the fillet is moved towards the beam tunnel's axis (the $+\hat{x}$-direction) in Fig. 4.7 by a distance of $R/2$ so that the boundary where the fillet's upper

point meets the taper with narrow wall dimension, b_{taper}, is located where the original step transition was positioned. The absolute location is represented by the expression $x = dx + {}^{R}/_{2}$ (note the plus sign because the transformer's original position is $dx < 0$). This displacement will be referred to as "towards the beam tunnel" herein.

3. **Behind** the original step transition's position by a distance of the fillet radius, $r_f = R$, divided by 2. In other words, the fillet is moved away from the beam tunnel's axis (the $-\hat{x}$-direction) in Fig. 4.7 by a distance of ${}^{R}/_{2}$ so that the boundary where the fillet's lower point meets the SWG with narrow wall dimension, G, is located where the original step transition was positioned. The absolute location is represented by the expression $x = dx - {}^{R}/_{2}$ (note the minus sign because the transformer's original position is $dx < 0$). This displacement will be referred to as "away from the beam tunnel" herein.

It is most logical to start with a small fillet to closely emulate a right angle and to ensure a good match is preserved with a fillet. Thus, we pick the initial fillet radius $R = 2.2$ mil and simulate the device's RF response when the fillet is located at the three positions listed above. The HFSS simulations for these three geometries are depicted in Fig. 4.8a and Fig. 4.8b.

It is clear from the results shown in Fig. 4.8a and Fig. 4.8b there is no significant deviation in S_{11} or S_{21} for the geometry including the fillet with radius $R = 2.2$ mils from the right angle transformer geometry. In fact, it is hard to discern the different traces in many areas.

In terms of the reflection magnitude, the largest observed change in Fig. 4.8a is only a $\approx$2 dB increase at 39.5 GHz, which is negligible at levels below 30 dB down. The standing wave in the same figure is also largely preserved across all three fillet locations, except for the one case where the fillet is moved towards the beam tunnel (the red trace in Fig. 4.8a) in the

Fillet Radii and Location Summary

Fillet Radius, R	Location, x
10 mil	dx
	$dx + {}^{R}/_{2}$
	$dx - {}^{R}/_{2}$
15 mil	dx
	$dx + {}^{R}/_{2}$
	$dx - {}^{R}/_{2}$
20 mil	dx
	$dx + {}^{R}/_{2}$
	$dx - {}^{R}/_{2}$

Table 4.5: Summary of the fillet radii and their locations used in HFSS simulations

frequency range 36.5 GHz – 37.5 GHz. Here, there is a slight interruption in the standing wave's periodicity, but it it quickly regains its periodic nature at ≈37.5 GHz.

The S_{21} results also closely adhere to the step transformer case for all three fillet positions. There are only two small deviations from the curve at ≈30 GHz and ≈37 GHz, each with a magnitude less than 0.05 dB, which is negligible.

It is safe to conclude replacing the right angle step transformer with a smooth fillet does not cause a deterioration in the microwave signal based on these results. The next step is to increase the fillet radius to lower the end mill's aspect ratio.

4.5.2 Increasing the Fillet Radius

Three fillet radii were chosen in accordance with corresponding end mill sizes that would lower the aspect ratio and provide more manufacturing precision. Each fillet radius was also

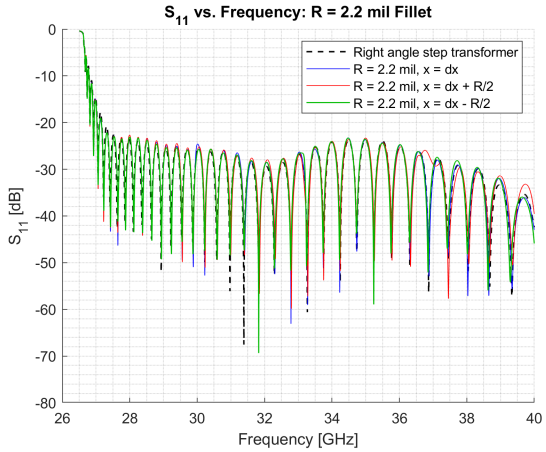

(a) Simulated reflection in the $R = 2.2$ mil geometry.

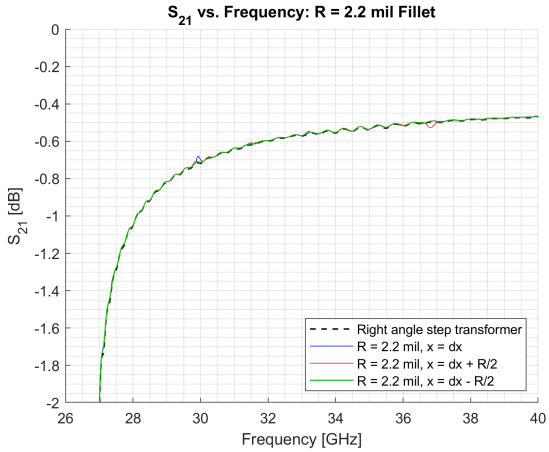

(b) Simulated transmission in the $R = 2.2$ mil geometry.

Figure 4.8: HFSS S_{11} and S_{21} simulation results for $R = 2.2$ mil fillet located at the original match location, i.e., $x = dx$ (blue trace); moved towards the beam tunnel, i.e., $x = dx + {}^{R}/_{2}$ (red trace); and moved away from the beam tunnel, i.e., $x = dx - {}^{R}/_{2}$ (green trace), compared to the right angle transformer response.

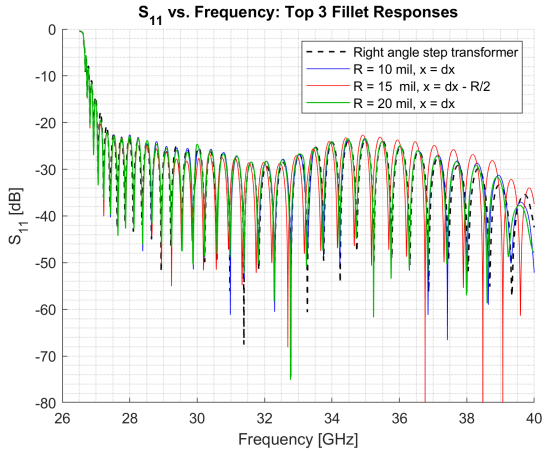

(a) HFSS simulations for the three geometries with fillets exhibiting the lowest reflection.

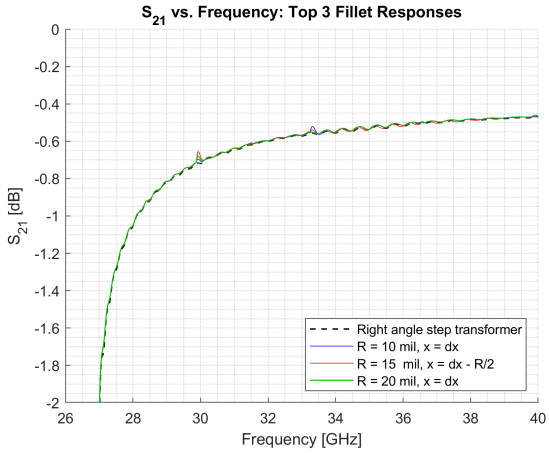

(b) HFSS simulations for the three geometries with fillets exhibiting the highest transmission.

Figure 4.9: HFSS S_{11} and S_{21} simulation results for the three geometries with fillets exhibiting the lowest reflection and the highest transmission. These geometries include the fillets $R = 10$ mil located at $x = dx$ (blue trace), $R = 15$ mil located at $x = dx - {}^{R}/_{2}$ (red trace), and $R = 20$ mil located at $x = dx$ (green trace).

tested at the three possible locations outlined in Sec. 4.5.1 for a total of nine simulations. These radii and their positions are summarized in Table 4.5. All nine geometries were then simulated in HFSS and the three exhibiting the best S_{11} and S_{21} responses are shown in Fig. 4.9.

Given the simulation results presented in Fig. 4.9, it was decided to select the fillet with radius $R = 15$ mil positioned a distance $x = dx - {}^{R}/_{2}$ (the red trace) from the beam tunnel axis. This fillet geometry exhibited the lowest reflections for a significant portion of the band from ≈28 GHz – ≈33 GHz. Though it did have reflections up to about 6 dB higher than the other fillet responses between ≈37 GHz – ≈40 GHz, its local maximum above 28 GHz is -23 dB at ≈35 GHz, which is still below the -20 dB threshold. The $R = 15$ mil fillet radius also corresponds to a reasonable end mill size with an appropriate aspect ratio whereas the $R = 20$ mil radius end mill may be too large for other circuit features. Thus, the fillet with radius $R = 15$ mil located a distance $x = dx - {}^{R}/_{2}$ from the beam tunnel was chosen to be investigated further.

4.6 Additional Circuit Geometry Adjustments

Additional adjustments were made to the the SWG CAD model with the $R = 15$ mil radius located a distance $x = dx - {}^{R}/_{2}$ from the beam tunnel to see if any additional reduction in reflection could be achieved. The minor adjustments made were also simulated in HFSS, but it was concluded that none of them made a significant impact on the circuit's S_{11} or S_{21}. Most of these adjustments either increased the reflection or degraded the standing wave's periodicity in the cases where S_{11} was reduced.

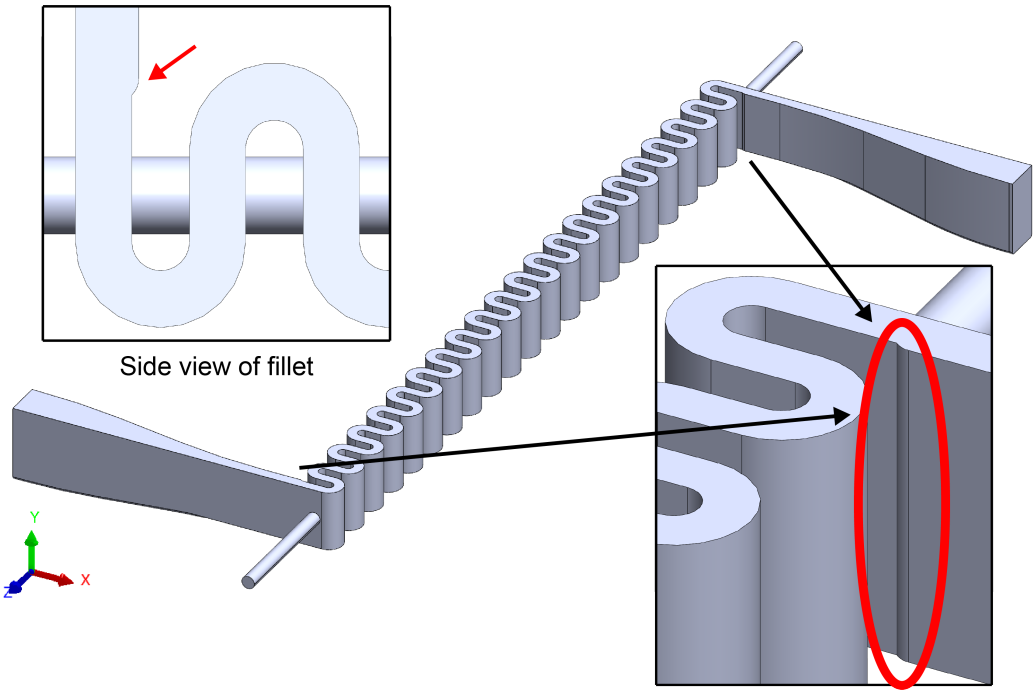

Figure 4.10: Final Ka-band vacuum space model with $N = 21.5$ periods and added fillet with radius $R = 15$ mil located a distance $x = dx - {}^{R}/_{2}$ from the beam tunnel and with tapers from the SWG size to the standard WR-28 size for Ka-band frequencies.

Final Ka-Band SWG Dimensions

SWG Circuit Parameter	Value (Customary)	Value (Metric)
P	71.00 mil	1.8034 mm
D	48.00 mil	1.2192 mm
R	15.00 mil	0.3810 mm
x	62.50 mil	1.5875 mm
l	3.9690 in	10.813 cm

Table 4.6: Select dimensions for the final Ka-band vacuum space model (with $N = 21.5$ periods) depicted in Fig. 4.10. The total circuit length, including the beam tunnel, is given by l.

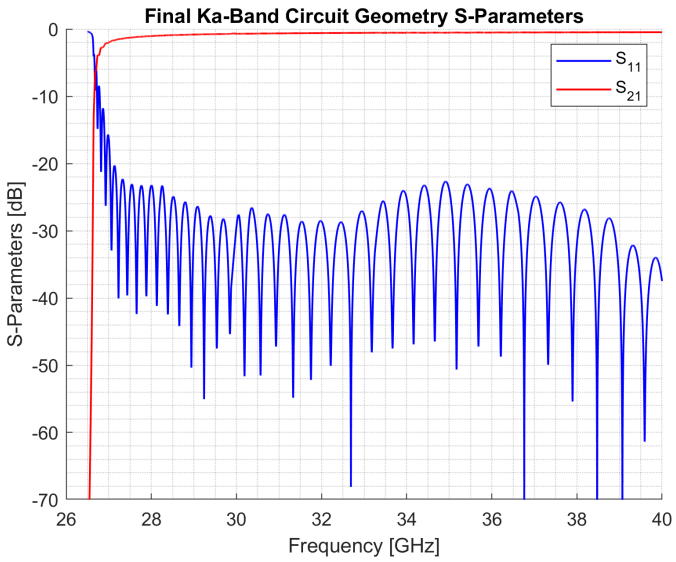

Figure 4.11: HFSS simulation results for the reflection and transmission S-parameters for the final Ka-band vacuum space model depicted in Fig. 4.10.

The S_{21} response of the additional adjustments also adhered closely to the trace for the $R = 15$ mil fillet located a distance $x = dx - {}^{R}/_{2}$ from the beam tunnel (the red trace) in Fig. 4.9b. HFSS simulation results for the aforementioned adjustments are given in Appendix B. Overall, the fillet with radius $R = 15$ mil located a distance $x = dx - {}^{R}/_{2}$ from the beam tunnel exhibited a rough average between the changed parameters, so it was elected to remain with such a geometry and not include any of the additional geometry changes.

4.7 Final Optimized Circuit Geometry Selection

The final optimized SWG geometry to be used for the misalignment studies and thus, to be fabricated, is the geometry including the fillet with radius $R = 15$ mil located a distance $x = dx - {}^{R}/_{2}$ from the beam tunnel and including the tapers from the SWG size to the standard WR-28 waveguide size for Ka-band frequencies. The final CAD model is shown in Fig. 4.10 and the circuit parameters are given in Table 4.6. The simulated S-parameters for this circuit are given in Fig. 4.11.

Notice how in Fig. 4.11 the maximum reflection throughout most of Ka-band is $\approx$25 dB down with only a few frequencies reaching -23 dB. Given this simulation result, we instate a -25 dB maximum reflection threshold herein as a design goal for the Ka-band circuit.

Chapter 5: Misaligned Ka-Band Circuit Modeling

5.1 Overview

It is now possible to begin characterizing the effects misalignments in the Ka-band circuit have on the RF component of the circuit using HFSS. This chapter describes the 1D and 2D misalignment definitions, the model verification in HFSS, and the resulting electromagnetic effects due to circuit misalignments.

5.2 Defining Misalignments

The misalignments studied are those in the x-z plane, which we will define as the circuit's half-plane. It is in this plane that misalignments are most likely to arise given the chosen circuit fabrication technique described in Sec. 2.4.2. Both 1D and 2D misalignments are characterized and all misalignments are in reference to the circuit's stationary lower half. The 2D misalignments can be further categorized into the two sub-groups defined below.

1. **Shear misalignments:** Simultaneous misalignments along both the x-axis and the z-axis. An example of a $(x, z) = (5, 5)$ mil misalignment is shown in Fig. 5.1a.

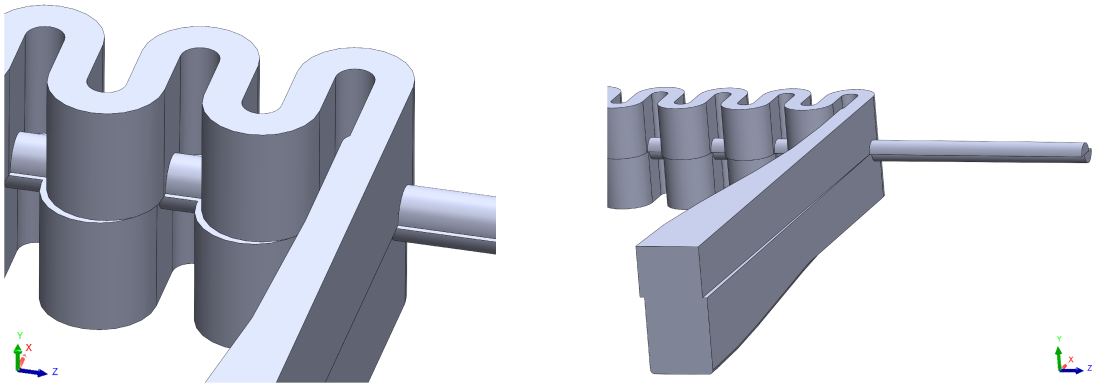

(a) SWG vacuum space model with a $(x, z) = (5, 5)$ mil 2D shear misalignment.

(b) SWG vacuum space model with a $\hat{\phi} = 0.5°$ rotational misalignment.

Figure 5.1: 2D SWG half-plane misalignment definitions.

2. **Rotational misalignments:** Misalignments defined by rotating the circuit's top half about the y-axis in the $\hat{\phi}$-direction relative to the circuit's lower half. Here, the y-axis is normal to the x-z plane and located in the geometric center of the SWG. $\hat{\phi} > 0$ is defined as the clockwise direction in the x-z plane pointing from the x-axis to the z-axis. An example of a $\hat{\phi} = 0.5°$ (clockwise) rotational misalignment is shown in Fig. 5.1b.

More information on creating the CAD models shown in Fig. 5.1a and Fig. 5.1b and the models' S-parameter verification in HFSS is described in Appendix B.3.

The misalignment magnitudes in the following sections were chosen for study based on numerous group members' previous experiences with manufacturing similar RF devices at similar sizes. Misalignments in strictly the $\hat{x}$-direction and the $\hat{z}$-direction are kept below 5 mil, which would be an extreme case of manufacturing error. Based on discussions presented in Ch. 2, it is unlikely misalignments with a magnitude of 5 mil would ever occur; however, it is still beneficial to study the effects of large misalignments to better understand the device as well as being able to create an acceptable tolerance for an operable device. Such a concept could prove

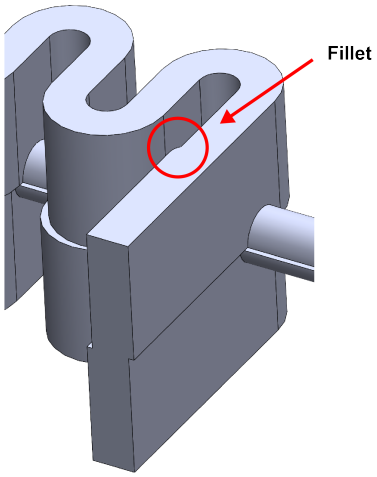

Figure 5.2: SWG vacuum space model with $(x, z) = (5, 5)$ mil misalignment with the matching fillet and without tapers.

useful for potentially loosening manufacturing restrictions to lower the device's cost or to better understand the device's operating limits in a rugged environment where it could be damaged.

5.3 One-Dimensional Misalignments

One-dimensional misalignments are chosen to be studied first in an attempt to gain an understanding of the severity simple misalignments have on the device, if any at all. A detailed discussion of full circuit's scattering parameters are presented in Sec. 5.3.1 followed by further discussion regarding dispersion curve simulations for a single period of the circuit in Sec. 5.3.2.

5.3.1 Scattering Parameters

In order to better understand the SWG circuit itself, the SWG circuit with the matching fillet, but without the tapers to the WR-28 (see Fig. 5.2), were the first simulations performed. The tapers were added back onto the circuit following completing the preliminary simulations.

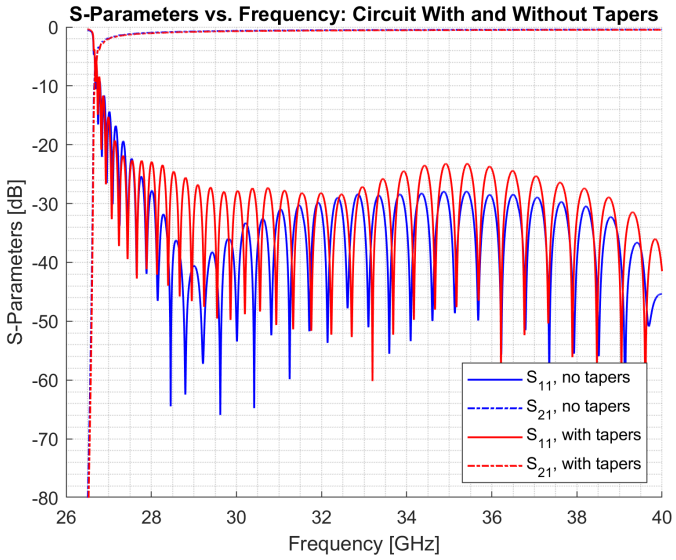

Figure 5.3: S_{11} and S_{21} responses for the SWG circuit (including the matching fillets) with and without the tapers.

The simulated S-parameters for the SWG circuit (include the matching fillets) with and without the tapers are given in Fig. 5.3.

For the 1D misalignment S-parameters depicted in Fig. 5.4, the $(x, z) = (0, 1)$ mil misalignment more closely adheres to the shape of the aligned structure's S_{11} curve whereas the $(x, z) = (1, 0)$ mil misalignment deviates from the aligned structure's response. In fact, there are two local maxima in the $(1, 0)$ misalignment, each exceeding the aligned (or "base case") curve by ≈6 dB at ≈29 GHz and ≈8 dB at ≈30 GHz. Other than these two observations in the 28 GHz – 30 GHz frequency range, the S_{11} curves observed in both 1 mil misalignments closely resemble that of the base case with only three exceptions. At 35.5 GHz, 38.25 GHz, and 39.75 GHz, there are deviations in magnitude between 2 dB and 6 dB. It is also important to note the S_{11} curve's periodicity and the envelope shape is largely preserved in all three traces in Fig. 5.4a except between 28 GHz – 30 GHz. In Fig. 5.4b, there is only a single deviation in the

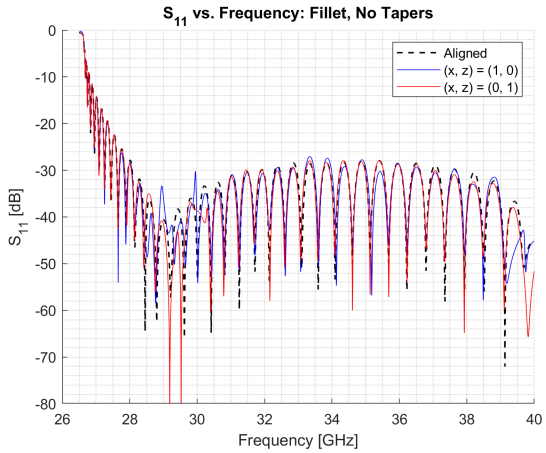

(a) SWG S_{11} response for 1D, 1 mil misalignments in the x-z plane.

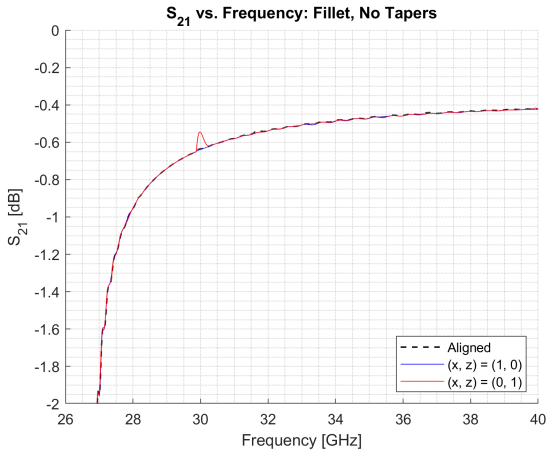

(b) SWG S_{21} response for 1D, 1 mil misalignments in the x-z plane.

Figure 5.4: Reflection and transmission results for 1D, 1 mil misalignments in the SWG structure with the matching fillet and without tapers.

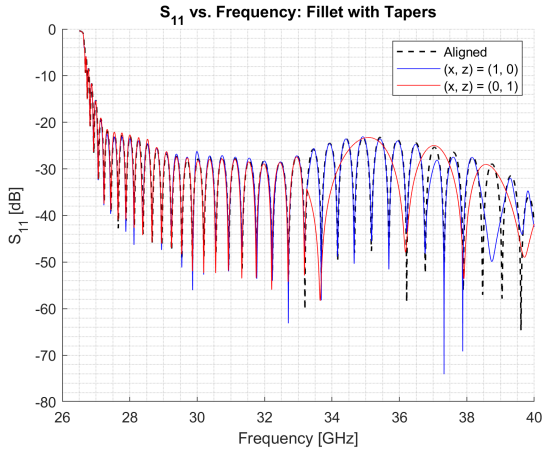

(a) SWG S_{11} response for 1D, 1 mil misalignments in the x-z plane.

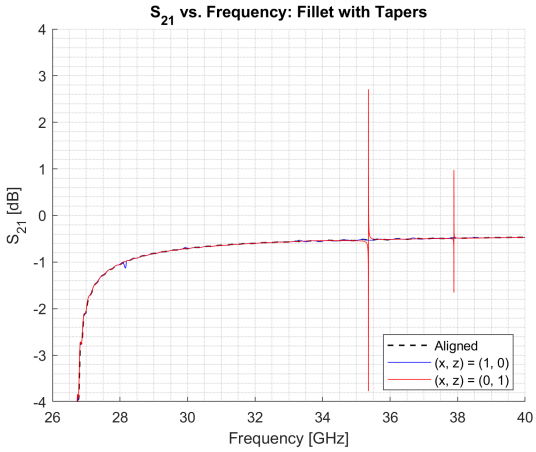

(b) SWG S_{21} response for 1D, 1 mil misalignments in the x-z plane.

Figure 5.5: Reflection and transmission results for 1D, 1 mil misalignments in the SWG structure with the matching fillet and tapers.

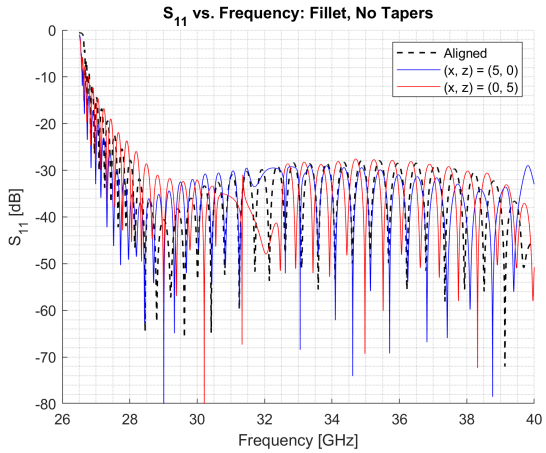

(a) SWG S_{11} response for 1D, 5 mil misalignments in the x-z plane.

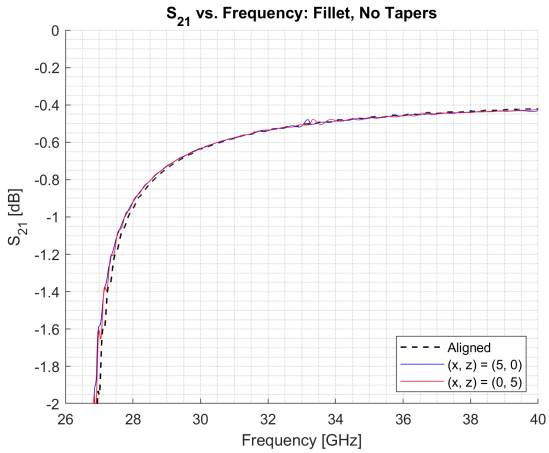

(b) SWG S_{21} response for 1D, 5 mil misalignments in the x-z plane.

Figure 5.6: Reflection and transmission results for 1D, 5 mil misalignments in the SWG structure with the matching fillet and without tapers.

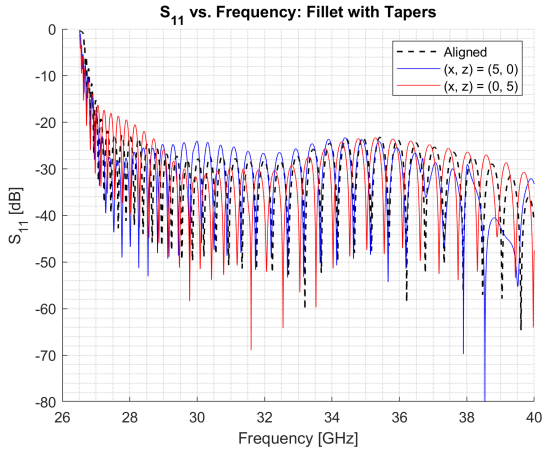

(a) SWG S_{11} response for 1D, 5 mil misalignments in the x-z plane.

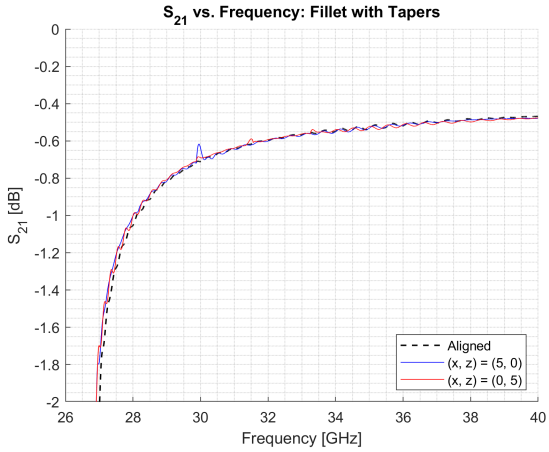

(b) SWG S_{21} response for 1D, 5 mil misalignments in the x-z plane.

Figure 5.7: Reflection and transmission results for 1D, 5 mil misalignments in the SWG structure with the matching fillet and tapers.

S_{21} response from the aligned structure. This is a ≈0.1 dB increase in magnitude occurring at 30 GHz in the $(0, 1)$ misalignment.

Adding the tapers back onto the SWG circuit and performing the same simulations for the 1D, 1 mil misalignments yields very different results than those when the tapers were removed. This behavior is evident in Fig. 5.5. The S_{11} response for the $(1, 0)$ and $(0, 1)$ misalignments in Fig. 5.5a match almost identically to the aligned structure's reflection in both magnitude and standing wave periodicity; there is only a small 2 dB difference in magnitude at 30 GHz for the $(0, 1)$ misalignment. At ≈33 GHz, however, the reflected signal's standing wave period for the $(0, 1)$ misalignment increases greatly, from about 500 MHz to 2.5 GHz, contrary to the base case and the $(1, 0)$ misalignment.

The transmitted signal in Fig. 5.5b also exhibits strange behavior. At ≈35.5 GHz there is a significant disturbance. The $(0, 1)$ misalignment's S_{21} amplitude dips suddenly from about -0.6 dB to about -3.8 dB and then increases sharply to about 2.8 dB signaling there is some amplification occurring (that is almost doubling the transmitted power in this case). A similar phenomenon is observed at ≈38 GHz, however to a lesser effect. Amplification of the RF signal without the presence of an electron beam in a SWG is not expected, so we can attribute these outliers in the data as HFSS numerical artifacts and thus, they can be ignored.

For the 1D, 5 mil misalignments in the SWG structure without the tapers, the S-parameters shown in Fig. 5.6a display a more significant effect on S_{11} than in the 1D, 1 mil misalignment case in Fig. 5.4a. This behavior is expected. The most notable consequence of the 1D, 5 mil misalignment is the loss in the standing wave's periodicity between ≈31.5 GHz and ≈32.5 GHz for the $(x, z) = (5, 0)$ mil misalignment and between ≈30.5 GHz and ≈32.5 GHz

for the $(0, 5)$ mil misalignment. In this same frequency range, the S_{11} magnitude for the $(5, 0)$ mil misalignment remains at approximately the aligned structure's local maximum (≈30 dB down) whereas the magnitude for the for the $(0, 5)$ mil misalignment drops by up to 18 dB. In other words, the $(0, 5)$ mil misalignment in the SWG structure without tapers actually reduces the microwave signal's reflection near 32 GHz.

The periodic nature of the reflected power for the $(0, 5)$ mil misalignment is also observed to experience a slight down shift in frequency, roughly 250 MHz, from the base case. The $(5, 0)$ mil misalignment, on the other hand, exhibits a slight up shift in frequency, roughly 150 MHz, from the base case. Each of the three S_{11} curves' periods are no longer in phase with each other; this is an effect not observed in the 1 mil misalignments.

Contrary to the tapers significantly disrupting the periodicity of the $(0, 1)$ mil misalignment S_{11} curve in Fig. 5.5a, adding the tapers to the 1D, 5 mil misalignments restores the periodicity in reflected wave. This can be seen in the transition from Fig. 5.6a to Fig. 5.7a. The reflected power curves' periodicity do not line up exactly, however.

The 5 mil misalignment with a lower reflection in the structure without the tapers interchanges throughout Ka-band, as well. More specifically, from ≈27 GHz to ≈29 GHz, the $(5, 0)$ mil misalignment has a lower reflection by up to ≈10 dB, from ≈29 GHz to ≈34.5 GHz, the $(0, 5)$ mil misalignment has a lower reflection by up to ≈8 dB, and from ≈34.5 GHz to ≈40 GHz, the $(5, 0)$ mil misalignment has a lower reflection by up to ≈12 dB.

Unlike the numerous disturbances seen in S_{11} in Fig. 5.6a and Fig. 5.7a, no significant signal degradation or improvement is observed in the S_{21} responses plotted in Fig. 5.6b and Fig. 5.7b for the 1D, 5 mil misalignments.

While concluding the discussion about the 1D misalignments, we can make one final observation. The HFSS simulations for the 1 mil and 5 mil misalignments in both the $\hat{x}$- and $\hat{z}$-directions in the SWG structure *without* tapers have a maximum reflection around -30 dB for most of Ka-band. When the tapers are added, however, the maximum reflection for the same misalignments increases by about 6 dB so that the new maximum reflection lies at about -23 dB. This exceeds the desired -25 dB threshold goal set forth in Sec. 4.7, but only by 2 dB. Considering the severity of the 1D misalignments studied in the is section, a 2 dB increase in the microwave signal's reflected power is quite remarkable. In terms of the signal's transmitted power, the only observed outliers are the numerical artifacts that can be ignored.

5.3.2 Dispersion Curves

The dispersion curves for the SWG structure are also important to simulate for the same reasons outlined in Sec. 3.2. It is possible to carry out such simulations in HFSS using the eigenmode solver and primary/secondary (formerly known as "master/slave") boundary conditions on a SWG single period like the one shown in Fig. 4.2. Additional information about the RF signal's behavior in the misaligned device can be extracted by simulating an aligned period as well as 1D misaligned periods.

The information most pertinent to the misalignment studies are the lowest mode's cutoff frequency and the bandgap size in the SWG. Dispersion curves for the aligned structure are depicted in Fig. 5.8. Note that because there are two beam tunnel gaps in the SWG full-cell model (i.e., a single period), the dispersion curves have two periods across the 2π phase advance. In other words, the SWG half-cell (i.e., half of the SWG single period) model's dispersion curves

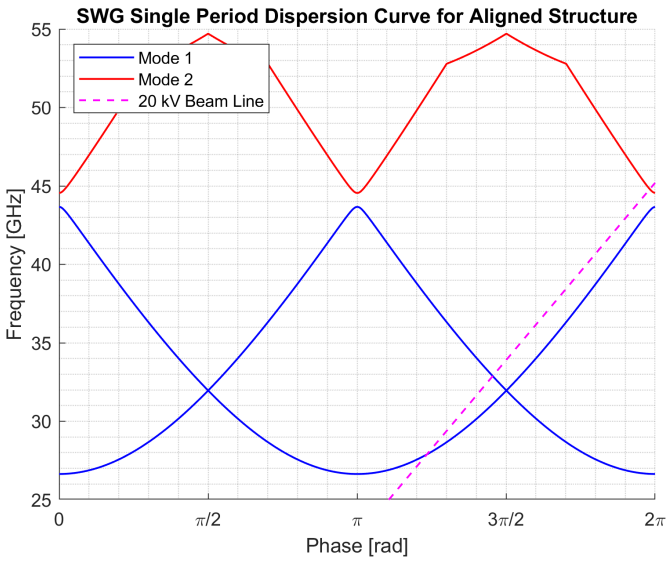

Figure 5.8: Dispersion curves for the first two modes in an aligned single period of the Ka-band SWG geometry obtained using the HFSS eigenmode solver. The SWG's periodic nature is confirmed by the periodic dispersion curves. A 20 kV beam line is added for reference. The horizontal axis is marked in steps of $\pi/10$.

are periodic in π. From the aligned structure in Fig. 5.8, we can extract the cutoff frequency, which is 26.6395 GHz. It is also evident the bandgap at π is 890.81 MHz wide occurring between 43.6641 GHz and 44.5549 GHz with a center frequency of 44.1095 GHz. Data from additional simulations performed for the 1D misalignments is summarized in Table 5.1. The notation $(x, z) = (0, 0)$ is representative of the aligned structure.

The 1D misalignments reduce the lowest mode's cutoff frequency with increasing misalignment magnitude as seen in Table 5.1. Looking more closely at the cutoff frequencies reveals the 1D misalignments along the z-axis lower the cutoff frequency more than the 1D misalignments along the x-axis. Though the cutoff frequencies do change, it is not by a significant amount; in fact, the most significant deviation from the aligned structure's lowest mode cutoff frequency is only 119.40 MHz observed in the $(0, 5)$ misalignment. Such a deviation is small, and in many applications, negligible, at frequencies in Ka-band and above.

1D Misalignment Eigenmode Simulation Data

1D Misalignment	Lowest Mode Cutoff Frequency	Bandgap Width at π
$(x,\ z) = (0,\ 0)$	26.6395 GHz	890.81 MHz
$(x,\ z) = (1,\ 0)$	26.6389 GHz	900.66 MHz
$(x,\ z) = (0,\ 1)$	26.6312 GHz	881.67 MHz
$(x,\ z) = (5,\ 0)$	26.5470 GHz	1223.52 MHz
$(x,\ z) = (0,\ 5)$	26.5201 GHz	854.52 MHz

Table 5.1: Simulated TE_{10} cutoff frequencies and bandgap sizes for 1D misalignments.

It is also evident from Table 5.1 the $(5, 0)$ misalignment has the largest bandgap (1223.52 MHz) that is 332.71 MHz larger than the aligned structure's bandgap. This is a fairly large bandwidth where no modes can propagate, even at Ka-band. More interestingly, however, both 1D misalignments along the x-axis have larger bandgaps than the aligned structure's bandgap whereas both 1D misalignments in along the z-axis have bandgaps that are smaller than the aligned structure's bandgap. In both cases, as the misalignment becomes more severe, the farther the bandgap deviates from the aligned structure's bandgap. Each misalignment bandgap's upper and lower cutoff frequencies do not deviate from the aligned structures by more than 300 MHz, however.

In terms of the dispersion curves' shapes, there were no significant changes for the misaligned geometries' dispersion curves. The only noticeable differences were the slight smoothing of the knees occurring at the phases $^{3\pi}/_{10}$, $^{7\pi}/_{10}$, $^{13\pi}/_{10}$, and $^{17\pi}/_{10}$ in the "Mode 2" trace for the $(5, 0)$ misalignment.

Finally, it is important to note the periodic TE_{10} mode intersects itself at $^{\pi}/_{2}$ and $^{3\pi}/_{2}$. At these points, one wave with $v_g > 0$ intersects another with $v_g < 0$ causing forward and backward waves to possibly couple to one another [31]. This phenomenon could cause instabilities in

the device and hinder the TWT's performance. The intersection at $^{3\pi}/_{2}$ is of particular interest because it occurs in the first Brillouin zone. Instabilities in the Brillouin zone could impact the device more severely because the first Brillouin zone is where the beam-wave interaction typically occurs for a SWG TWT. In the "cold" simulations (i.e., simulations without an electron beam present) presented in Sec. 5.3.1, we can see the disruption in the reflected wave in Fig. 5.6a at 32 GHz, which is the frequency corresponding to the mode crossing at the $^{3\pi}/_{2}$ point. More details regarding the effect instabilities at the $^{3\pi}/_{2}$ point have on TWT gain are described in [31].

5.4 Two-Dimensional Misalignments

Two-dimensional misalignments may also arise as a result of SWG circuit's fabrication technique. Mitigating such misalignments is one of the principle goals of this study, but they may still be present in the final circuit. A discussion about and HFSS simulations for the 2D misalignments introduced in Sec. 5.2 are presented in the following two sections.

5.4.1 Shear Misalignments

The first type of 2D misalignment is the shear misalignment; it has been previously defined in Sec. 5.2. As was done for the 1D misalignments, the first simulations performed for the shear misalignments included the matching fillet without the tapers to the WR-28 to better characterize the SWG circuit itself. The tapers were then added back onto the circuit for the second round of simulations. Symmetrical shear misalignments with magnitude $(x, z) = (1, 1)$ mil, $(x, z) = (2, 2)$ mil, $(x, z) = (3, 3)$ mil, $(x, z) = (4, 4)$ mil, and $(x, z) = (5, 5)$ mil are chosen to be simulated in order to reduce the total number of runs by avoiding simulating each possible

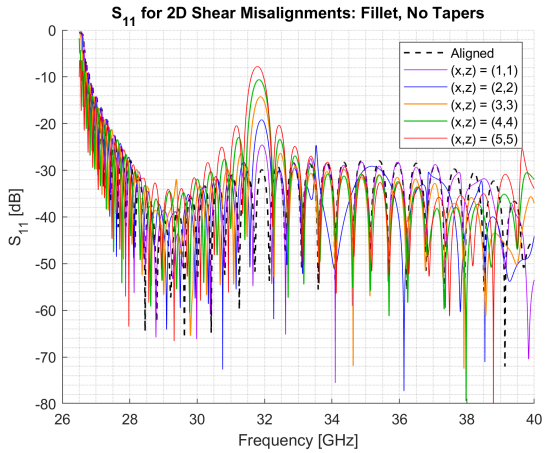

(a) SWG S_{11} response for various shear misalignments in the x-z plane.

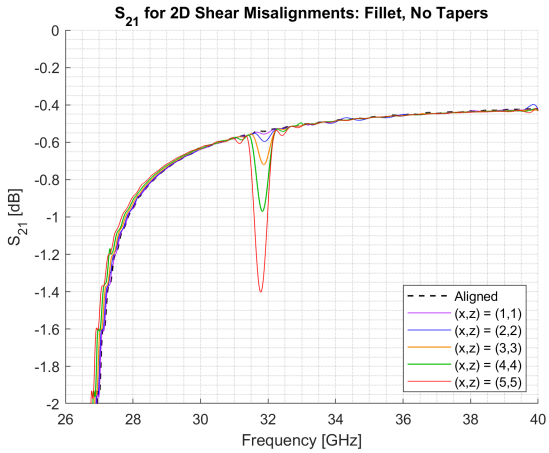

(b) SWG S_{21} response for various shear misalignments in the x-z plane.

Figure 5.9: Reflection and transmission results for symmetrical shear misalignments ranging from 1 mil to 5 mil in the SWG structure with the matching fillet and without tapers.

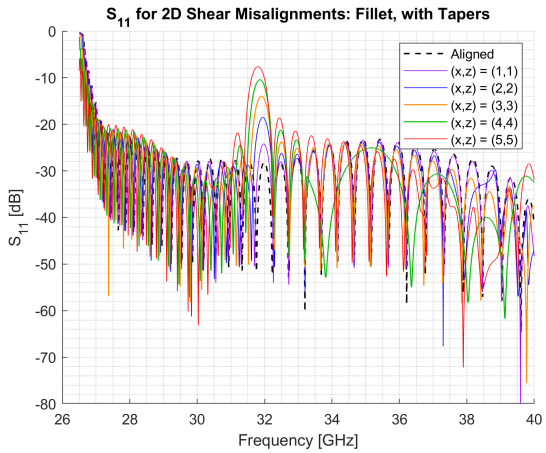

(a) SWG S_{11} response for various shear misalignments in the x-z plane.

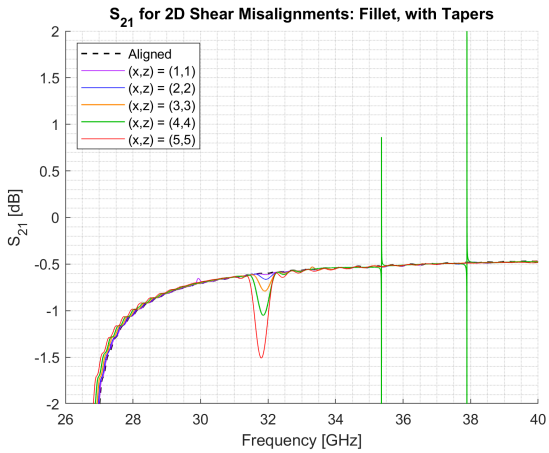

(b) SWG S_{21} response for various shear misalignments in the x-z plane.

Figure 5.10: Reflection and transmission results for symmetrical shear misalignments ranging from 1 mil to 5 mil in the SWG structure with the matching fillet and tapers.

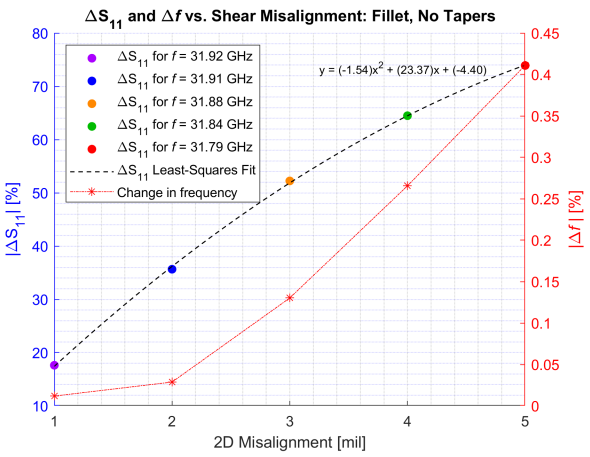

(a) Characteristic changes in the S_{11} local maximum (with least-squares fit) and the frequency at which it occurs.

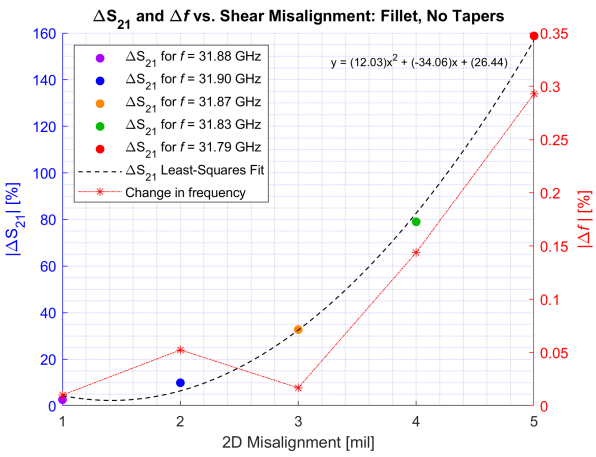

(b) Characteristic changes in the S_{21} local minimum (with least-squares fit) and the frequency at which it occurs.

Figure 5.11: Characteristic changes in the reflected signal's local maximum, the transmitted signal's local minimum, as well as how far each misalignment's local maximum (or minimum) center frequency deviates from the frequency at which the local maximum (or minimum) occurring closest to 32 GHz in the aligned structure resides for shear misalignments in the SWG structure with the matching fillet and without tapers. The horizontal axis is marked in terms of symmetrical shear misalignment, i.e., "1" on the horizontal axis corresponds to the $(1, 1)$ misalignment.

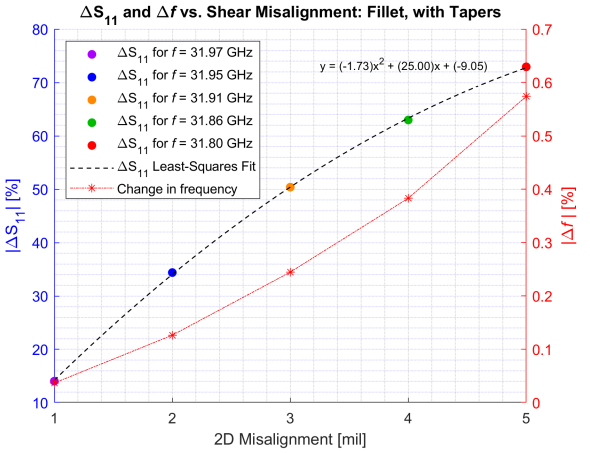

(a) Characteristic changes in the S_{11} local maximum (with least-squares fit) and the frequency at which it occurs.

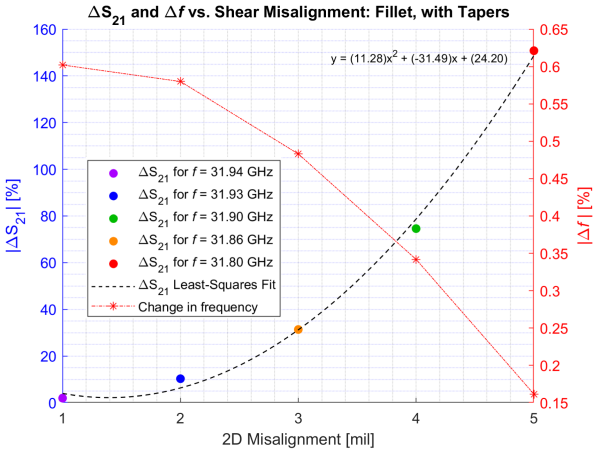

(b) Characteristic changes in the S_{21} local minimum (with least-squares fit) and the frequency at which it occurs.

Figure 5.12: Characteristic changes in the reflected signal's local maximum, the transmitted signal's local minimum, as well as how far each misalignment's local maximum (or minimum) center frequency deviates from the frequency at which the local maximum (or minimum) occurring closest to 32 GHz in the aligned structure resides for shear misalignments in the SWG structure with the matching fillet and tapers. The horizontal axis is marked in terms of symmetrical shear misalignment, i.e., "1" on the horizontal axis corresponds to the $(1, 1)$ misalignment.

shear combination while still being able to efficiently characterize the effects on the microwave signal. The resulting S-parameters are shown in Fig. 5.9 and Fig. 5.10.

The cold simulations in Fig. 5.9 for shear misalignments in the SWG with no tapers reveal a pronounced reflected power level occurring at 32 GHz and consequently, a reduction in the transmitted power at the same frequency. Recall this is the frequency at which the $^{3\pi}/_{2}$ point is located. We can see the 2D shear misalignments' S-parameters have concentrated instabilities around 32 GHz as well as a deterministic increase in reflection and decrease in transmission unlike the 1D misalignments that behaved in a more unpredictable nature.

It can be observed in Fig. 5.9a that the $(5, 5)$ misalignment has a -8 dB reflection near 32 GHz whereas the aligned structure has a -30 dB reflection near the same frequency. This 22 dB increase in the reflected power level is significant. The high reflected power around 32 GHz translates to a decrease in the transmitted power as seen in Fig. 5.9b. The S_{21} local minimum for the $(5, 5)$ shear misalignment drops by 0.85 dB from -0.55 dB to -1.4 dB near 32 GHz. Though this is not as a drastic as the 22 dB change in S_{11}, the 0.85 dB drop in transmitted power is still a significant outlier in the S_{21} trace signifying a disruption in the RF signal.

Further investigation into the deviations observed in S_{11} and S_{21} (or ΔS_{11} and ΔS_{21}) near 32 GHz for the SWG with no tapers reveals a nonlinear increase in both the reflected and transmitted signals as shown in Fig. 5.11. In the case of S_{11}, the increase in magnitude is similar to a curve proportional to a square-rooted term whereas in the case of S_{21}, the decrease in magnitude is quadratic. The changes in frequency (or Δf) at which the local maxima (for S_{11}) occur appear to also be quadratic, but the local minima (for S_{21}) are not as well defined by a three-term, quadratic polynomial, though the change is still nonlinear.

Shear Misalignment Eigenmode Simulation Data

2D Misalignment	Simulated TE_{10} Cutoff Frequency	Simulated bandgap Width at π
$(x,\ z) = (0,\ 0)$	26.6395 GHz	890.81 MHz
$(x,\ z) = (1,\ 1)$	26.6292 GHz	903.68 MHz
$(x,\ z) = (2,\ 2)$	26.6041 GHz	934.58 MHz
$(x,\ z) = (3,\ 3)$	26.5607 GHz	995.83 MHz
$(x,\ z) = (4,\ 4)$	26.5118 GHz	1062.22 MHz
$(x,\ z) = (5,\ 5)$	26.4480 GHz	1155.11 MHz
$(x,\ z) = (1,\ 5)$	26.5173 GHz	863.01 MHz
$(x,\ z) = (5,\ 1)$	26.5418 GHz	1214.25 MHz

Table 5.2: Simulated lower-mode cutoff frequencies and bandgap sizes for 2D shear misalignments.

Adding the tapers back to the SWG structure raises the S_{11} magnitude's envelope as can be observed in Fig. 5.10a. Such behavior is expected considering similar trends are seen in Fig. 5.3. The dramatic increases in the S_{11} magnitude at 32 GHz are again present. The $(5, 5)$ mil misalignment again exhibits the maximum reflected power near 32 GHz with a level of -8 dB, which is the same as the maximum reflected power at the $^{3\pi}/_{2}$ point for $(5, 5)$ misalignment in the SWG without the tapers. Numerical artifacts are again present in Fig. 5.10b for the $(4, 4)$ mil misalignment, but it is possible to ignore them for reasons discussed previously.

The ΔS_{11} and Δf curve shapes for the SWG with tapers are nearly identical to those for the SWG without tapers; they only differ in magnitude. For the circuit with the tapers, the ΔS_{11} curve shifts downwards by about 10% and the Δf curve shifts upwards by approximately 3%. A more drastic change is noticeable for the SWG with tapers' S_{21} Δf curve. Unlike its counterpart in the device without tapers that has a generally nonlinear, increasing trend, Δf in Fig. 5.10b decreases with increasing misalignment. This curve resembles a decreasing quadratic function.

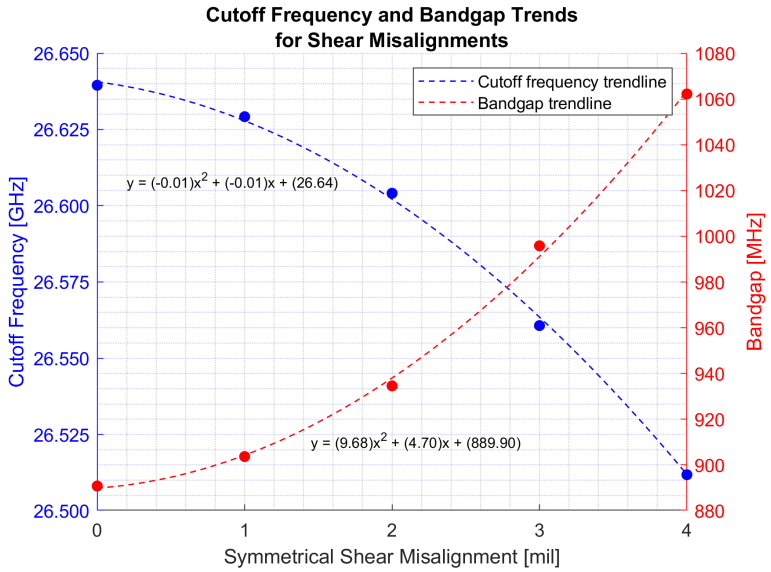

Figure 5.13: Cutoff frequency and bandgap variations for symmetrical shear misalignments with best-fit curves (dashed traces). The horizontal axis denotes each symmetrical misalignment, i.e., 0 represents $(x, z) = (0, 0)$ (the aligned case), 1 represents the $(x, z) = (1, 1)$ symmetrical misalignment, and so forth.

Eigenmode simulations for shear misalignments were also performed to investigate if there are any changes in the misaligned structure's frequency or bandgap size. The dispersion curves for the shear misalignments take a very similar shape as those in Fig. 5.8, however, the SWG's cutoff frequencies and bandgaps do change in the misaligned circuit. A concise summary of these changes is presented in Table 5.2.

It is evident that as the symmetrical misalignments grow more severe, the cutoff frequency decreases and the bandgap at π increases. These trends are depicted graphically in Fig. 5.13. The observed behavior shows the cutoff frequency decreases quadratically and the bandgap increases quadratically. Recall the changes in S_{11} magnitude for shear misalignments discussed previously also varied nonlinearly.

5.4.2 Rotational Misalignments

The second type of 2D misalignment studied is the rotational misalignment, which has been previously defined in Sec. 5.2. Clockwise rotational misalignments with magnitudes $\phi = 0.1°$, $\phi = 0.2°$, $\phi = 0.3°$, $\phi = 0.4°$, and $\phi = 0.5°$ are chosen to be simulated. These values are selected based on the fact that a $0.5°$ rotation corresponds to a 17.32 mil displacement in $\hat{x}$ at the end of the beam tunnel, which is less than the 24.00 mil beam tunnel radius. As with the $(5, 5)$ mil shear misalignment, the $0.5°$ rotational misalignment is an extreme case, but it is still beneficial to study the consequences such a displacement has on the RF signal for the same reasons discussed earlier in the text.

Contrary to the shear misalignments, there are no extrema at 32 GHz, nor anywhere else in the band for the rotational misalignments in both the circuit without tapers and the circuit with tapers. The magnitude of S_{11} in Fig. 5.14a and in Fig. 5.15a does increase with increasing rotational misalignment; however, this increase is relatively flat across the entire Ka-band for all rotational misalignment displacements. The S_{21} response for the rotational misalignments also differs from the shear misalignments. There are no concentrated minima near 32 GHz, but instead, a standing wave is present throughout the entire band as seen in Fig. 5.14b and in Fig. 5.15b. The standing wave's magnitude becomes more severe with increasing frequency. At 39.5 GHz, the $\phi = 0.5°$ standing wave oscillates between -0.5 dB and -0.7 dB.

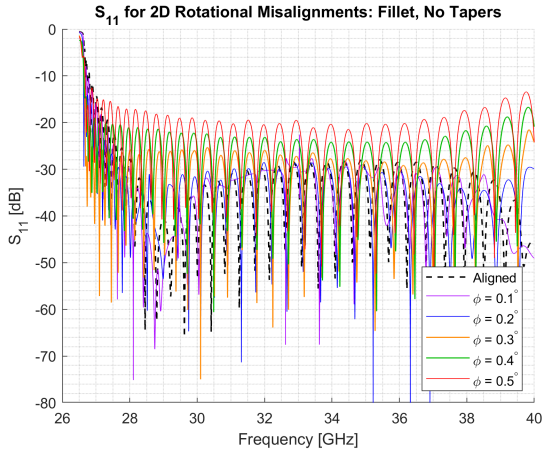

(a) SWG S_{11} response for various clockwise rotational misalignments in the x-z plane.

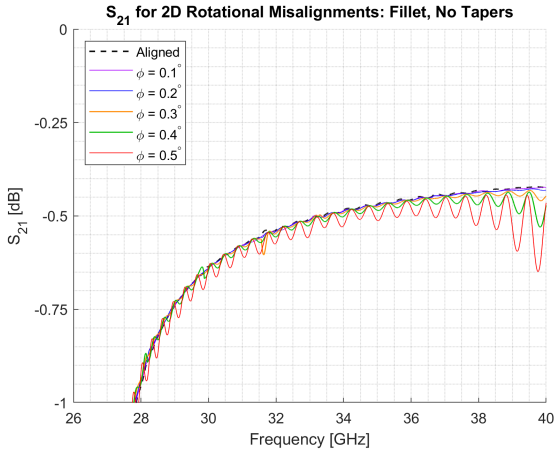

(b) SWG S_{21} response for various clockwise rotational misalignments in the x-z plane.

Figure 5.14: Reflection and transmission results for clockwise rotational misalignments ranging from $0.1°$ to $0.5°$ in the SWG structure with the matching fillet and without tapers. Note that a $0.5°$ rotational misalignment corresponds to a 17.32 mil = 0.4399 mm displacement at the end of the beam tunnel (the beam tunnel's radius is 24.00 mil = 0.6096 mm).

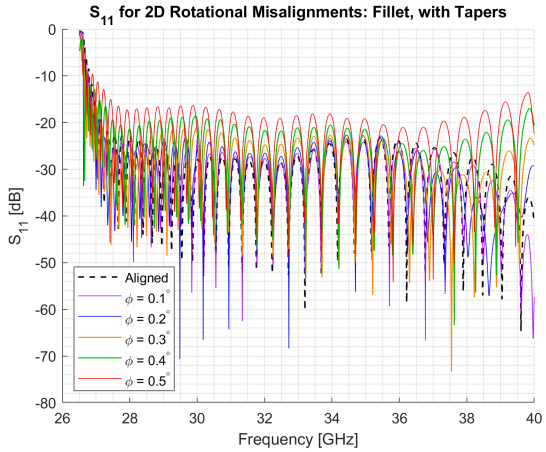

(a) SWG S_{11} response for various clockwise rotational misalignments in the x-z plane.

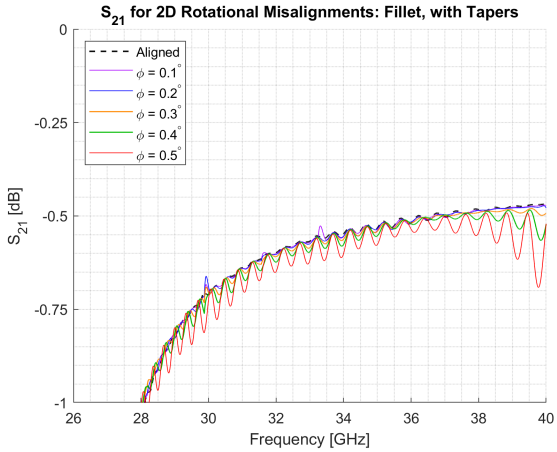

(b) SWG S_{21} response for various clockwise rotational misalignments in the x-z plane.

Figure 5.15: Reflection and transmission results for clockwise rotational misalignments ranging from $0.1°$ to $0.5°$ in the SWG structure with the matching fillet and tapers. Note that a $0.5°$ rotational misalignment corresponds to a 17.32 mil = 0.44 mm displacement at the end of the beam tunnel (the beam tunnel's radius is 24 mil = 0.6096 mm).

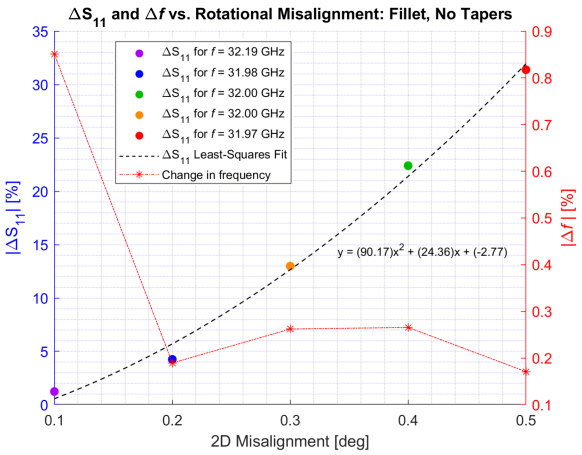

(a) Characteristic changes in the S_{11} local maximum (with least-squares fit) and the frequency at which it occurs for the SWG without tapers.

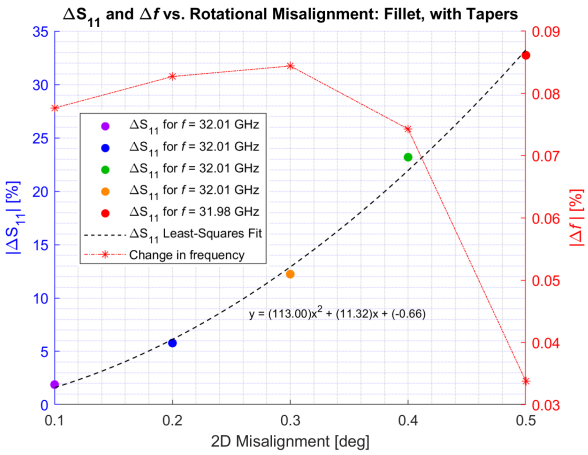

(b) Characteristic changes in the S_{11} local maximum (with least-squares fit) and the frequency at which it occurs for the SWG with tapers.

Figure 5.16: Characteristic changes in the reflected signal's local maximum near 32 GHz as well as how far each misalignment's local maximum center frequency deviates from the frequency at which the local maximum occurring closest to 32 GHz in the aligned structure resides for rotational misalignments ranging from $\hat{\phi} = 0.1°$ to $\hat{\phi} = 0.5°$. The horizontal axis is marked in terms of rotational misalignment, i.e., "0.1" on the horizontal axis corresponds to the $\hat{\phi} = 0.1°$ misalignment.

Though no extrema are present at 32 GHz, it is still beneficial to further inspect the change in S_{11} magnitude of the local maximum near 32 GHz and by how much the the maximum's center frequency deviates from the aligned circuit's local maximum near the same frequency. It is evident from Fig. 5.16a and Fig. 5.16b the increase in S_{11} magnitude is quadratic. Recall for the shear misalignments, the increase in S_{11} goes like a square root.

The change in frequency observed for rotational alignment in the SWG without tapers has a general decreasing trend whereas shear misalignments in the same structure has an increasing frequency shift magnitude. The SWG with tapers exhibits a decrease in frequency shift magnitude for both shear and rotational misalignments, however.

5.5 Chapter Summary

In this chapter, various 1D and 2D misalignments were simulated using HFSS and characterized using S-parameters, cutoff frequencies, and bandgaps as figures of merit. The 2D shear misalignments caused profound signal degradation isolated at 32 GHz whereas the 2D rotational misalignments affected the entire band. In both cases, the S-parameter responses were nonlinear.

Chapter 6: Ka-Band Circuit Cold Tests

6.1 Overview

Detailed simulations characterizing the S-parameters and dispersion curves in a misaligned Ka-band SWG structure have been presented. Computer simulations can only go so far, however. The precision alignment techniques discussed in Ch. 2 must now be put into practice to determine if any misalignments are present in the fabricated circuit. More importantly, the residual misalignment effects on the laboratory-measured RF signal must be determined.

6.2 Fabricated Circuit Block

The reasons behind the choice to manufacture the Ka-band circuit block have already been discussed in detail in previous sections. Here, the CAD model for the fabrication circuit is presented in Fig. 6.1. Two blocks compose the full circuit that is aligned using alignment pins and the elastic averaging technique. In this project's first phase, the EA and QKC precision alignment techniques were tested for alignment accuracy and repeatability. The EA technique was selected over QKC for the SWG structure because its alignment was accurate to within 1.4 μm and it also allows for multi-layer structures.

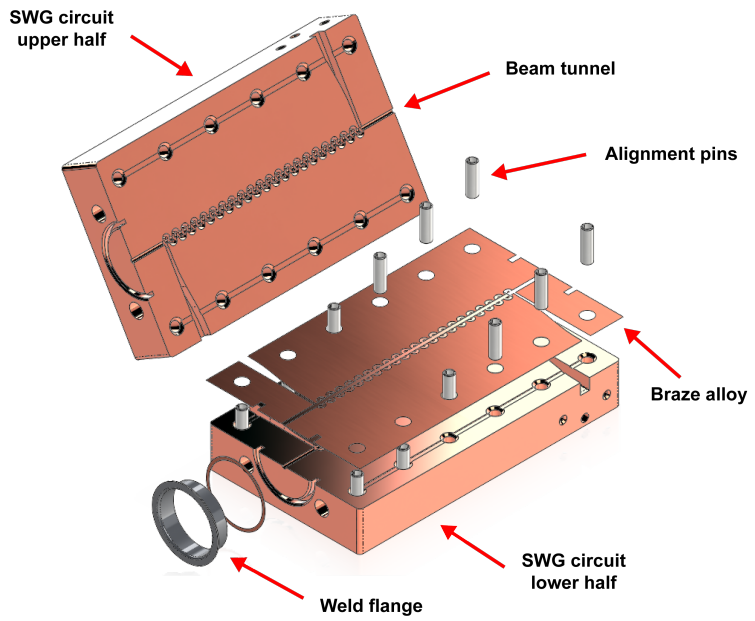

Figure 6.1: Exploded view of the fabricated Ka-band SWG circuit block. Adapted from [6].

Two circuit blocks were fabricated. The first to be made did not include the brazing alloy shown in Fig. 6.1. We will call this circuit the "unbrazed" circuit. Forgoing the brazing alloy in the first circuit manufactured was done in an attempt to better measure the EA precision as well as the device's S-parameters. The brazing process includes heating the circuit to temperatures at and above 500°C to melt the alloy. Thus, it is possible for the alloy to leak into the SWG itself thereby causing disturbances in the RF signal. It is for this reason the brazing alloy was not included in the first circuit manufactured.

The second fabricated circuit did include the brazing alloy between the two circuit block halves. We will call this circuit the "brazed" circuit. Brazing is necessary for TWT operation in order to ensure good conductivity between the two circuit halves as well as to preserve vacuum in the device. The SWG must be under vacuum to minimize collisions between the electron beam and other particles when the device is operating as a TWT amplifier. In this case, the electron gun

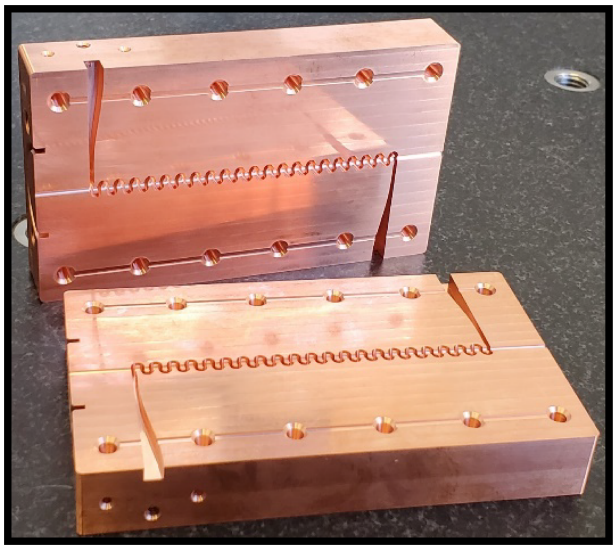

(a) Top and bottom halves of the fabricated Ka-band SWG circuit block before the halves are fastened together using the elastic averaging precision alignment technique.

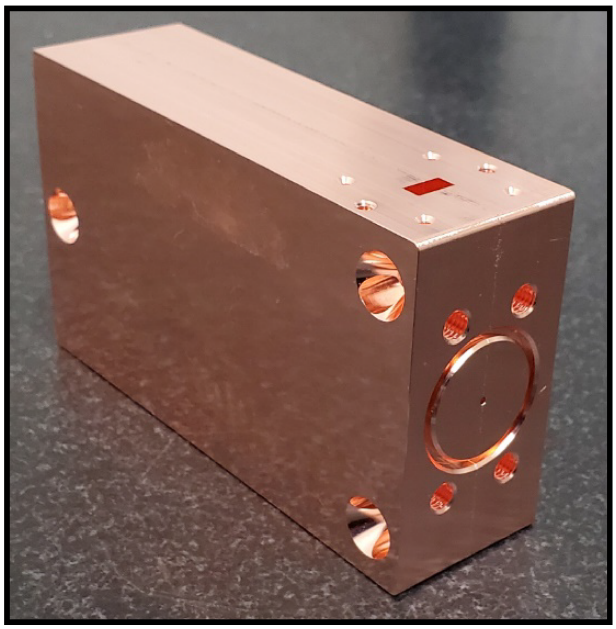

(b) Fully assembled Ka-band SWG circuit block.

Figure 6.2: Fabricated Ka-band SWG circuit block. The circuit is 3.9690 in. (100.8126 mm) long and 2.3000 in. (58.4200 mm) wide. Adapted from [6].

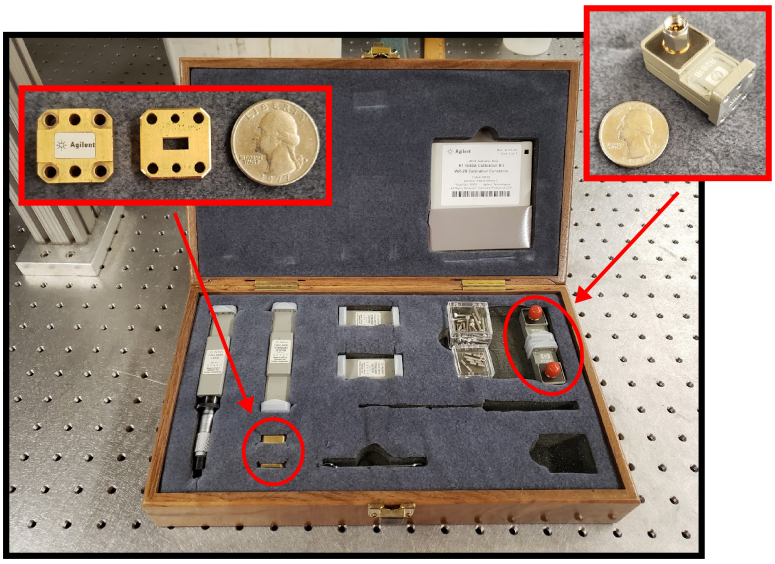

Figure 6.3: The Agilent R11644A waveguide calibration kit for a vector network analyzer. The top left inset depicts the waveguide short (left) and the $\lambda/4$ line (center). The top right inset depicts the R281B 2.4 mm coaxial line to WR-28 adapter. A quarter is included in both insets to provide a size reference.

is affixed to the weld flange shown in Fig. 6.1 and a collector would be attached to the opposite end of the circuit. Images of the fabricated circuit are illustrated in Fig. 6.2a and Fig. 6.2b.

6.3 Test Equipment Calibration

The S-parameter cold test measurements for both the unbrazed and brazed circuit were performed at IREAP using the Agilent Technologies E8361C performance network analyzer (PNA)[4] with a 10 MHz – 67 GHz bandwidth. When the W-band circuit is manufactured, the VNA can be upgraded to include W-band frequencies and above using VNA frequency extenders such as those made by Virginia Diodes, Inc.

VNA calibration prior to the cold tests was performed using the Agilent R11644A WR-28 waveguide calibration kit. The kit's bandwidth is that of Ka-band (26.5 GHz – 40 GHz) and

[4]Please note the PNA name designation is simply a proprietary product line of Agilent vector network analyzers (VNA). This device will be referred to as a VNA herein.

its contents are shown in Fig. 6.3. The R281B 2.4 mm coaxial line to waveguide adapter (depicted in the top right inset in Fig. 6.3) must be included in the calibration because the VNA ports are coaxial. The calibration for the VNA was performed using the thru, reflect, and line (TRL) standards which are often more accurate than its short, open, load, and thru (SOLT) standards counterpart (this is mainly because TRL standards have more simple definitions and the hardware is easier to fabricate as opposed to SOLT standards, which often times include a sliding waveguide load) [32].

6.4 Unbrazed Circuit

Cold test measurements for the unbrazed circuit were performed first. The following section details the measurement results. Additional information regarding the misalignment quality control measurements for the fabricated, unbrazed circuit can be found in [6] and [33]. A summary of the findings is outlined in Table 6.1. The fabricated, unbrazed circuit discussed in these references is the exact circuit cold tested in the following sections.

6.4.1 WR-28 Flange Adapters

Waveguide flanges (the method used to fasten waveguides together) typically come in one of two variants: a square flange or a circular flange. For frequencies below Ka-band, square flanges are more commonly used; for frequencies at and above Ka-band, however, circular flanges are typically standard. It is for this reason the unbrazed Ka-band circuit block was fabricated with waveguide alignment pin and screw holes for a circular flange. The circular flange design was not known by the UMD team until the already fabricated, unbrazed circuit arrived at IREAP. The

R281B coaxial line to waveguide adapters necessary for VNA calibration and the cold tests have square flanges, however. This incompatible waveguide flange problem was solved by adding a 1 in. WR-28 standard section with a square flange on one end and a circular flange on the opposite end between the R281B and the SWG circuit block. We will call these standard sections "flange adapters;" they are visible in the bottom left inset in Fig. 6.4a.

The flange adapter addition presents a challenge for the cold tests. Because one end of the adapters has a circular flange, the TRL component standards for the VNA calibration are not able to fasten to the adapters. Consequently, the flange adapters are outside the calibration plane, which is undesirable. In other words, any reflections, loss, or dispersion that occurs in the flange adapters (which is generally low for short, straight waveguide sections) will be characterized as a part of the SWG circuit's response thus reducing the SWG circuit S-parameter characterization accuracy. The given contract time restraints prohibited the group from addressing this problem in the unbrazed Ka-band circuit, however, it was resolved in the brazed circuit. Further discussion about this resolution will be presented in Sec. 6.5. For now, all unbrazed circuit cold tests include the 1 in. WR-28 standard section flange adapters.

6.4.2 Unbrazed Circuit Cold Tests

Three cold tests for the unbrazed circuit block were performed. The first test's setup included testing the unbrazed, "unclamped" circuit block. This setup is depicted in Fig. 6.4a.

Clamps were added in the subsequent cold tests to determine if added pressure on the blocks could make up for the lack of brazing material. The first cold test performed with the clamps included one clamp positioned in the circuit block's center (see Fig. 6.4b) and the

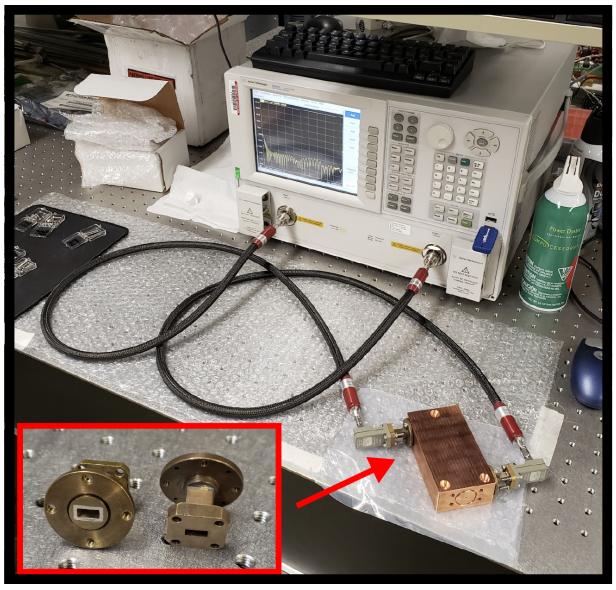

(a) Unbrazed, unclamped circuit cold test. The WR-28 flange adapters are shown in the inset at the bottom left of the image.

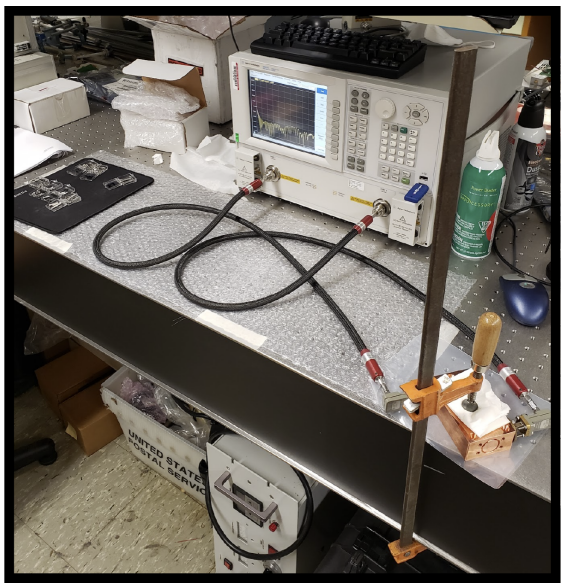

(b) Unbrazed circuit with a single clamp positioned at the circuit block's center.

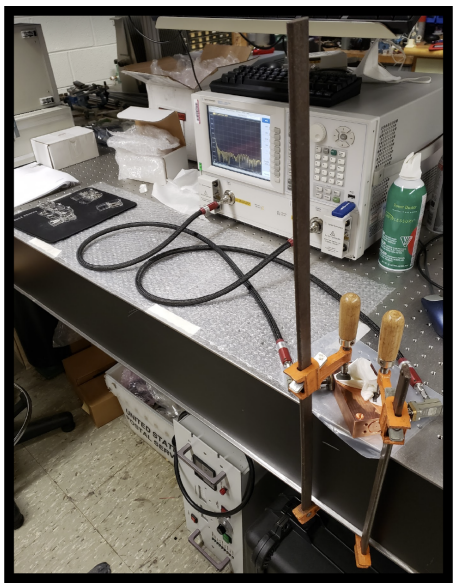

(c) Unbrazed circuit with a two clamps. Each clamp is positioned adjacent to the WR-28 ports on either side of the circuit block.

Figure 6.4: Laboratory setup for the unbrazed Ka-band circuit block cold tests performed at IREAP.

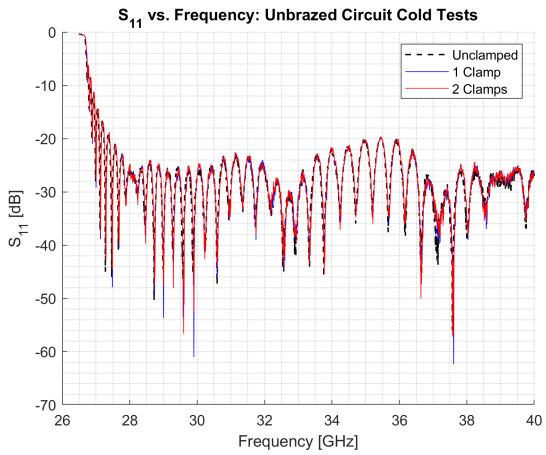

(a) S_{11} response for the three unbrazed circuit cold tests.

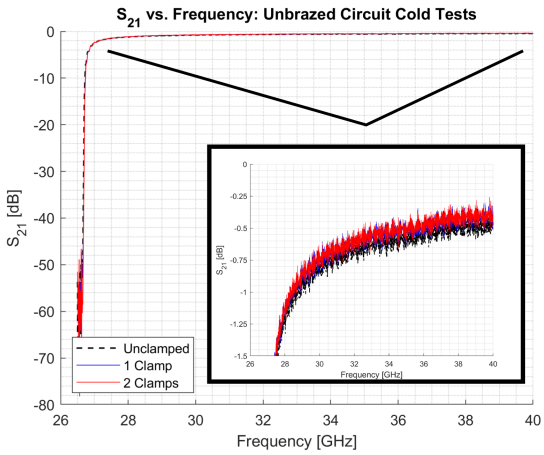

(b) S_{21} response for the three unbrazed circuit cold tests.

Figure 6.5: Unbrazed Ka-band circuit cold test results. The three tests performed included the unclamped circuit block measurement, a measurement where a single clamp was positioned in the circuit block's center, and a measurement where two clamps were each positioned adjacent to the WR-28 ports on either side of the circuit block.

second, clamped cold test included two clamps, each of which were positioned adjacent to the two waveguide ports (see Fig. 6.4c). In the cold tests consisting of the clamped structure, we were looking to identify any reduction in reflected power or increase in transmitted power compared to the unclamped device. The unbrazed circuit's cold test measurements are presented in Fig. 6.5.

The resulting cold test S-parameters for the unbrazed circuit shown in Fig. 6.5 are quite remarkable. It is evident in Fig. 6.5a the reflected power in the unclamped, single-clamped, and double-clamped structures is nearly identical. Only small deviations less than 2 dB in magnitude are visible between 38.5 GHz and 39.5 GHz in the S_{11} response. At levels below 20 dB down, these deviations are negligible. The reflected power's standing wave periodicity is also identical. For the transmitted power in Fig. 6.5b, no discrepancies between the three structures is visible above cutoff.

The cold test laboratory measurements also agree quite well with the SWG circuit simulated in HFSS presented in previous chapters. In fact, if we compare the reflected power response in

Fig. 6.5a with the simulated SWG with tapers (the solid red trace) in Fig. 5.3, we can also see very good agreement. Above cutoff, the maximum reflected power in the simulated circuit is about -23 dB at 35 GHz whereas in the three cold-tested circuits, the maximum reflected power occurs at the same frequency and is measured to be approximately -20 dB. The the fabricated structure exceeds the -25 dB maximum reflected power threshold design goal imposed earlier in the design process, but not by more than 5 dB. Though not optimal, we are satisfied with these results given these levels were achieved with an unbrazed circuit that included additional straight waveguide sections.

It is also possible to come to the conclusion there are very few misalignments in the structure based on the fact no outliers in magnitude occur in S_{11} or S_{21}. based on the simulated data presented in Ch. 5, we can deduce that if any misalignments are present, they should be less than 1 mil. Such a conclusion, solely based on the S-parameter laboratory measurements, is confirmed by the middle column in Table 6.1 where the largest misalignment arises in $\hat{x}$ with magnitude 0.558 mil (14.173 μm).

Results as consistent as those presented in Fig. 6.5 across unclamped and clamped VEDs manufactured in the split-block configuration has not been observed before in the vacuum electronics field. We can attribute these measurements to accurate VNA calibration, but more importantly, to successful fabrication implementation of the EA precision alignment technique in the Ka-band circuit block. Observing these measurements in the unbrazed circuit with the flange adapter addition is promising as it is likely better results will be obtained when the flange adapters can be removed and the circuit is brazed. The S-parameter's consistency across the three unbrazed structures warrants the use of the unbrazed, unclamped circuit as the unbrazed circuit baseline throughout the following sections.

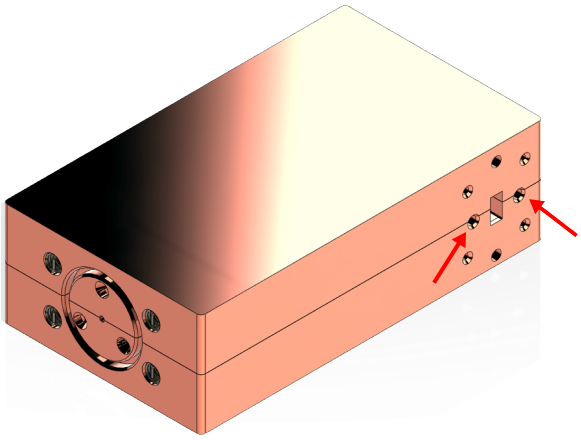

Figure 6.6: Alignment pin holes for the square WR-28 flange added to the Ka-band circuit block. The red arrows point to the new holes.

6.5 Brazed Circuit

The next cold tests performed involved the brazed circuit that was manufactured. Like the unbrazed structure, more details about the brazed circuit can be found in [6] and a summary of the measured misalignments are outlined in Table 6.1. The fabricated, brazed circuit discussed in this reference is the exact circuit cold tested in the following sections.

6.5.1 Circuit Modifications

Fabrication of the brazed structure finished shortly after the unbrazed circuit, so it was possible to add square flange alignment pin holes to the brazed circuit block, thus allowing us to remove the 1 in. standard section flange adapters. The new alignment pin holes are denoted by the red arrows in Fig. 6.6. Screw holes for the square flange could not be added to the brazed circuit block because the circular flange holes had already been milled. If square flange screw holes were added to the brazed structure, they would overlap the circular flange holes prohibiting screws for either flange type from maintaining a tight bond between the waveguide and the circuit block.

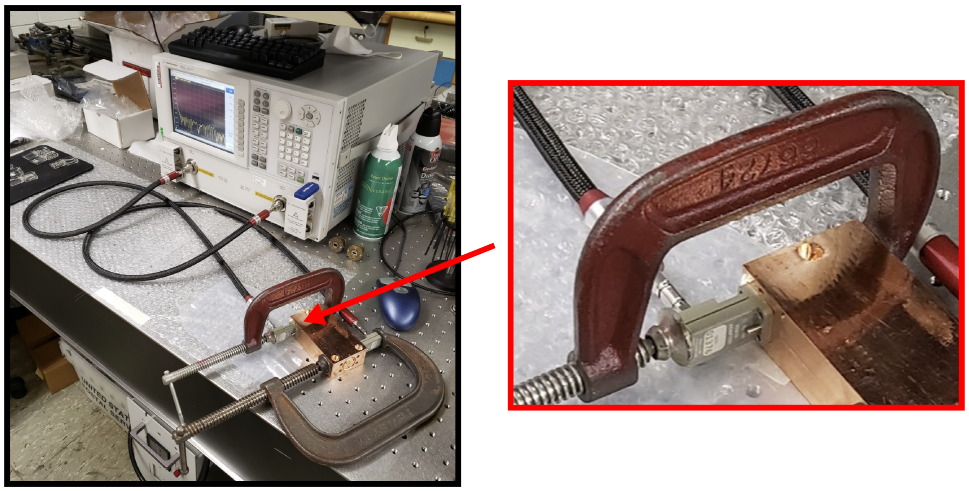

Figure 6.7: Laboratory setup for the brazed Ka-band circuit cold tests. One of the two silver WR-28 alignment pins is visible just underneath the R281B adapter. The second alignment pin is located on the opposite side.

Any gaps between the waveguide flange and the block may increase reflections and/or reduce transmission.

It is still possible to tightly fasten the R281 coaxial line to WR-28 adapter to the circuit block by using the square flange alignment pins as well as clamps directed perpendicularly to the circuit (see the inset in Fig. 6.7). The horizontal clamps' purpose is not the clamp the circuit block like described in Sec. 6.4.2, but instead, to solely fasten the R281B adapter to the structure. Removing the flange adapters will not only allow for a more accurate RF characterization of the brazed circuit, but it should also slightly reduce reflection and slightly increase transmission.

6.5.2 Brazed Circuit Cold Tests

Before the brazed circuit is tested without the flange adapters, it is beneficial to perform a brazed circuit cold test with the flange adapters to compare its results to the unbrazed circuit (that requires the flange adapters). Results for this test are plotted in Fig. 6.8.

As expected, the brazed circuit exhibits a lower reflection magnitude than the unbrazed circuit throughout most of the band. There are only a few brazed circuit local maxima between 28 GHz and 31 GHz that exceed the unbrazed circuit's S_{11}. This is an encouraging result given the flange adapters are still included in the measurement.

Next, the flange adapters are removed from the brazed circuit the S-parameters are remeasured. These results are plotted in Fig. 6.9 and further examination reveals removing the flange adapter from the brazed circuit reduces S_{11} and increases S_{21} thereby agreeing with the original hypothesis.

An astute observation can be made for the reflected power in Fig. 6.9a. Just below 33 GHz, S_{11} improves significantly (i.e., the curve decreases in magnitude) compared to the rest of the band. More specifically, at $\approx$32.75 GHz, the local maxima for the brazed circuit with flange adapters (the blue trace) is -32 dB and the local maxima for the brazed circuit without flange adapters (the red trace) at the same frequency drops below -50 dB. Recall that in the HFSS simulations, the $^{3\pi}/_{2}$ point occurs at 32 GHz, which makes this decrease in reflection particularly intriguing.

The simulations also indicate the $^{3\pi}/_{2}$ point is where disturbances in reflection and transmission are present if the circuit is misaligned. We saw that especially for 2D shear misalignments, S_{11} increases and S_{21} decreases in a nonlinear manner as the misalignments grow more severe. The only misalignment case simulated where S_{11} improved is in the 1D, $(x, z) = (0, 5)$ misalignment (see Fig. 5.4a). It is difficult to make an accurate comparison with this simulation, however, because the structure in Fig. 5.4a was simulated without the tapers to the WR-28. The fabricated circuit, of course, includes the tapers.

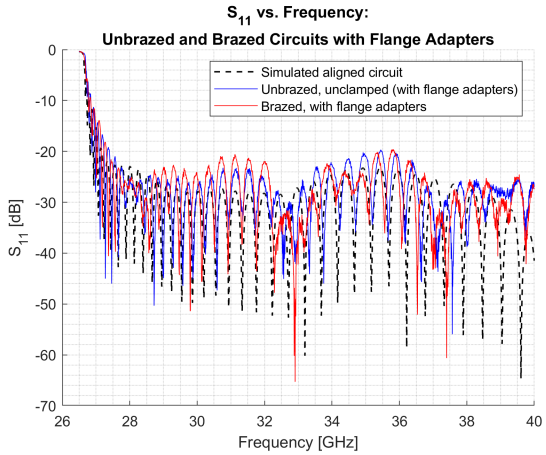

(a) S_{11} response for the unbrazed and brazed circuits with the flange adapters.

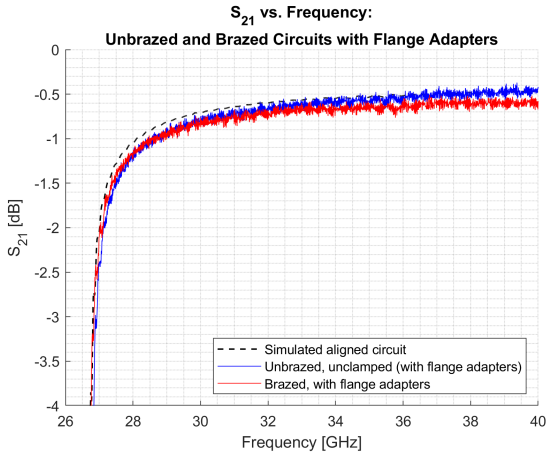

(b) S_{21} response for the unbrazed and brazed circuits with the flange adapters.

Figure 6.8: Reflection and transmission cold test results for the unbrazed and brazed circuits with the WR-28 flange adapters.

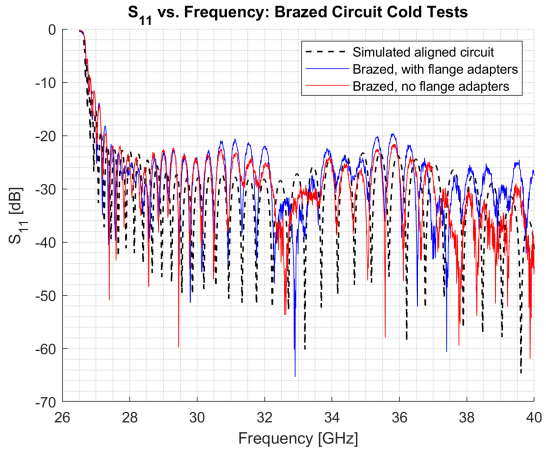

(a) S_{11} response for the brazed circuit with and without the flange adapters.

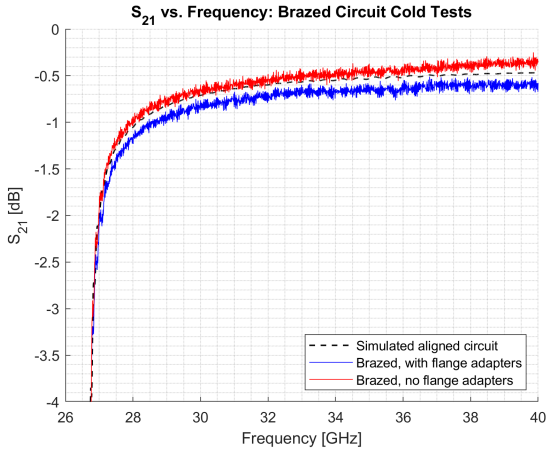

(b) S_{21} response for the brazed circuit with and without the flange adapters.

Figure 6.9: Reflection and transmission cold test results for brazed circuit with and without the WR-28 flange adapters.

It should also be noted the simulated improvement is present in the large, 1D, 5 mil misalignment in $\hat{z}$. Further inspection into Table 6.1 reveals the largest misalignment in the brazed (and unbrazed) fabricated circuit does occur in the $\hat{z}$-direction. Though the 5 mil misalignment magnitude is much greater in the simulations than the 0.558 mil misalignment in the fabricated circuit, it is of special interest the largest displacement in both cases is in $\hat{z}$. For this reason, the decrease in S_{11} may not necessarily be related to the one-dimensional misalignment magnitude, but instead, when the displacement in one dimension, particularly along $\hat{z}$, far exceeds the displacement in the adjacent dimension. This is the case for both the fabricated unbrazed and brazed circuits where the misalignments in $\hat{z}$ are greater than those in $\hat{x}$ (see the numbers outlined in bold in Table 6.1). Additional simulations and laboratory tests are required to confirm this result, however.

6.6 Chapter Summary

Many laboratory measurements for the Ka-band SWG circuit have been outlined throughout this chapter. A concise summary of the measurements is plotted in Fig. 6.10 and a summary of the misalignment magnitudes in the fabricated circuits is given in Table 6.1.

There is much room for improvement in the circuit block fabrication and cold test measurement technique before the W-band circuit is designed. More focus will be put on improving the piece-part (i.e., each individual part) manufacturing precision of the SWG circuit block so that the final assembly has misalignments with smaller magnitudes, if any are present at all. It is especially important at W-band frequencies to ensure precise fabrication because the RF signal's wavelength is much smaller than those in Ka-band. Waveguides with circular flanges will

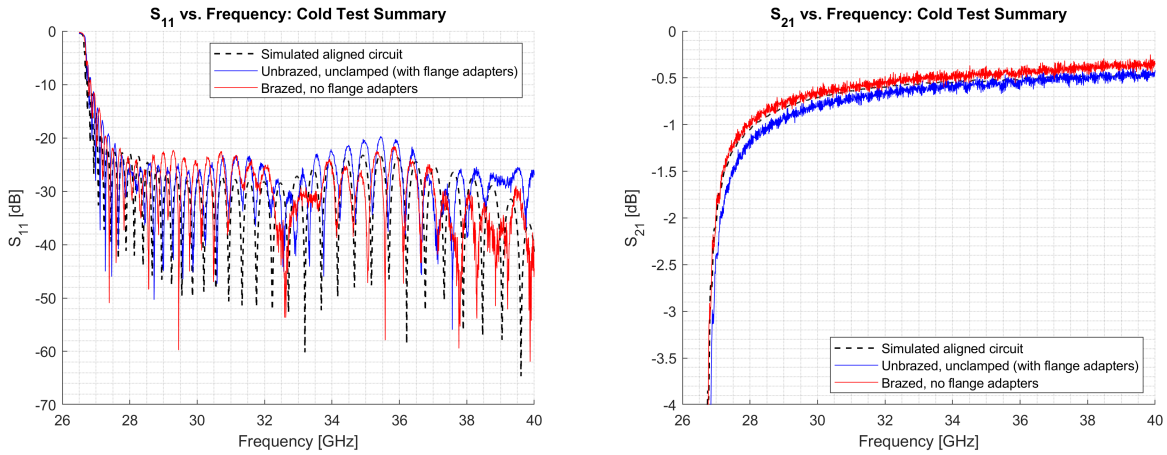

(a) S_{11} cold test summary.

(b) S_{21} cold test summary.

Figure 6.10: Summary of the S-parameters from the cold tests performed for the unbrazed SWG circuit with the flange adapters and the brazed SWG circuit without the flange adapters. The cold test data is compared to the simulated, aligned structure (with tapers) baseline.

also be procured to match the planned alignment pin and screw hole circular flange configuration on the W-band circuit block.

A detailed study into the effect misalignments have on a Ka-band SWG circuit through simulations and laboratory testing has been presented. Efforts will now shift to translating the lessons learned throughout the Ka-band SWG circuit design into creating a SWG to be used in a fully-functional W-band TWT prototype.

Measured Misalignments in the Fabricated Ka-Band Circuits

Feature	Unbrazed Circuit (mil [μm])	Brazed Circuit (mil [μm])
Front	0.279 [7.087]	0.04 [1.02]
Left	0.138 [3.505]	0.20 [5.08]
Right	0.145 [3.683]	0.14 [3.56]
Back	0.456 [11.582]	0.21 [5.33]
Beam Tunnel		
$\hat{x}$-Front	0.162 [4.115]	0.17 [4.32]
$\hat{z}$-Front	0.195 [4.953]	**0.64 [16.26]**
$\hat{x}$-Back	0.136 [3.454]	0.06 [1.52]
$\hat{z}$-Back	**0.558 [14.173]**	0.41 [10.41]

Table 6.1: Measured misalignments in the unbrazed and brazed fabricated Ka-band circuit blocks. The "front," "left," "right," and "back" terms are all relative to the circuit block shown in Fig. 6.1. The front face is the where the weld flange is located and the right face is where the "SWG circuit lower half" label is located. The bold table entries signify the largest misalignment in each structure. Adapted from [6, 33].

Chapter 7: W-Band Circuit Optimization

7.1 Overview

The contract supporting this work requires a precision-fabricated W-band SWG TWT prototype. Using lessons learned from the Ka-band circuit, the W-band SWG SWS design can begin smoothly. The first portion of this chapter details the preliminary circuit's design origins and verification. The latter parts of the chapter will then describe alterations made to the circuit in an effort to optimize its performance, which is measured in terms of the SWG's S-parameters, but more importantly, its cutoff frequency and beam-wave interaction.

7.2 Preliminary Design

7.2.1 Circuit Repeatability Verification

The initial W-band circuit design begins through a verification process. A W-band design with similar performance goals we strive to achieve is presented in [34]. Few dimensions and circuit parameters are given in the paper, however. Our group adapted the dimensions available and using the pictures provided in the paper, we attempted to reverse engineer a single circuit period. Verification of our "scaled" design was done by performing an HFSS eigenmode

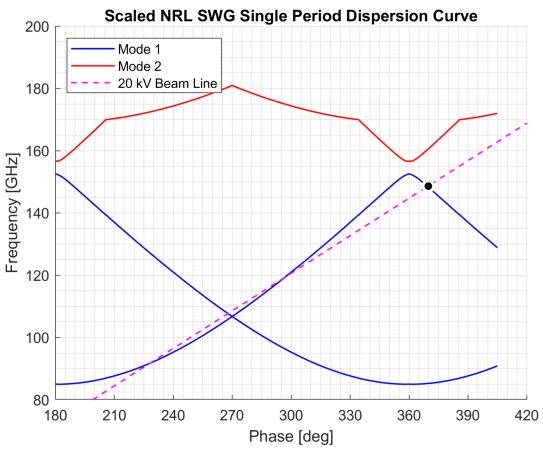

(a) Dispersion curves for the "scaled" SWG.

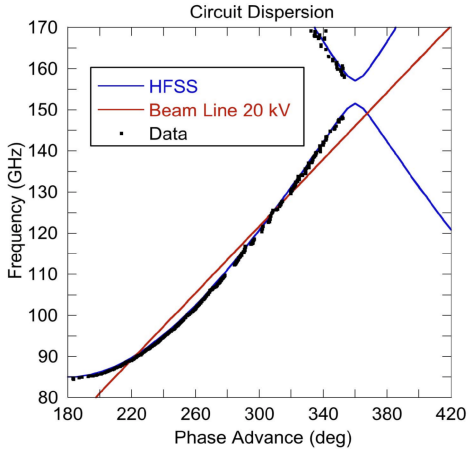

(b) Dispersion curves for the NRL SWG. Adapted from [34].

Figure 7.1: Comparison of the "scaled" W-band circuit's dispersion curves to the dispersion curves for the original NRL W-band circuit presented in [34].

simulation and comparing our simulated dispersion curves to those presented in the paper. The results are shown in Fig. 7.1.

The scaled model's validity is confirmed by comparing its dispersion curves in Fig. 7.1a to the dispersion curves in Fig. 7.1b. In both plots, the 20 kV beam line[5] crosses the TE_{10} mode at three points between 180° and 420°. The black dot in Fig. 7.1a occurs at a the phase advance of ≈370°, which corresponds to a frequency of ≈150 GHz. This point is consistent with the beam line crossing above 360° in Fig. 7.1b. We may thus conclude the scaled model has been reverse-engineered accurately.

7.2.2 Full-Circuit Modeling

Following the single period verification, a W-band full-circuit model was designed. Tapers are again included to transition from the SWG size to the WR-10 standard waveguide size for

[5] A 20 kV beam has been chosen for the W-band SWG TWT design based on other STTR design requirements not detailed in this text.

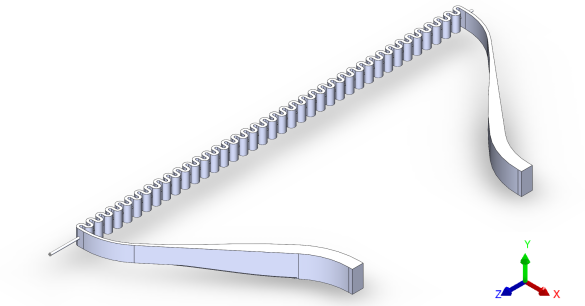

(a) CAD model for the scaled circuit's full structure including tapers to the standard WR-10.

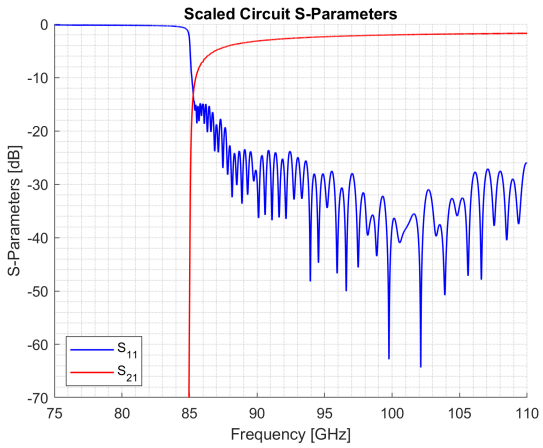

(b) S_{11} and S_{21} responses for the SWG scaled NRL W-band SWG circuit.

Figure 7.2: W-band full-circuit CAD model and its simulated S-parameter response. The circuit has $N = 40$ periods.

W-band (see Fig. 7.2a). Fillets were not added to this circuit because no significant improvement in S_{11} or S_{21} was observed in any simulations. The simulated S-parameter responses for this model are given in Fig. 7.2b.

The S-parameters for the full-circuit model indicate cutoff occurs at approximately 85 GHz. This is confirmed by the dispersion curves presented in Fig. 7.1a. Above 88 GHz, S_{11} reaches levels well below -20 dB, which is an encouraging result.[6] Notice, however, S_{21} saturates at about -2 dB and does not reach this level until $\approx$98 GHz, or 10 GHz above cutoff. Such a result reveals just over half the incident power is transmitted through the device. In the simulated, aligned Ka-band circuit, the S_{21} response was much higher. The transmitted power crossed the -2 dB threshold at approximately 27 GHz, or only 500 MHz above Ka-band's lower band edge. S_{21} proceeded to stay between 0 dB and 2 dB down for the remainder of Ka-band. In fact, above 30 GHz, S_{21} remained at levels between -0.70 dB and -0.45 dB for the Ka-band circuit.

[6]The S-parameter results plotted in Fig. 7.2b are consistent with those presented in [34]. In fact, the scaled circuit's simulated S_{11} response outperforms the HFSS simulation results presented in [34].

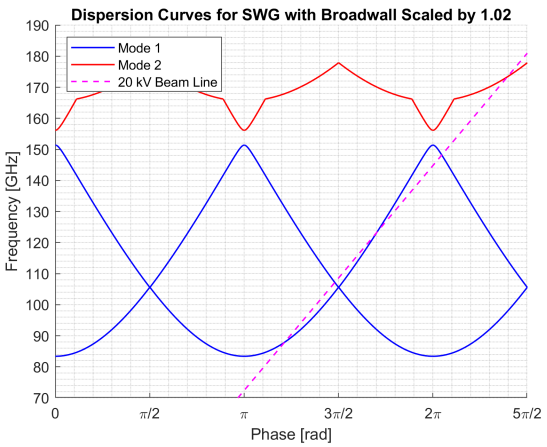

(a) Dispersion curves for the circuit with a 2% larger broadwall dimension, W.

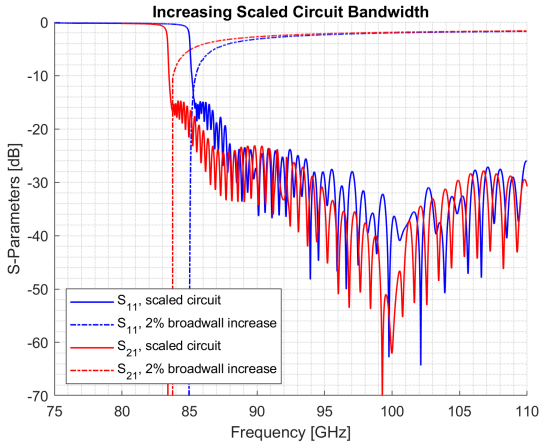

(b) Reflected and transmitted power in the circuit with the 2% broadwall increase compared to the scaled circuit.

Figure 7.3: Dispersion curves and S-parameter results for the scaled W-band circuit with a 2% increase in the broadwall size.

7.3 Increasing Bandwidth

The bandwidth for the scaled device is ≈25 GHz, which is significant in general terms, but it is desirable to attempt to widen it in order to increase the device's functionality. Increasing the device's bandwidth amounts to decreasing the scaled circuit's cutoff frequency. To do this, recall the expression for a rectangular waveguide's cutoff frequency given in (2.7). The TE_{10} mode is the mode of most interest for the beam-wave interaction, so the the second term in (2.7) can be ignored. It was decided to increase the scaled circuit's bandwidth by 2% thus demanding the broadwall dimension, a, to be increased by 2%.[7] The dispersion curves and the S-parameter responses are given in Fig. 7.3a and Fig. 7.3b, respectively. It can be deduced from both Fig. 7.3a and Fig. 7.3b the cutoff frequency decreases from ≈85 GHz in the scaled circuit's case to 83.39 GHz in the circuit with the 2% increase in broadwall size.

[7]The broadwall dimension variable name in the SWG single period model is defined as W (recall Fig. 4.2).

Though the bandwidth expansion goal has been successfully achieved, there is still a design flaw in this circuit that will need to be addressed before fabrication. This issue is discussed in the next section.

7.4 Avoiding Instabilities

A glaring problem is present in Fig. 7.1a and Fig. 7.3a; the beam line intersects a backward wave just beyond 2π. In general terms, such behavior in a TWT is undesirable because backward-wave instabilities are likely to arise.[8] To avoid said instabilities, we derive an analytical approach for the circuit design and test its efficacy using HFSS.

7.4.1 Analytical Approach

We begin the analytical approach with a simplified dispersion relation for the TE_{10} mode that can be derived from [24]:

$$\alpha = \pi + \frac{L_s}{c}\sqrt{\omega^2 - \omega_c^2}\,. \tag{7.1}$$

where $\alpha = kL_g$ is the phase advance across a single SWG period, $L_g = P$ is the gap length, and $L_s = x_i + x_o + \frac{\pi}{2}(r_i + r_o)$ is the average microwave signal path length through the SWG bend. These quantities are illustrated in Fig. 7.4.

It is then possible to write a normalized equation for frequency in terms of the phase advance, α, as

[8] In select applications, a backward-wave oscillator, or BWO (pronounced "bee-woah", also known as a "carcinotron"), requires a beam-wave interaction with a backward-wave. This phenomenon can be used to create a terahertz RF source (see [35, 36, 37] for more details about BWOs).

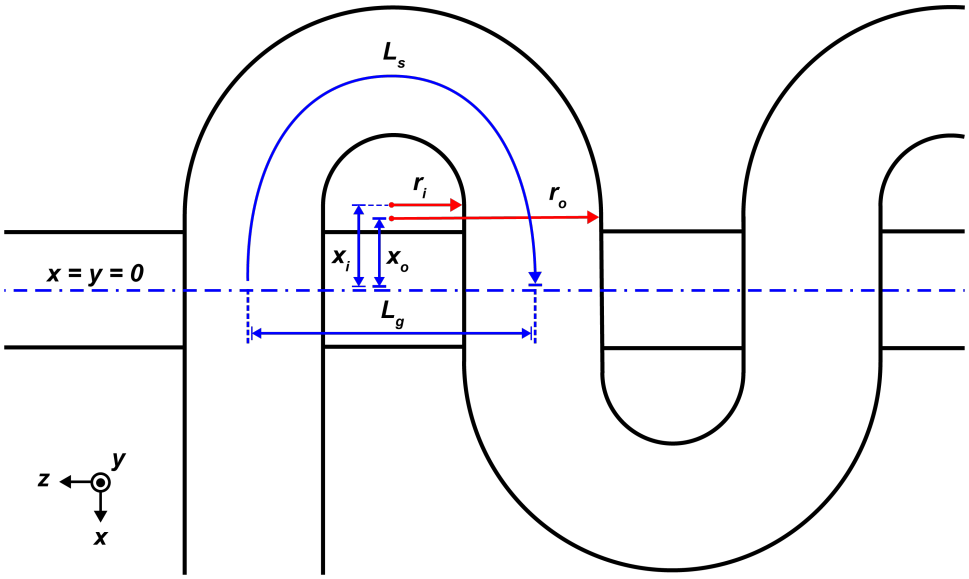

Figure 7.4: Additional SWG geometry variable definitions used in the analytical derivations.

$$\frac{\omega}{\omega_c} = \sqrt{1 + \left(\frac{\alpha - \pi}{\pi F_c}\right)^2} \tag{7.2}$$

where $F_c \equiv \frac{\omega_c L_s}{\pi c}$ is the dimensionless cutoff frequency. The beam's dispersion relation in terms of the beam's velocity, v_b, can expressed as

$$\omega = k v_b = \frac{\alpha}{L_g} v_b = \frac{\alpha}{\pi}\left(\frac{\pi v_b}{L_g}\right) . \tag{7.3}$$

Normalizing the beam's frequency to the SWG cutoff frequency then results in

$$\frac{\omega}{\omega_c} = \frac{\alpha}{\pi}\left(\frac{B}{F_c}\right) \tag{7.4}$$

where $B \equiv \frac{v_b L_s}{c L_g}$ is the dimensionless beam velocity.

We now demand the 20 kV beam line intersects the TE_{10} dispersion curve at 2π to avoid exciting any backward wave modes. Substituting in $\alpha = 2\pi$ into (7.2) and (7.4) and then equating the two yields

$$4B^2 = F_c^2 + 1 \,, \tag{7.5}$$

i.e.,

$$\boxed{F_c = \sqrt{4B^2 - 1}} \tag{7.6}$$

indicating that $B^2 > 1/4$. The beam line will also intersect the TE_{10} dispersion curve at a point before 2π, which can be found be equating (7.2) to (7.4) and then implicitly solving for $\theta \equiv \frac{\alpha}{\pi}$ thus yielding

$$\theta^2 B^2 = F_c^2 + (\theta - 1)^2 \ . \tag{7.7}$$

It is then necessary to substitute (7.5) into (7.7) and solve for θ to find the two solutions, i.e., the two points at which the beam line intersects the TE_{10} mode. The two solutions are given in (7.8) and (7.9).

$$\begin{cases} \theta_1 = \dfrac{2B^2}{1 - B^2} & (7.8) \\ \theta_2 = 2 & (7.9) \end{cases}$$

We can ignore the $\theta_2 = 2$ solution because it is equivalent to the $\alpha = 2\pi$ solution that has already been solved.

The additional constraint $\pi < \alpha < 2\pi$ (i.e., $1 < \theta < 2$) for the lower intersection must also be imposed to ensure any backward-wave crossings are avoided. Using (7.5) and (7.8), we arrive at the constraints for F_c and B:

$$\begin{cases} \dfrac{1}{3} < F_c^2 < 1 & (7.10) \\ \dfrac{1}{3} < B^2 < \dfrac{1}{2}\,, & (7.11) \end{cases}$$

which confirms the previous constraint that $B^2 > {}^1\!/_4$.

Now suppose we take $\omega = \omega_L$ where ω_L is the lower frequency at which the first beam line and TE_{10} dispersion curve crossing occurs. Thus, it is possible to define a "safety factor,"

$$R \equiv \frac{\omega_L}{\omega_c}\,, \tag{7.12}$$

describing the ratio of the lower intersection frequency to the SWG's cutoff frequency. Substituting $\omega = \omega_L$ into (7.2) and again equating (7.2) to (7.4) reveals

$$R = \frac{\alpha}{\pi}\left(\frac{B}{F_c}\right) = \theta\left(\frac{B}{F_c}\right)\,. \tag{7.13}$$

Finally, we substitute $\theta = \theta_1$ into (7.13) to arrive at the final expression for the safety factor as a function of the dimensionless quantity B:

$$\boxed{R = \frac{B}{\sqrt{4B^2 - 1}}\left(\frac{2B^2}{1 - B^2}\right).} \tag{7.14}$$

The curves for $F_c\,(B)$ and $R\,(B)$ are given in Fig. 7.5.

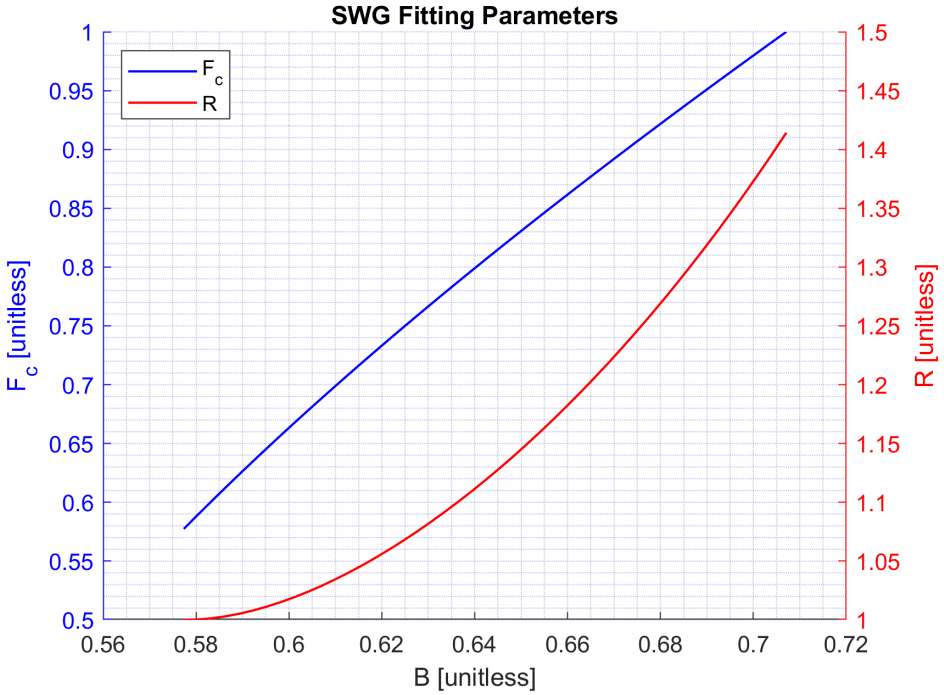

Figure 7.5: Curves representing the analytical relationships F_c and R, both as a function of B.

Optimized Geometry Parameters

Pre-Optimization	Post-Optimization
$P = L_g$	$P' = L'_g$
W	W'
G	G
S	S
L	L'
D	D
x_i	x'_i
x_o	x'_o
r_i	r'_i
r_o	r'_o

Table 7.1: SWG circuit parameters for the pre- and post-optimized W-band circuit. The optimization's goal is avoid any backward-wave mode excitations. The primed dimensions indicate new values not equivalent to the original, unprimed dimensions.

The analytical model presented in the previous section is a powerful tool that can be used to optimize the W-band circuit geometry in order to avoid any unwanted crossings simply by specifying a value for R and the circuit's operating frequency, f_0. Using these two figures of merit in the safety factor derivation results in a straightforward method to back-out SWG geometry quantities that will force the structure to adhere to the beam-wave intersection with the TE_{10} mode at 2π. More specifically, specifying R and f_0 in addition to already knowing the scaled structure's original dimensions (i.e., $P = L_g$, W, G, S, L, and D) will yield the optimized circuit dimensions L', or the SWG's new height, L'_s, or the new RF signal average path length through the SWG bend, L'_g, or the circuit's new gap length, W', or the new broadwall dimension, and consequently, f'_c, or the circuit's new cutoff frequency. It is also possible to further deduce x'_i, x'_o, r'_i, and r'_o from L'_g, G, and S. Table 7.1 illustrates the circuit dimension variables before it is optimized compared to the optimized geometry's parameters.

7.4.2 Selecting an Appropriate Safety Factor

The next step in optimizing the circuit's geometry to avoid backward-wave instabilities is to select an appropriate safety factor. The scaled circuit's safety factor is found to be $R_s = 1.07$, which can be found from Fig. 7.1a by inspection. It is evident we must choose a value for R such that $R > R_s$ to avoid any backward-wave intersections. Let us take $R_1 = 1.1$ and $R_1 = 1.2$ as initial guesses for R, choose $f_0 = 95$ GHz (a common operating frequency for W-band devices), perform the optimization, and analyze the results. The dispersion curves for the $R_1 = 1.1$ and $R_1 = 1.2$ optimizations are presented in Fig. 7.6a and Fig. 7.6b, respectively.

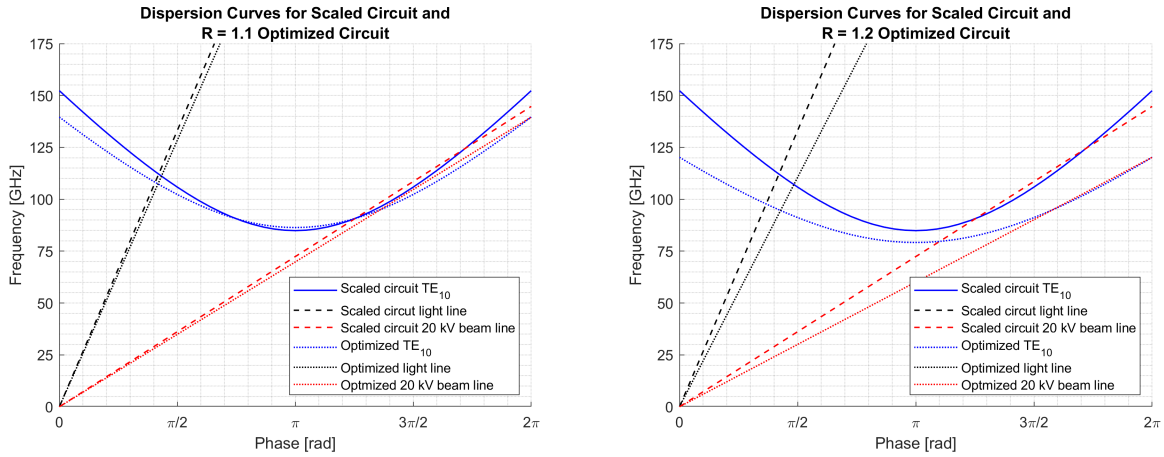

(a) $R_1 = 1.1$ optimized geometry.

(b) $R_2 = 1.2$ optimized geometry.

Figure 7.6: Simplified analytical TE_{10} mode dispersion curves for the $R_1 = 1.1$ and $R_2 = 1.2$ optimized geometries compared to the scaled circuit.

The dispersion curves in Fig. 7.6 demonstrate how different R-values affect the SWG circuit's electromagnetic characteristics. In the case where $R = R_1$, the cutoff frequency rises slightly to $f_{c1} \approx 86$ GHz and in the case where $R = R_2$, the cutoff frequency decreases to $f_{c2} \approx 79$ GHz. Regardless of the change in cutoff frequency, however, we can see the lower beam-wave intersection for R_1 occurs at ≈95 GHz, or 10% above f_{c1}, and the lower intersection for R_2 also occurs at ≈95 GHz, or 20% above f_{c2}, as expected.

7.4.3 Optimized Geometry Dispersion Modeling

Attention now turns to implementing the analytical model into a practice by realizing the dimensions output by the optimization scheme into a CAD model for the SWG. Once a CAD model is created, an eigenmode simulation on a single circuit period can be performed in HFSS. CAD models for both the $R_1 = 1.1$ and $R_2 = 1.2$ optimizations were created and simulated; their simulated dispersion curves are depicted in Fig. 7.7.

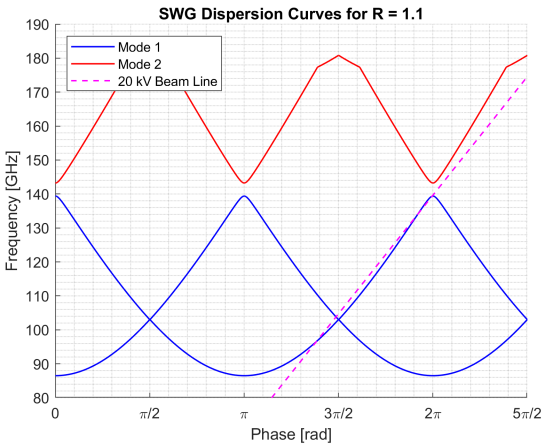

(a) $R_1 = 1.1$ optimized geometry.

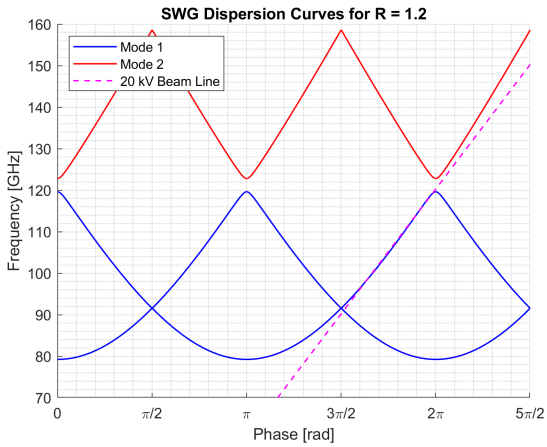

(b) $R_2 = 1.2$ optimized geometry.

Figure 7.7: Simulated dispersion curves for the $R = R_1$ and $R = R_2$ optimized geometries with an overlayed 20 kV beam line.

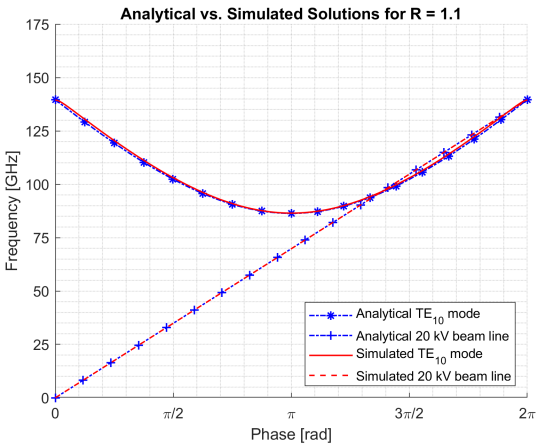

(a) $R_1 = 1.1$ optimized geometry analytical result compared to its HFSS simulation.

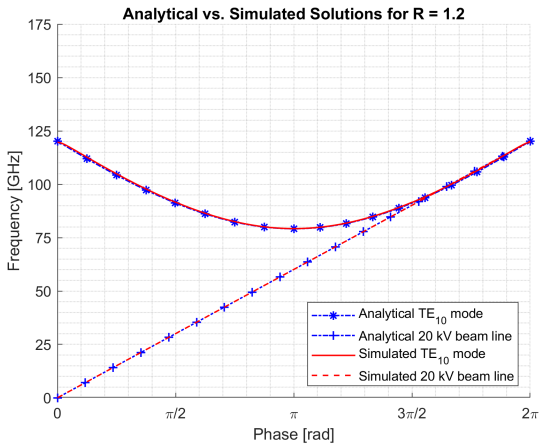

(b) $R_2 = 1.2$ optimized geometry analytical result compared to its HFSS simulation.

Figure 7.8: Comparison of the $R = R_1$ and $R = R_2$ analytical geometry optimizations to their HFSS simulations.

The HFSS simulation results are extremely encouraging. For both values of R, it is clear from both Fig. 7.7a and Fig. 7.7b the beam line intersects the TE_{10} mode's dispersion curve precisely at 2π as we demanded. The second constraint that the lower intersection occurs between π and 2π is also obeyed. More importantly, no intersections between the beam line or any backward-waves are present, which is the optimization's principle goal.

An even more impressive result becomes evident when inspecting just the lowest mode from the simulation results in Fig. 7.7a and Fig. 7.7b. When the HFSS simulation results are overlayed onto the analytical results illustrated in Fig. 7.6a and Fig. 7.6a, we can see outstanding agreement between the curves. In fact, there is no visible deviation except for where the simulated results begin to round off at 0 and 2π (i.e., where the bandgaps occur). This is expected because the analytical dispersion relation from [24] used to begin the safety factor derivation is only valid for the lowest mode and does not account for bandgaps. The agreement between the analytical results and the HFSS simulations presented in Fig. 7.8a and Fig. 7.8a and are quite an amazing result. Not only is the analytical model confirmed, it has also been shown the model is valid to a high degree of accuracy for SWG TWTs in which backward-wave instabilities must be avoided.

7.4.4 Optimized Geometry S-Parameters

Additional HFSS simulations were performed for the $R_1 = 1.1$ and the $R_2 = 1.2$ optimized geometries to obtain their S-parameter responses. These simulations are summarized in Fig. 7.9.

The reflected power results presented in Fig. 7.9a provides alternate viewpoint of the different SWG geometries' cutoff frequencies, each of which are consistent with their corresponding dispersion curve. The geometry with the largest bandwidth (and hence, lowest

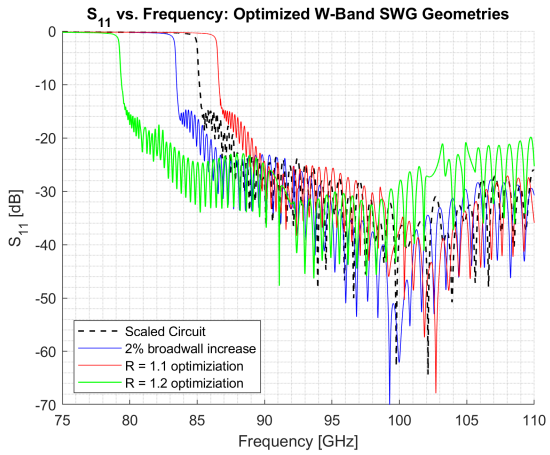

(a) S_{11} summary for the optimized circuits.

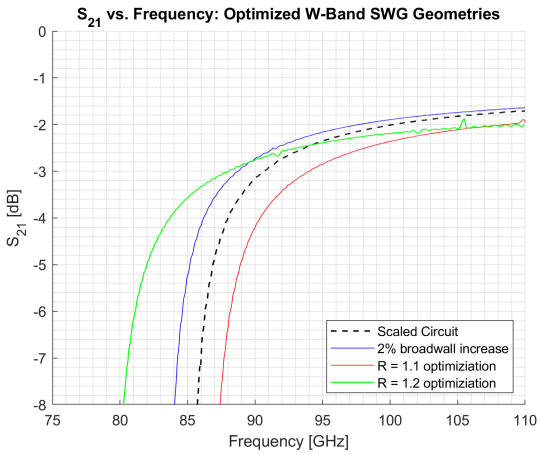

(b) S_{21} summary for the optimized circuits.

Figure 7.9: Summary of the three optimized geometries' S-parameters compared to the original, scaled circuit's S-parameters.

cutoff), is the $R = R_2$ optimized circuit. At 95 GHz (the chosen operating frequency), the $R = R_2$ circuit has the lowest reflection; however, at 99 GHz, the device's reflection increases to levels up to 10 dB above S_{11} for other geometries. The circuit with the 2% broadwall increase exhibits the lowest reflection. Between 95 GHz and 105 GHz, this geometry has an S_{11} response below 30 dB down with some frequencies exhibiting reflections as low as -50 dB over a 1 GHz bandwidth. The $R = R_1$ optimization appears to exhibit an S_{11} response between the remaining reflected power responses, but it has the smallest bandwidth.

As for S_{21} in the optimized geometries shown in Fig. 7.9b, it is clear the $R = R_1$ circuit has the lowest transmitted power. Its level peaks at about 2 dB down and it does not reach this level until near the band edge at 108 GHz. In fact, the transmitted power through this circuit is less than -3 dB until 94 GHz indicating less than half the power makes it through the circuit at frequencies below 95 GHz.

The geometry where the broadwall is increased by 2% has the highest transmitted power peaking at about -1.6 dB at 110 GHz. This circuit has a bandwidth of $\approx$26 GHz. The $R = R_2$ optimization exhibits an S_{21} response that is somewhere between the highest and lowest transmitted power response.

7.5 Chapter Summary

The transition to designing the W-band circuit for the SWG TWT prototype has been discussed in detail throughout this chapter. Reverse engineering a circuit design presented in [34] resulted in a preliminary circuit design that was then altered in an attempt to increase bandwidth, which was successful. Backward-wave instabilities were present in this circuit, however, so an analytical optimization technique to prevent said instabilities was derived and confirmed through HFSS simulations. Further discussion about final W-band circuit geometry choice will be discussed in Sec. 8.2.

Chapter 8: Conclusions and Future Work

8.1 Conclusions

8.1.1 Ka-Band Circuit

A detailed study of a Ka-band SWG has been presented. Simulations were performed using the CEM software HFSS to improve matching between the SWG and the tapers to the WR-28 standard waveguide size as well as to characterize the possible effects misalignments in the SWG circuit had on its RF performance. Mechanical precision alignment techniques were also introduced and realized in a Ka-band circuit to mitigate such misalignments in the fabricated device. Circuit cold tests were then carried out in the laboratory to determine if any misalignments in the fabricated structure degraded the microwave signal in the SWG.

The matching step transformer between the SWG and the tapers determined to have the lowest simulated reflected power, or S_{11}, and maintain a reasonable size to facilitate fabrication was the fillet with a 15 mil radius located 62.5 mil away from the beam tunnel's axis.

Simulations of various misalignments in the final Ka-band circuit geometry were then performed. Both one-dimensional and two-dimension misalignments in the $\hat{x}$-direction and the $\hat{z}$-direction with magnitudes ranging from 1 mil and 5 mil were introduced into the circuit. Rotational misalignments with angular displacements ranging from 0.1° to 0.5° in the clockwise

direction were also studied. It was found that the 1D misalignment with the greatest disruption to the reflected power was the 5 mil misalignment in the $\hat{z}$-direction. This disturbance was observed to decrease S_{11} by up to 18 dB at 32 GHz, which is the frequency corresponding to the $3\pi/2$ point. It has been observed in other studies in the VED field the $3\pi/2$ point is the a phase at which instabilities often occur.

The 2D shear misalignments proved to increase the reflected power and decrease the transmitted power (S_{21}). At 32 GHz, or where the $3\pi/2$ point occurs, significant increases in S_{11} and decreases in S_{21} were observed in the simulations with increasing misalignment severity. A 20 dB increase from -28 dB to -8 dB in S_{11} was seen in the $(x, z) = (5, 5)$ mil shear misalignment and a corresponding decrease of 0.9 dB from -0.6 dB to -1.5 dB was seen in S_{21} for the same misalignment. The $(5, 5)$ mil misalignment was most detrimental to the SWG circuit as hypothesized. It was also found the increases in S_{11} and decreases in S_{21} were nonlinear for the shear misalignments. Eigenmode simulations to obtain the dispersion curves for shear misalignments in the SWG device found the cutoff frequency decreases nonlinearly and the bandgap size increases quadratically with increasing misalignment magnitude, as well.

Rotational misalignments in the Ka-band circuit also increased the reflected power and decreased the transmitted power as the displacement grew larger in magnitude. There were no concentrated frequencies where these disturbances were significantly larger than in other portions of the band unlike in the case of the shear misalignments. The increase in S_{11} remained relatively uniform across Ka-band with a peak reflection of about 15 dB down occurring at $\approx$39.75 GHz, which is 7 dB lower than the peak pass band reflection for the shear misalignments. The observed increases in S_{11} for the rotational misalignments were nonlinear just as was the case for the shear misalignments.

Rotational misalignments caused a more significant standing wave to arise in the transmitted microwave signal compared to the shear misalignments, as well. The standing wave with largest magnitude that was observed in the rotational misalignment simulations also occurred at ≈39.75 GHz between −0.45 dB and −0.65 dB for a 0.2 dB magnitude. Though this standing wave has a small magnitude compared to the reflected standing wave, it is the largest standing wave magnitude seen relative to the transmitted power.

Laboratory measurements of the fabricated Ka-band circuit were performed following the misalignment simulations in HFSS. The unbrazed structure was manufactured and tested first and it was demonstrated the device's reflected and transmitted power were nearly identical in the unclamped, single-clamped, and double-clamped circuit blocks. This behavior has seldom, if ever, been observed before in the VED field. Our results validate the efforts put forth to manufacture and assemble a device with a high degree of precision using the elastic averaging technique. In these cold test measurements, the maximum reflection in the unbrazed circuit's pass band reached approximately −20 dB, which was only 5 dB above the HFSS simulated values. The transmitted power was measured to be between −1 dB and 0 dB for 28 GHz and above. Considering flange adapters had to be used in the unbrazed measurements, we conclude this level is acceptable and proves a successful design and fabrication.

The fabricated brazed circuit exhibited even lower reflected power and higher transmitted power than unbrazed circuit. It was encouraging to confirm the original hypothesis that stated this behavior. An interesting observation was also made in the brazed circuit's measured S_{11}. Between 32 GHz and 33 GHz, the reflected power significantly decreases to below −50 dB from levels just above −30 dB outside this 1 GHz bandwidth. Recall the $^{3\pi}/_{2}$ point, or the point at which instabilities often arise, occurs at 32 GHz for the Ka-band circuit. In the HFSS simulations,

we saw that 2D shear misalignments cause a significant increase in the reflected power at this point. In all the misalignment types and magnitudes tested, however, the $(x, z) = (0, 5)$ mil misalignment was the only displacement observed to improve S_{11} near 32 GHz. This may suggest the decrease in S_{11} may not necessarily be related to the one-dimensional misalignment magnitude, but instead, when the displacement in one dimension, particularly in the $\hat{z}$-direction, far exceeds the displacement in the adjacent dimension. Additional simulations and laboratory tests are required to confirm this result, however.

8.1.2 W-Band Circuit

The larger-scale Ka-band circuit's design and fabrication provided an excellent starting point to begin the W-band circuit design, which will have to be done at a much smaller scale given the decrease in wavelength. Design efforts began by reverse engineering a W-band SWG circuit presented in [34] by A.M. Cook *et al.* Subsequent HFSS simulations of the reverse-engineered, or "scaled," circuit and comparison of its S-parameters and dispersion curves to those presented in [34] proved the scaled circuit's validity.

Focus then shifted to improving the scaled circuit's bandwidth, but more importantly, to revise its dispersion such that there were no beam-wave interactions with any backward waves, as were present in the circuit presented in [34]. An analytical model based on a simplified dispersion relationship for the TE_{10} mode originally described in [24] was then derived to avoid said crossings. The analytical model defined a safety factor, $R \equiv \omega_L/\omega_c$, or the ratio of the beam line's intersection with the TE_{10} mode below 2π, to ensure the beam line's upper intersection with the TE_{10} mode occurs at 2π. This requirement prevents any backward-wave

intersections and thus, improves device stability. The analytical optimization output several SWG geometry parameters to create a new geometry that would exhibit these desired properties. HFSS simulations of the $R_1 = 1.1$ and $R_2 = 1.2$ optimizations were performed and compared to the analytical model. Excellent agreement was observed between the two, thus validating the analytical model's effectiveness and proving it can be used as an effective tool in future FW/SWG TWT design.

Finally, the S-parameters for the SWG with the 2% broadwall increase and the two optimized geometries were simulated and compared to the scaled circuit. Overall, these three geometries all exhibited lower transmission than the simulated Ka-band circuit. The best observed transmission had a maximum of approximately -1.6 dB at 110 GHz, or W-band's upper threshold. The greatest bandwidth simulated was the $R = R_2$ optimization that exhibited a pass band from $\approx$79 GHz to 110 GHz.

8.2 Future Work

A detailed study into the effect misalignments have in a Ka-band SWG circuit and an optimization technique used to avoid backward-wave instabilities in a W-band circuit have been presented. Although this text is quite comprehensive, by no means does it provide definitive conclusions for all the topics covered; there are certainly areas where more research must be conducted.

In the Ka-band circuit, the Pierce impedance described in Sec. 3.5 should be calculated for the aligned structure as well as for the 1D, shear, and rotational misalignments. This calculation can provide further quantitative insight into how misalignments affect the gain of the TWT when

the device is running hot (i.e., when an electron beam is propagating through the beam tunnel). Work has already begun on this calculation, but unfortunately, time constraints prevented it from being completed before the conclusion of this thesis.

As for the W-band circuit, the next steps include inputting the simulated eigenmode data for the SWG with the 2% broadwall increase and the two optimized geometries into the large-signal interaction codes CHRISTINE and TESLA-Z to compute the structures' impedance matrices and gain. These results will then be used in conjunction with the S-parameters and dispersion curves simulated in HFSS to create a final W-band SWG circuit design. At this point in time, it appears the most promising geometry is the $R = R_1$ optimization. In this geometry, there is slightly more space between the 20 kV beam line and the TE_{10} mode's dispersion curve. This is important to consider when creating a real-world device because space charge forces in the beam may cause the beam line shift to the right and alter the interaction frequencies. If there is more space in between the beam line and the and dispersion curve in the cold simulations, there is more of a buffer for the beam line to shift without exciting any backward waves.

Similar misalignment studies to those made for the Ka-band circuit may also be performed for W-band devices. Characterizing the RF response across two bands that are separated by a minimum of 35 GHz could prove incredibly insightful to the circuit's overall behavior. It is likely the smaller wavelengths at W-band will cause the device to be susceptible to smaller misalignments and potentially have more pronounced signal degradation for the same misalignment magnitudes tested for the Ka-band studies. A final circuit geometry cannot be decided upon by analyzing only one simulation, however. Careful thought and consideration of all the simulations (and potentially laboratory tests of numerous circuit geometries) must be put forth before a final decision can be made for the W-band device's geometry.

As this thesis is being composed, extensive work is being on done the W-band SWG TWT prototype. Efforts are being made to improve the tolerances of the elastic averaging precision alignment technique, the adjoint method is being implemented in MICHELLE to aid in the electron gun design (as described in Appendix A), a custom magnet for the beam's focusing field is being designed, and further simulations of the optimized SWG circuit geometries will be performed so that a final circuit geometry design can be chosen. In summary, the W-band SWG TWT prototype is on schedule to be delivered to the Navy by the STTR's conclusion.

This page is intentionally left blank.

Appendix A: TWTs and the Adjoint Method

Before it is possible to apply the general principle of the adjoint method to traveling-wave tubes, it is necessary to first introduce its origin and the reason for its use.

A.1 Introduction to the Adjoint Method

The adjoint method is a general, mathematically-based method for finding the sensitivity of a system's performance to the many parameters that describe said system [38, 39]. The advantage of the adjoint method over a direct method, in which system parameters are individually varied, is that the dependence on all parameters can be determined by one or two solutions of the system's adjoint equations rather than requiring a solution of the base equations for each parameter variation.

To illustrate this concept, consider a system whose state is defined by an N-dimensional vector, $\boldsymbol{x}$, that depends on a vector, $\boldsymbol{B}$, of M variables (note that here, $\boldsymbol{B}$ is *not* the magnetic field vector) [38]. If the system is described by differential equations, the dimension of $\boldsymbol{x}$ might be infinite. Similarly, if the parameters of the system are functions, such as the shape of a surface, M may be infinite as well. The relation between the system state and the parameters can be represented by the nonlinear vector equation

$$\boldsymbol{A}(\boldsymbol{x}) = \boldsymbol{B} \, . \tag{A.1}$$

Further, it is possible to represent the performance of the system in terms of a scalar figure of merit $G(\boldsymbol{x}, \boldsymbol{B})$, chosen by the system's designer. The goal is to find the dependence of G on $\boldsymbol{B}$ for an arbitrary reference state $\boldsymbol{x}$. The variation of G with given changes in $\boldsymbol{B}$ can be represented in terms of incremental changes in the governing variables,

$$d\boldsymbol{G} = G_x \cdot d\boldsymbol{x} + G_{\boldsymbol{B}} \cdot d\boldsymbol{B} \tag{A.2}$$

where G_x and $G_{\boldsymbol{B}}$ are vectors of derivatives with lengths N and M, respectively. The first term represents the implicit dependence of the figure of merit G on the parameters through changes of the system state, $d\boldsymbol{x}$, and the second term represents the explicit dependence of G on the change in parameters $d\boldsymbol{B}$. The implicit change in the system state depends on the change in parameters through the linearized system relation

$$d\boldsymbol{A}_{\boldsymbol{x}}(\boldsymbol{x}) \cdot d\boldsymbol{x} = d\boldsymbol{B} \tag{A.3}$$

where $d\boldsymbol{A}_{\boldsymbol{x}}(\boldsymbol{x})$ is an M-by-N matrix of derivatives. For a direct calculation of $d\boldsymbol{G}$, this matrix must be inverted to find $d\boldsymbol{x}$ in terms of $d\boldsymbol{B}$, and then inserted into (A.2) to find $d\boldsymbol{G}$. This implies the inversion of an M-by-N matrix.

The adjoint approach is to solve:

$$\boldsymbol{y} \cdot d\boldsymbol{A}_{\boldsymbol{x}}(\boldsymbol{x}) = G_x \tag{A.4}$$

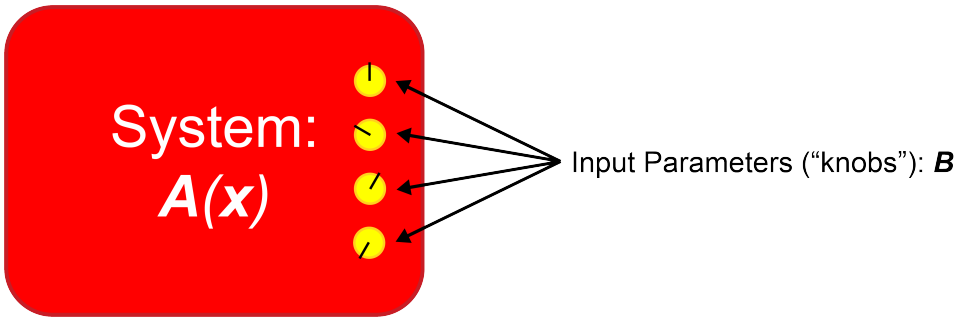

Figure A.1: Block diagram representing a graphical view of the adjoint method. The system, $\boldsymbol{A}(\boldsymbol{x})$, has the state $\boldsymbol{x}$ and input parameters, $\boldsymbol{B}$, that can be thought of as "knobs" to adjust the system's state.

a single time for the vector $\boldsymbol{y}$. It then follows that

$$d\boldsymbol{G} = (\boldsymbol{y} + G_{\boldsymbol{B}}) \cdot d\boldsymbol{B} \; . \tag{A.5}$$

The adjoint method is unique in the sense it allows for efficient computation of the gradient of the function, $G(\boldsymbol{x}, \boldsymbol{B})$, that is dependent on both the solution, $\boldsymbol{x}$, and the control parameters, $\boldsymbol{B}$. Recall the function G contains figures of merit the designer chooses [38]. Computing the gradient of G reveals how changes in the control variables affect G, which is particularly powerful when designing a system with a large number of parameters. The system can be represented as a block diagram depicted in Fig. A.1.

A.2 Qualitative Application of the Adjoint Method to TWTs

Application of the adjoint method to TWTs is best illustrated in the case of the SWG structure in Fig. 2.10. It is quite clear where misalignments may arise in the structure when the two halves of the copper block are fastened together. To be more specific, the most apparent misalignments occur in the x-z plane, or the plane of the blocks' mating surfaces. Said

misalignments in the structure could cause disturbances in the RF field in the SWG and/or cause the beam to scrape on the beam tunnel walls. Both of the aforementioned consequences could severely degrade the TWT's performance, thus demonstrating the need to better understand what types of effects these misalignments have on the structure.

Characterizing the SWG structure's sensitivity to disturbances in its geometry can be categorized into two parts: the effect on the RF signal and the effect on the electron beam. The RF characterization has be discussed at length throughout this text. This section serves to provide an overview of efforts put forth by our group to determine the effects electron gun misalignments have on the TWT's performance.

Currently, studying the consequences structural misalignments have in a device such as the SWG is extremely time consuming. The main method used to gain an understanding of the device's behavior, particularly the beam, are primarily PiC codes, which use a much smaller number of particles to represent a group of a large number of particles, such as electrons and ions, to increase computation speed [40]. Though efficient for general beam simulations, PiC codes are not optimized for misalignment studies. They are more than capable of computing the desired fields in a misaligned device, however, simulating misalignments must be done one at a time. In other words, it is usually advantageous to simulate more than one misalignment magnitude to determine their effects on the fields, but in current PiC codes, each misalignment would have to be simulated separately, which is extremely time consuming.

At this point is where the introduction of the adjoint method greatly improves the computation speed. By defining one "sensitivity function," or a figure of merit (FoM), decided upon by the researcher, the adjoint method allows for the calculation of how a large number of

changes in geometrical properties impact said FoM in only one additional run of the PiC code, rather than several runs each containing a single misalignment or geometry perturbation [41].

A.3 Quantitative Application of the Adjoint Method to TWTs

To better understand the adjoint method's applicability to TWTs, consider the example of aligning an electron gun to the SWG circuit block shown in Fig. 2.10. If the gun is misaligned in any way, the beam will not propagate down the center of the beam tunnel and thus, interact with the RF fields in potentially unexpected ways. Additionally, a small perturbation in the electric field will arise anywhere there may exist misalignments in the SWG structure. The perturbations in the field will cause a change in the root-mean-square (RMS) beam radius, $\langle x^2 \rangle$, which can be written as

$$G(\boldsymbol{x}) = \delta\langle x^2 \rangle = \int_S dA \; (\delta E_n) \, \Delta|x| \tag{A.6}$$

where $G(\boldsymbol{x})$ is the FoM and δE_n is the normal component of the electric field on the gun's anode, which will be defined as the "sensitivity function" herein.

Modeling such a change in the figure of merit, $\langle x^2 \rangle$, in the PiC code is done by perturbing the electrons where the beam exits the gun (i.e., to the right of the anode; see Fig. A.2). Then, the beam and magnetic field are reversed in both time and space (i.e., the beam propagates in the $-\hat{z}$-direction). Using the adjoint method, the change in δE_n, or the sensitivity function, can be calculated yielding the manner in which the beam responds to any misalignments. A more in-depth description of PiC code modeling of the adjoint method is discussed in the Sec. A.4.

Mathematically, the above discussion can be written as the following steps. First, take the electron gun to be the"system," $\boldsymbol{A}(\boldsymbol{x})$, where the vector $\boldsymbol{x}$ is N-dimensional and contains information about the electron gun's current state. The misalignments and other system parameters, such as the magnetic field, demanding our attention are then compiled and stored in the vector $\boldsymbol{B}$. Recall from previous sections the parameters represented by $\boldsymbol{B}$ can be thought of "knobs" to adjust system parameters. Thus, it is possible to rewrite (A.1), which is nonlinear, by linearizing around an equilibrium to get the matrix equation

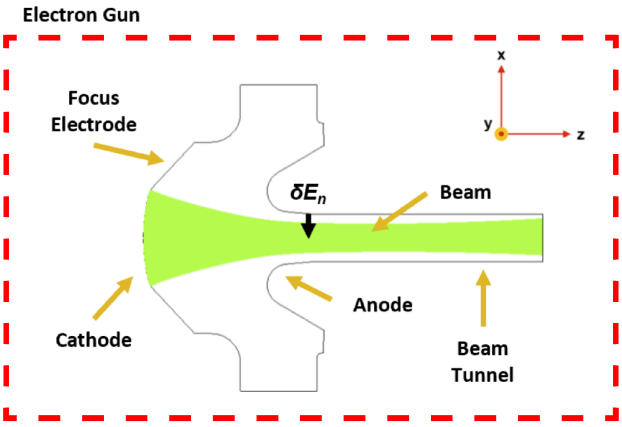

Figure A.2: 2D cross-section of an electron gun. Adapted from [42].

$$A\boldsymbol{x} = \boldsymbol{B} \ . \tag{A.7}$$

The next step is to perturb the system in the following manner:

$$\mathbf{x} = \mathbf{x} + \delta\mathbf{x} \tag{A.8}$$

$$\mathbf{B} = \mathbf{B} + \delta\mathbf{B} \tag{A.9}$$

$$\mathbf{G} = \mathbf{G} + \delta\mathbf{G} \tag{A.10}$$

and rewrite (A.7) as

$$\frac{\partial A}{\partial \boldsymbol{x}} \cdot \boldsymbol{x} = \delta\boldsymbol{B} \Rightarrow \bar{\bar{A}} \cdot \delta\boldsymbol{x} = \delta\boldsymbol{B} \ . \tag{A.11}$$

It is also possible to write

$$\delta \boldsymbol{G} = \delta \boldsymbol{x} \cdot \frac{\partial G}{\partial \boldsymbol{x}} \, . \tag{A.12}$$

At this point is where the adjoint method is introduced. It is desired to find a variable, $\boldsymbol{y}$, such that the following is true:

$$\boldsymbol{y} \cdot \bar{\bar{A}} = \frac{\partial G}{\partial \boldsymbol{x}} \Rightarrow \boldsymbol{y} = \frac{\partial G}{\partial \boldsymbol{x}} \cdot \bar{\bar{A}}^{-1} \, . \tag{A.13}$$

Because A is a function of all the system parameters, $\boldsymbol{x}$, it is necessary to calculate $\bar{\bar{A}}^{-1}$ only once, thereby significantly decreasing simulation time. In this example, the term $\boldsymbol{y} \cdot \bar{\bar{A}}$ is equivalent to time reversal of the beam and the magnetic field due to the equations of motion and Hamiltonian dynamics. From (A.11), it is then possible to write

$$\begin{cases} y \cdot \bar{\bar{A}} \cdot \delta \boldsymbol{x} = \boldsymbol{y} \cdot \delta \boldsymbol{B} & \text{(A.14)} \\ \dfrac{\partial \boldsymbol{G}}{\partial \boldsymbol{x}} \cdot \delta \boldsymbol{x} = \boldsymbol{y} \cdot \delta \boldsymbol{B} & \text{(A.15)} \end{cases}$$

yielding

$$\boxed{\delta \boldsymbol{G} = \boldsymbol{y} \cdot \delta \boldsymbol{B} \, .} \tag{A.16}$$

In other words, the change in the FoM (in this case, only the RMS beam radius) caused by *any* change in parameters can be deduced [41]! It is also important to note there may be more than a single FoM, thereby increasing the robustness of this calculation.

Further quantitative discussions regarding the adjoint method and its applications are presented in [43]. In this reference, other TWT figures of merit are optimized including average gain, gain flatness, the gain-bandwidth product, beam voltage, and circuit geometry.

A.4 PiC Modeling with the MICHELLE Code

As mentioned previously, PiC codes are widely used in beam modeling. Many versions of these codes exist, however, the adjoint method remains absent from them all. One particular code, MICHELLE, largely developed by Dr. John Petillo and Dr. Eric Nelson (and described in more detail in [42] and [44]), has been chosen as the first code into which the aforementioned formulation of the adjoint method, largely developed by Professor Thomas M. Antonsen, Jr. of the University of Maryland, College Park, will be integrated. The following discussion is a brief overview of how the adjoint method's application to TWTs is implemented using the code.

The first step in the adjoint method simulation is to propagate an undisturbed electron beam in the forward direction, which is defined to be from left to right, as depicted in Fig. A.3a. The beam energy for this set of runs is 10 keV. In the forward case, the beam propagates in the $+\hat{z}$-direction between two boundaries at ground potential (0 V) [41]. Affixed to the upper and lower portion of the blue boundaries in Fig. A.3 are two electrodes (the red patches) that create a potential difference between them. These electrodes are also held at ground potential for the forward case and the y-component of the electron's velocities are set such that the beam is laminar [41]. The focusing is provided by a magnetic field. This simulation will serve as the "base case," i.e., the control [41].

The potential difference across the electrodes is then set to 2 kV for the second, perturbed case as shown in Fig. A.3b. When the beam travels through the potential difference, it is "kicked" and begins to oscillate [41]. The restoring force in this mechanism is a magnetic field, just as in the forward case. Because the beam has been perturbed, the electrons reach the rightmost boundary with a displacement along the x-axis. This offset is saved by the code [41].

Finally, in the third case, the electron's velocities and the magnetic field are reversed in time, causing the particles to propagate backwards (from the right boundary to the left boundary) as shown in Fig. A.3c [41]. Before the particles are launched backwards, however, the potential across the electrodes is set back to 0 V. When the reversed beam propagates between the electrodes, the change in the normal component of the electric field on the electrodes, δE_n, is recorded. Using the adjoint method theory presented earlier, the change in the normal electric field, or the sensitivity function, can be used in (A.16) to find the relation between the sensitivity function and the directly perturbed beam in Fig. A.3b [41]. It is important to reiterate the process described above only requires a single additional run of the MICHELLE code, the case of the time-reversed beam, that is, to arrive at the adjoint solution, rather than simulating each misalignment individually [41].

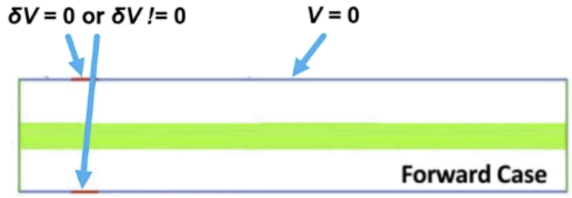

(a) Forward, unperturbed case (i.e., the base case).

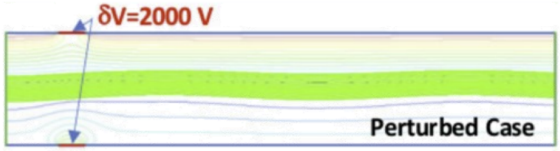

(b) Direct, perturbed case.

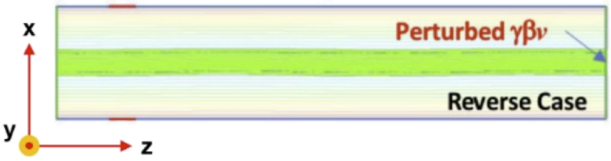

(c) Time-reversed case.

Figure A.3: MICHELLE simulations of an electron beam propagating between two boundaries. Adapted from [41].

Appendix B: Additional HFSS Simulation Results

B.1 Overview

This appendix serves to provide HFSS simulation results for geometries mentioned throughout this text for which there was insufficient room to include them in the thesis body. Numerous points made in the previous sections are clarified here by examining the results provided.

B.2 "Additional Adjustments" S-Parameters

The HFSS simulations for S_{11} and S_{21} in this section correspond to the "additional adjustments" described in Sec. 4.6. A more thorough description of each adjustment is included in the list below followed by the simulation results.

- **Input Step Width (ISW):** The distance the fillet protrudes from the SWG (in the $\hat{z}$-direction). Altering the ISW dimension does *not* affect the fillet radius.
- **Input/Output Taper Length (IOTL):** Taper ramp length. This ramp is defined to be the distance in $\hat{x}$ beginning at the IOSTT's end and extending to the beginning of the WR-28.
- **Input/Output Step-Out to Taper (IOSTT):** The distance in $\hat{x}$ from the fillet's center to the taper ramp's beginning.

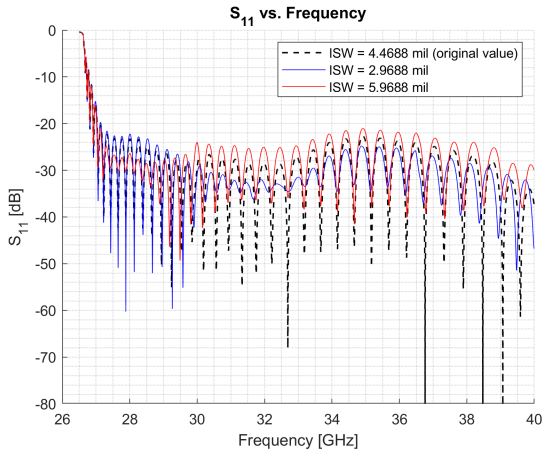

(a) S_{11} response for various ISW values.

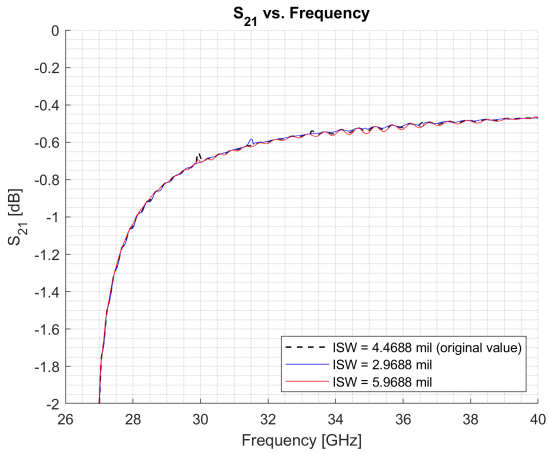

(b) S_{21} response for various ISW values.

Figure B.1: HFSS reflection and transmission simulation results for the two adjustments made to the ISW dimension in vacuum space model compared to the parameter's original value.

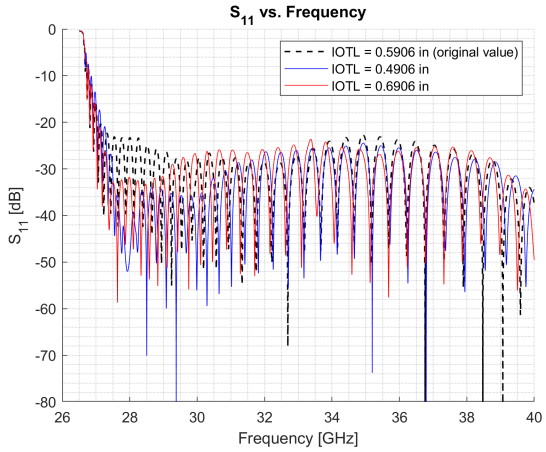

(a) S_{11} response for various IOTL values.

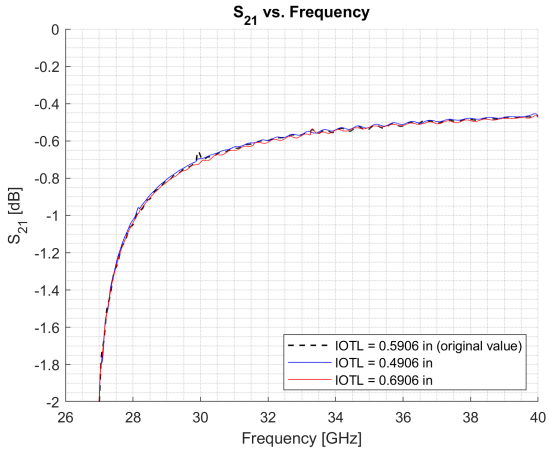

(b) S_{21} response for various IOTL values.

Figure B.2: HFSS reflection and transmission simulation results for the two adjustments made to the IOTL dimensions in vacuum space model compared to the parameters' original values.

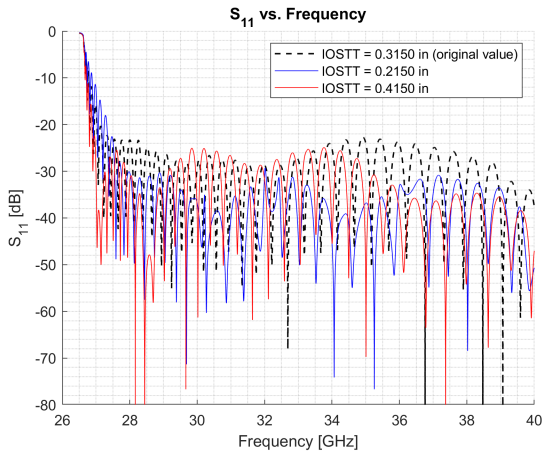

(a) S_{11} response for various IOSTT values.

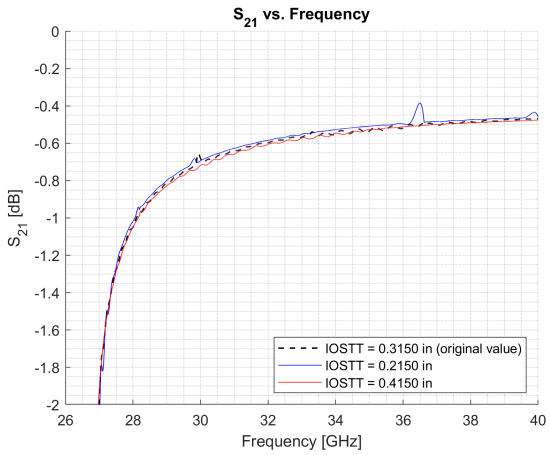

(b) S_{21} response for various IOSTT values.

Figure B.3: HFSS reflection and transmission simulation results for the two adjustments made to the IOSTT dimensions in vacuum space model compared to the parameters' original values.

B.3 CAD Model Verification

To create the misaligned structures shown in Fig. 5.1a and Fig. 5.1b, the CAD model in Fig. 4.10 (an aligned geometry), which we will define as the "solid" geometry was split using the x-z half-plane. This new, cut model is defined as the "split" geometry, which is saved as a separate file from the "solid" geometry. Both these vacuum space models were created in the CAD software SolidWorks, as mentioned previously, and exported as *.stp file. The *.stp file was then imported into HFSS to carry out the electromagnetic simulations.

Geometry discrepancies commonly arise when importing CAD models into HFSS, which is out of the user's control. The only way to avoid this issue is to create the model in HFSS itself, but this was not done for this research due to the mechanical team's better familiarity with SolidWorks and contractual time constraints. For this reason, it was imperative to ensure the split, aligned geometry [i.e., a misalignment of $(x, z) = (0, 0)$] exhibits the same, or very close to the same, S-parameters as the solid geometry. This was done by simulating both the solid geometry

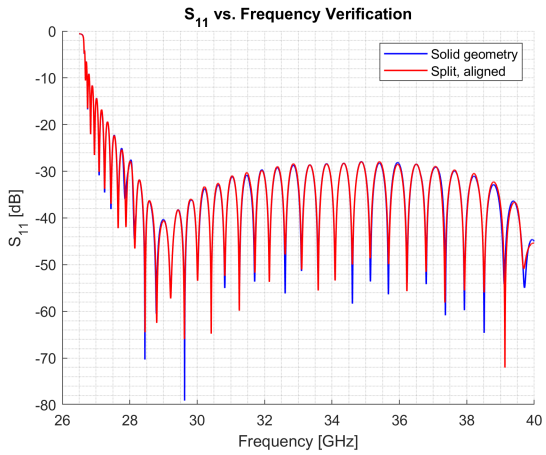

(a) S_{11} response for solid geometry (blue trace) and the split, aligned geometry (red trace).

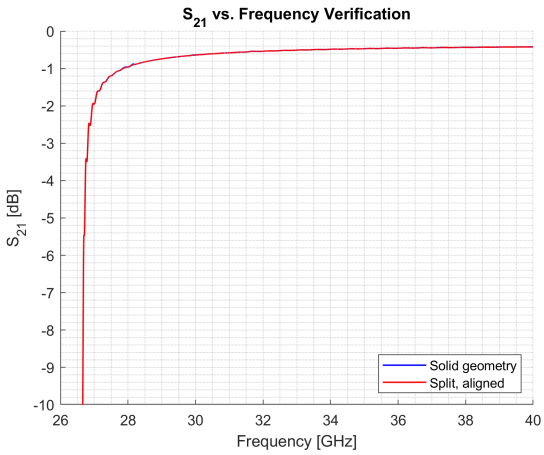

(b) S_{21} response for solid geometry (blue trace) and the split, aligned geometry (red trace).

Figure B.4: HFSS reflection and transmission simulation results for the solid geometry CAD model and the split, aligned CAD model.

as well as the split, aligned geometry. The resulting S-parameters from these simulations are shown in Fig. B.4.

It is apparent from Fig. B.4 both structures exhibit almost identical S-parameters. Both structures' standing wave periodicity is preserved, as seen in Fig. B.4a, and there are only four, 1 dB deviations in S_{11} magnitude at ≈31.50 GHz, ≈37.75 GHz, ≈38.25 GHz, and ≈39.75 GHz. These small deviations occur at levels below 25 dB down, confirming they are insignificant. The S_{21} response for both structures in Fig. B.4b also confirms nearly identical model behavior with few deviations, all of which with magnitudes much less than 1 dB.

For the reasons described in the previous paragraph, we conclude the solid geometry model exhibits the same RF characteristics as the split, aligned model, as expected.

Bibliography

[1] SBIR/STTR Programs. About the SBIR and STTR Programs. [Online]. Available: https://www.sbir.gov/about. [Accessed June 21st, 2022].

[2] NAVSEA – Naval Sea Systems Command. SBIR/STTR Program Description. [Online]. Available: https://www.navsea.navy.mil/Business-Partnerships/SBIR-STTR/. [Accessed June 21st, 2022].

[3] United States Department of the Navy. "Precision Alignment Techniques for Affordable Manufacture of Millimeter Wave Vacuum Devices." Topic : N20A-T013, Acquisition Program: PEO IWS 2: Advanced Offboard Electronic Warfare Program, 14 January, 2020.

[4] Dymenso, LLC. "Precision Alignment Techniques for Millimeter Wave Sources." Phase I Contract Number: N6833520C0815, Topic : N20A-T013, 10 January, 2021.

[5] T.J. Teo and A.H. Slocum. Principle of elastic averaging for rapid precision design. *Precision Engineering*, 49:146–159, 2017. https://doi.org/10.1016/j.precisioneng.2017.02.003. [Accessed July 2nd, 2022].

[6] P. Borchard. Precision mechanical interfaces for boosting millimeter-wave devices' performance. In *International Vacuum Electronics Conference (IVEC) 2022*, 27 April, 2022. Plenary presentation.

[7] M.L. Culpepper. *Design and Application of Compliant Quasi-Kinematic Couplings*. PhD thesis, Massachusetts Institute of Technology, February 2000.

[8] S. Gilmour. *Klystrons, Traveling Wave Tubes, Magnetrons, Cross-Field Amplifiers, and Gyrotrons*. Artech House, Boston, MA, 2011.

[9] Andrew V. Haeff. 19 October, 2021. [Online]. Available: https://en.wikipedia.org/wiki/Andrew_V._Haeff. [Accessed April 8th, 2022].

[10] A.V. Haeff. "Device for and method of controlling high frequency currents." U.S. Patent 2,064,469, 15 December, 1936.

[11] Y. Blancard, G. Galati, and P. van Genderen. The cavity magnetron: Not just a British invention. *IEEE Antennas and Propagation Magazine*, 55(5), October 2013. https://ieeexplore.ieee.org/stam/stamp.jsp?arnumber-6735528. [Accessed April 8th, 2022].

[12] J.R. Pierce. Traveling-wave tubes. *The Bell System Technical Journal*, 29(1):1–59, January 1950.

[13] P. Wong, P. Zhang, and J. Luginsland. Recent theory of traveling-wave tubes: A tutorial review. *Plasma Res. Express*, 2(2), 3 June 2020. https://dx.doi.org/10.1088/2516-1067/ab9730. [Accessed April 8th, 2022].

[14] D.M. Pozar. *Microwave Engineering*. John Wiley and Sons, Inc., Hoboken, NJ, 2012.

[15] J.G. Meeker and J.E. Rowe. Phase focusing in linear-beam devices. *IRE Trans. Electrton Devices*, 9(3):257–266, 1962. https://dx.doi.org/10.1109/T-ED.

[16] A.M. Cook, C.D. Joye, R.L. Jaynes, and J.P. Calame. W-band TWT circuit fabricated by 3D-printed mold electroforming. In *International Vacuum Electronics Conference (IVEC) 2018*, pages 331–332, Monterey, CA, 24–26 April, 2018. doi: 10.1109/IVEC.2018.8391511. [Accessed July 2nd, 2022].

[17] K.T. Nguyen et al. Design methodology and experimental verification of serpentine/folded-waveguide TWTs. *IEEE Tans. Electron Devices*, 61(6):1679–1686, June 2014.

[18] H.A. Haus and J.R. Melcher. *Electromagnetic Fields and Energy*. Prentice-Hall, Englewood Cliffs, NJ, 1989. ISBN: 9780132490207.

[19] A.M. Cook et al. W-band TWT component fabrication and testing. In *International Vacuum Electronics Conference (IVEC) 2019*, Busan, South Korea, 28 April – 1 May, 2019. doi: 10.1109/IVEC.2019.8745362. [Accessed July 3rd, 2022].

[20] A.M. Cook et al. Demonstration of a W-band TWT with 10 GHz bandwidth. In *International Vacuum Electronics Conference (IVEC) 2020*, Virtual, 19 – 22 October, 2020. doi: 10.1109/IVEC45766.2020.9520602. [Accessed July 3rd, 2022].

[21] R.E Collin. *Field Theory of Guided Waves*. John Wiley and Sons, Inc., Piscataway, NJ, 1990.

[22] D. Chernin et al. Large-signal multifrequency simulation of coupled-cavity TWTs. *IEEE Tans. Electron Devices*, 58(4):1229–1240, April 2011. https://doi-org.proxy-um.researchport.umd.edu/10.1109/TED.2011.2106504. [Accessed July 5th, 2022].

[23] A.N. Vlasov, T.M. Antonsen, Jr., I.A. Chernyavskiy, D.P. Chernin, and B. Levush. A computationally efficient two-dimensional model of the beam-wave interaction in a coupled-cavity TWT. *IEEE Tans. Plasma Science*, 40(6):1575–1589, June 2012. https://doi-org.proxy-um.researchport.umd.edu/10.1109/TPS.2012.2188547. [Accessed July 5th, 2022].

[24] T.M. Antonsen, A.N. Vlasov, D.P. Chernin, I.A. Chernyavskiy, and B. Levush. Transmission line model for folded waveguide circuits. *IEEE Tans. Electron Devices*, 60(9):2906–2911, September 2013.

[25] R. Marosi, T. Mealy, A. Figotin, and F. Capolino. Three-way serpentine slow-wave structures with stationary inflection point and enhanced interaction impedance. *arXiv*, June 2022. https://doi.org/10.48550/arXiv.2203.05641. [Accessed July 24th, 2022].

[26] D.A. Watkins. *Topics in Electromagnetic Theory*. John Wiley Sons, Inc., New York, 1958.

[27] J.H. Booske et al. Accurate parametric modeling of folded waveguide circuits for millimeter-wave traveling wave tubes. *IEEE Tans. Electron Devices*, 52(5):685–694, May 2005. https://doi.org/10.1109/TED.2005.845798. [Accessed July 24th, 2022].

[28] S.-T. Han, J.-I. Kim, and G.-S. Park. Design of a folded waveguide traveling-wave tube. *Microwave and Optical Technology Letters*, 38(2):161–165, July 2003. https://doi.org/10.1002/mop.11003. [Accessed July 24th, 2022].

[29] J. Pasour et al. High-power millimeter-wave cascaded traveling wave tube (TWT). Available through the U.S. Defense Technical Information Center (DTIC). Naval Research Laboratory, Washington, D.C., USA, 2020.

[30] EverythingRF. Waveguide sizes. 2020. [Online]. Available: https://www.everythingrf.com/tech-resources/waveguides-sizes. [Accessed July 6th, 2022].

[31] T.M. Antonsen, Jr. Effect of imperfections in FW structures on gain near the $3\pi/2$ intersection.

[32] Agilent Technologies, Inc. *Modern Measurement Techniques for Testing Advanced Military Communications and Radars, 2nd Edition*. Agilent Technologies, Inc., 2006.

[33] P. Borchard et al. Fabrication of traveling wave tube amplifier circuit using elastic averaging precision alignment technique. In *International Vacuum Electronics Conference (IVEC) 2022*, pages 166–167, Monterey, CA, 25–28 April, 2022.

[34] A.M. Cook et al. Demonstration of a W-band traveling-wave tube power amplifier with 10-GHz bandwidth. *IEEE Tans. Electron Devices*, 68(5):2492–2498, May 2021. https://doi.org/10.1109/TED.2021.3068926. [Accessed July 22nd, 2022].

[35] H.R. Johnson. Backward-wave oscillators. *Proceedings of the IRE*, 43(6):684–697, June 1955. https://doi.org/10.1109/JRPROC.1955.278054. [Accessed July 22nd, 2022].

[36] G.S. Nusinovich, Y. Carmel, T.M. Antonsen, Jr., D.M. Goebel, and J. Santoru. Recent progress in the development of plasma-filled traveling-wave tubes and backward-wave oscillators. *IEEE Tans. Plasma Science*, 26(3):628–645, June 1998. https://doi.org/10.1109/27.700799. [Accessed July 22nd, 2022].

[37] B. Levush, T.M. Antonsen, Jr., A. Bromborsky, W.-R. Lou, and Y. Carmel. Theory of relativistic backward-wave oscillators with end reflectors. *IEEE Tans. Plasma Science*, 20(3):263–280, June 1992. https://doi.org/10.1109/27.142828. [Accessed July 22nd, 2022].

[38] S.G. Johnson. Notes on adjoint methods for 18.335. 30 April, 2021. [Online]. Available: https://math.mit.edu/~stevenj/18.336/adjoint.pdf. [Accessed May 9th, 2022].

[39] T.M. Antonsen, Jr., D. Chernin, and J.J. Petillo. Adjoint approach to beam optics sensitivity based on Hamiltonian particle dynamics. *Phys. Plasmas*, 26, January 2019. https://dx.doi.org/10.1063/1.5079629. [Accessed May 9th, 2022].

[40] A. Pukhov. Particle-in-cell codes for plasma-based particle acceleration. In *Proceedings of the 2014 CAS-CERN Accelerator School: Plasma Wake Acceleration*, volume 1, 2016. https://dx.doi.org/10.5170/CERN-2016-001.181. [Accessed May 12th, 2022].

[41] J. Petillo et al. Development and application of adjoint methods in the presence of static electric and magnetic fields in the MICHELLE beam optics code. In *International Vacuum Electronics Conference (IVEC) 2022*, Monterey, CA, 25–28 April, 2022.

[42] J. Petillo et al. The new 3D electron gun and collector modeling tool: MICHELLE. In *International Vacuum Electronics Conference (IVEC) 2000*, Monterey, CA, May 2000. https://dx.doi.org/10.1109/OVE:EC.2000.847426. [Accessed May 12th, 2022].

[43] A.N. Vlasov, T.M. Antonsen, D.P. Chernin, and I.A. Chernyavskiy. Adjoint approach to optimization of TWT design. In *International Vacuum Electronics Conference (IVEC) 2022*, pages 146–147, Monterey, CA, 25–28 April, 2022.

[44] J. Petillo et al. The MICHELLE three-dimensional electron gun and collector modeling tool: Theory and design. *IEEE Tans. Plasma Sci.*, 30(3):1238–1264, June 2002. https://dx.doi.org/10.1109/TPS.2002.801659. [Accessed May 12th, 2022].